

2012-01-01

High-Order Central Finite-Volume Schemes For Atmospheric Modeling

Kiran Kumar Katta

University of Texas at El Paso, kattakiran@gmail.com

Follow this and additional works at: https://digitalcommons.utep.edu/open_etd



Part of the [Atmospheric Sciences Commons](#), [Mathematics Commons](#), and the [Mechanical Engineering Commons](#)

Recommended Citation

Katta, Kiran Kumar, "High-Order Central Finite-Volume Schemes For Atmospheric Modeling" (2012). *Open Access Theses & Dissertations*. 2119.

https://digitalcommons.utep.edu/open_etd/2119

This is brought to you for free and open access by DigitalCommons@UTEP. It has been accepted for inclusion in Open Access Theses & Dissertations by an authorized administrator of DigitalCommons@UTEP. For more information, please contact lweber@utep.edu.

HIGH-ORDER CENTRAL FINITE-VOLUME SCHEMES FOR ATMOSPHERIC MODELING

KIRAN KUMAR KATTA

Program in Computational Sciences

APPROVED:

Vinod Kumar, Chair, Ph.D.

Ramachandran D. Nair, Co-chair, Ph.D.

Andrzej Pownuk, Ph.D.

Rodrigo Romero, Ph.D.

Benjamin C. Flores, Ph.D.
Interim Dean of the Graduate School

©Copyright

by

Kiran Kumar Katta

2012

to my dearest

MOTHER and FATHER

HIGH-ORDER CENTRAL FINITE-VOLUME SCHEMES FOR ATMOSPHERIC
MODELING

by

KIRAN KUMAR KATTA, M.S., B.S.

DISSERTATION

Presented to the Faculty of the Graduate School of

The University of Texas at El Paso

in Partial Fulfillment

of the Requirements

for the Degree of

DOCTOR OF PHILOSOPHY

Program in Computational Sciences

THE UNIVERSITY OF TEXAS AT EL PASO

August 2012

Acknowledgements

Part of this research was carried out while I was visiting the National Center for Atmospheric Research (NCAR) in Boulder, CO, U.S.A; and for this summer intern and ASP visitor opportunity, I wish to acknowledge Dr. Richard Loft and Dr. Christopher Davis. I also must sincerely extend my deep-felt gratitude to Dr. Ram Nair, scientist III at NCAR. He was always available to provide insight advice for this project. Any amount of gratitude expressed to him will remain insufficient for he has been there for me as a good friend and mentor assisting and watching over me most of the way while working on the project at NCAR. He has taken the effort to understand my problems and support me, and to bring the best out of me. It is because of him this dissertation became possible. Before meeting Dr. Ram, I did not have much programming skills, but he took the patience to guide me and teach basics of programming. Many thanks to Evan Bollig, my colleague at NCAR and a friend, for his helpful discussions, especially for the tips he gave me on programming and Latex.

I would like to gratefully thank my esteemed advisor Dr. Vinod Kumar, director of Multi-physics Multi-scale Computational Modeling (MU2COM) Laboratory and asst. professor in mechanical engineering at UTEP, for supporting me in performing this research; and for the assistance he provided throughout my graduate studies. I would never have reached this level of success if it wouldn't have been for him initially taking me under his wing and entrusting his belief in me. Again, the amount of gratitude would not be enough for all he has done for me. I would also like to thank my other committee members, Dr. Rodrigo Romero and Dr. Andrzej Pownuk of computational science department at UTEP, for their assistance during the writing of this thesis. I would also like to acknowledge Dr. Leticia Velazquez, Director of CPS Program at UTEP, for the financial support provided during my doctoral studies.

Additionally, I want to thank The University of Texas at El Paso Program in Computa-

tional Science and Mechanical Engineering professors and staff for all their hard work and dedication, providing me the means to complete my degree and prepare for a career as a computational scientist.

Many thanks to Mari, Nithin, Sanjay and Ashvin for their company during my graduate studies. Finally, I would like to thank my family, for their support during my graduate studies, who have made my education a high priority from the beginning. Without them, I would not be where I am today.

This thesis was submitted to the supervising committee on July 2012.

Abstract

Atmospheric numerical modeling has been going through drastic changes over the past decade, mainly to utilize the massive computing capability of the petascale systems. This obliges the modelers to develop grid systems and numerical algorithms that facilitate exceptional level of scalability on these systems. The numerical algorithms that can address these challenges should have the local properties such as the high on-processor operation count and minimum parallel communication i.e., high parallel efficiency. They should also satisfy the following properties such as inherent local and global conservation, high-order accuracy, geometric flexibility, non-oscillatory advection and positivity preservation properties. The goal of this dissertation is to address these challenges using various high-order numerical methods.

As a possible solution to achieve the above mentioned desirable properties, I considered central-upwind finite-volume (C-FV) schemes, which are proven to be robust, simple and accurate in many research areas and practical applications. These numerical methods are a subset of Godunov-type methods, widely known for their simplicity and for solving hyperbolic conservation laws. But, these staggered central schemes may not provide a satisfactory resolution when small time steps are enforced by stability restrictions. To address this issue, the considered schemes have an upwind nature, in the sense that they are based on the one-sided local speeds of propagation. The central-upwind framework provides high-order accuracy by decreasing the numerical dissipation present in the staggered central schemes. This is the reason, these schemes are central-upwind schemes, but here throughout my present work, I refer them to as C-FV schemes. The construction in the proposed schemes is based on the use of the Courant-Friedrich-Levy (CFL) related local speeds of propagation and on integration over Riemann fans of variable sizes. This way, a non-staggered fully discrete central scheme is derived and is naturally reduced to a particularly simple semi-discrete form. Among the advantages of these schemes are that

they do not require Riemann solvers or characteristic decomposition and grid staggering. These characteristics make them different from upwind schemes and universal methods, so they are promising candidate for providing higher-order accuracy to solutions governed by conservative systems. However, little is known for their practicality to geoscience problems that are also governed by conservative systems.

In this work, I examine the performance of these high-order schemes. Based on existing knowledge from other fields, I chose five promising schemes that are expected to possess desired properties needed in atmospheric modeling. The five schemes considered are Kurganov-Petrova (KP), a third-order compact central Weighted Essentially Non-Oscillatory (WENO-33), a fifth-order WENO (WENO-5), combination of WENO-33 and WENO-5 (WENO-35), a fourth-order Kurganov-Liu (KL), for a linear transport problem on a two-dimension (2D) Cartesian plane and on sphere. I used the shallow water model on the sphere using the C-FV schemes.

The cubed-sphere computational grid system has been chosen in this research work. This type of grid system is very well suited for FV discretization, mainly because the underlying control-volumes (grid cells) are logically rectangular, facilitating an easy implementation. Moreover, the cubed-sphere grid system is free of polar singularities, and its grid uniformity leads to excellent parallel efficiency.

For numerical modeling of the transport of trace constituents in atmospheric models, a non-oscillatory positivity preserving solution is essential. Standard WENO schemes produce spurious oscillations in the numerical solution, to address this issue, I employed a Bound-Preserving filter, which restricts the numerical solution to be inside the initial upper and lower bounds and suppresses the spurious oscillations, an additional flux correction step, to achieve strictly positive-definite solution is also employed to remove any negative values produced by the C-FV schemes, I used these filters for KL scheme as well. Both these techniques are inexpensive and effective. I use either a third-order or fourth-order Strong Stability Preserving Runge-Kutta time stepping scheme based on the order of the spatial discretization. The numerical schemes are evaluated with several benchmark tests,

on a 2D Cartesian plane and cubed-sphere geometry for transport problem, that accentuate accuracy and conservation properties.

In this present work, I only extend three schemes out of five schemes considered for solving the transport equation, i.e. KL, WENO-5 and WENO-35 schemes to shallow water model, because it can be concluded from the results of transport problem on a cubed-sphere geometry that these three schemes perform better than the other schemes in terms accuracy and performance. For evaluating flux for shallow water model, I employ a different flux evaluation formula developed by Kurganov-Noelle-Petrova (KNP), since KNP flux evaluation is more accurate than the one used for transport problem. These three schemes are evaluated using the test suite that is accepted by the atmospheric sciences community.

Table of Contents

	Page
Acknowledgements	v
Abstract	vii
Table of Contents	x
List of Tables	xiii
List of Figures	xiv
Chapter	
1 Introduction	1
1.1 Outline	3
2 Overview and Background	5
2.1 Atmospheric Modeling	5
2.2 History of Numerical Methods for Atmospheric Modeling	6
2.3 Overview and Background of C-FV Schemes	8
3 C-FV Methods for the Transport Problem	12
3.1 Semi-Discrete Central Scheme in 1D	12
3.2 Semi-Discrete Central Scheme in 2D Space	17
3.3 C-FV Schemes Based on WENO Methods	21
3.3.1 Third-Order Compact 2D WENO	21
3.3.2 Fifth-Order WENO Scheme (WENO-5)	24
3.3.3 A Hybrid Central WENO Scheme (WENO-35)	25
3.4 A Fourth Order Kurganov Liu Scheme (KL)	26
3.5 Filters and Bound Preservation	26
3.6 Time Integration schemes	28
3.6.1 SSP-RK3 scheme	28
3.6.2 SSP-RK (5,4) Scheme	29

3.7	Discussion and Summary	30
4	2D Numerical Experiments	31
4.1	Solid-Body Rotation of a Smooth Function	32
4.2	Solid-Body Rotation of a Non-Smooth Function	34
4.3	Deformational Flow Test	38
4.4	Discussion and Summary	41
5	Numerical Experiments on the Cubed-Sphere Geometry	43
5.1	Cubed-Sphere Geometry	43
5.2	Discretizing the Advection Equation on a Cubed Sphere	46
5.2.1	Arrangement of Cells on a Cubed-Sphere	46
5.3	Ghost cells	47
5.4	Linear Transport Problem on the Cubed-Sphere	48
5.4.1	Solid-Body Rotation of a Cosine-Bell	49
5.4.2	Deformational Flow Test: Moving Vortices	52
5.4.3	Deformational Flow Test: Slotted-Cylinders	55
5.4.4	Deformational Flow Test: Twin Cosine-Bells	62
5.5	Discussion and Summary	62
6	The Shallow Water Model	65
6.1	Shallow water model	65
6.2	Shallow Water Model on the Cubed-Sphere	67
6.3	The FV Discretization of SWE	68
6.4	Treatment of discrete derivatives	70
6.5	Numerical experiments and Results	70
6.5.1	Steady state geostrophic flow	70
6.5.2	Zonal flow over an isolated mountain	74
6.5.3	Rossby-Haurwitz wave	77
6.6	Discussion and Summary	80
7	Conclusion and Future Work	81

7.1	Conclusion	81
7.2	Future Work	83
	References	85
Appendix		
A	Reconstruction and Other Details	94
A.1	2D Semi-Discrete C-FV Scheme Reconstruction Details	94
A.2	2D Fifth-Order WENO Scheme Reconstruction Details	96
A.3	2D KL Scheme Reconstruction Details	98
A.4	Constants for the SSP-RK (5,4) Scheme	99
A.5	Cubed-Sphere Geometry Details	99
A.6	Anti-Diffusive Flux Term	102
	Curriculum Vitae	103

List of Tables

3.1	Values of constants c_{km}	25
4.1	L_2 norms for 2D solid body rotation of a Gaussian hill.	31
5.1	Error norms for deformational-flow test with twin cosine-bells on a cubed sphere, with $N_c = 90$ and a CFL maximum value set to 0.50. All four C-FV schemes are used for the test.	63
6.1	Relative errors in the height field for steady state geostrophic flow ($\alpha = \pi/4$ and $t = 5$ days for KL scheme with a resolution of $40 \times 40 \times 6$ and a CFL of 0.50 is chosen.	71
6.2	Same as in Table. 6.1 but for WENO-5 scheme.	71
6.3	Same as in Table. 6.1 but for WENO-35 scheme.	71

List of Figures

3.1	Schematic of a 1D computational stencil, where the domain is partitioned into N_x cells $I_i = [x_{i-1/2}, x_{i+1/2}]$, with cell interfaces $x_{i\pm 1/2}$. The values of the solution are reconstructed from the cell-averages \bar{u}_i using a polynomial approximation. The left and the right limits of the solution at the interface $x_{i+1/2}$ are denoted by $L(-)$ and $R(+)$, respectively.	14
3.2	Schematic of a 1D Stencil used for the KP scheme and WENO-5 scheme in 1D. New updates for the cell average \bar{u}_i^{n+1} is computed at the central cell I_i	16
3.3	2D stencil for KP, WENO-35 and KL schemes. Thick lines indicate the 2D stencil for WENO-5 scheme. The dashed lines indicate the 2D stencil for WENO-33 scheme.	19
3.4	Schematic of a 2D control volume, where the fluxes are evaluated on the cell boundaries at eight points ('X' marks). Non-oscillatory reconstruction polynomials are used for the flux evaluation	20
3.5	The 2D compact stencil for WENO-33 scheme. Reconstruction procedure requires a 3×3 stencil for the quadratic reconstruction, and four sub-stencils employing 2×2 cells for the linear reconstructions.	22
4.1	Initial solution for test case, solid body rotation of smooth function. A gaussian hill is placed at the center of the 2D Cartesian plane.	32
4.2	Convergence plot for 2D Cartesian solid-body (Gaussian hill) after one full revolution. All the five schemes KP, WENO-33, WENO-5, WENO-35 and KL are used for the convergence plots. Here CFL (0.50) is kept constant for different number of cells.	33

4.3	Initial solution for test case: solid body rotation of non-smooth function. The initial data consists of a cosine cone and a square block, and they rotate around the center of axis of 2D Cartesian plane.	34
4.4	The solution after one revolution of Leveque data using KP scheme without limiter, a resolution of 40×40 , and CFL limit of 0.50 is used here. The aim of this figure is to illuminate the Gibbs phenomenon i.e. the spurious oscillations at the top and bottom of the square block, that are introduced into the solution if no limiter is used.	35
4.5	All the details are same as in Figure. 4.4, but a limiter is used in KP scheme to attain the solution. It can be clearly seen that the spurious oscillations are smoothened by the use of a limiter.	36
4.6	Numerical results of solid-body rotation of non-smooth function [36], after one revolution with CFL= 0.50 and $\Delta x = \Delta y = .025$ on a domain $\Omega = [-1, 1]^2$, using (a) KP scheme, (b) WENO-33 scheme, (c) WENO-5 scheme, (d) WENO-35 scheme (e) KL scheme. The numerical solution is represented by the solid lines in which the contour values are from 0.05 to 0.95 with increment of 0.1. Thick solid-lines represent the exact reference solution with a contour value of 0.05 and 0.75.	37
4.7	Numerical results of Deformational flow test mentioned in test case 3 with CFL=0.50, $\Delta x = \Delta y = .01$ on a 2D Cartesian domain, $\Omega = [0, 1]^2$ using WENO-35 scheme. The figure (a) shows the initial solution, and the panels (b), (c) and (d) show the defoemation of the initial solution at $T/4$, $T/2$, and $3T/4$ respectively.	39

4.8	Numerical results of deformational flow test at the final time T , with $CFL=0.50$, $\Delta x = \Delta y = .01$ on domain $\Omega = [0, 1]^2$, using different schemes (a) KP, (b) WENO-33, (c) WENO-5, (d) WENO-35 and (e) KL schemes. The numerical solution is represented by the solid lines in which the contour values are from 0.05 to 0.95 with increment of 0.1. Thick solid-lines represent the exact reference solution with a contour value of 0.05 and 0.75.	40
5.1	A cubed-sphere generated by equiangular central projection. Each face of the cubed-sphere is partitioned into $N_c \times N_c$ cells (control volumes) for the FV discretization, $6 N_c^2$ cells span the entire spherical surface.	44
5.2	Schematic showing orientation of the different cube faces and their local connectivity. The cube faces are marked as \mathcal{F}_n , $n = 1, \dots, 6$	45
5.3	Schematic of cell centers (FV cells) on a cubed-sphere geometry. In this figure each face has 10×10 cells and $10 \times 10 \times 6$ cells span the surface of the sphere.	47
5.4	Treatment of connectivity between each face for the cubed-sphere. The center points of ghost cells lie on the same line as the center points of cells on the neighboring face.	48
5.5	Results of cosine-bell advection test on the cubed-sphere after one revolution (12 days) with the WENO-35 scheme. The wind field is oriented along the north-east direction ($\alpha_0 = \pi/4$), on a $48 \times 48 \times 6$ grid (or $N_c = 48$), with $CFL = 0.25$. The panels (a) indicates the initial (cell-averaged) height of the cosine-bell, (b) numerical solution without any filter, (c) solution with BP filter and (d) solution with BP and PP filter.	51
5.6	Time traces of the normalized ℓ_2 error for the simulations in Figure 5.5. Different combinations of filters used with the WENO-35 scheme, and the BP filter enhances the accuracy of the scheme.	52

5.7	Time traces of the normalized errors ℓ_1 , ℓ_2 and ℓ_∞ for cosine-bell advection test. With (a) KP, (b) WENO-33, (c) WENO-5, (d) WENO-35 and (e) KL schemes. Flow is along north-east direction ($\alpha_0 = \pi/4$) on a cubed-sphere with $N_c = 90$ (1° resolution), and CFL = 0.25 for all simulations. Note that y -axis scaling for KP scheme is different from that of the WENO schemes.	53
5.8	Numerical solution with WENO-35 scheme for the moving vortices test. (a) Initial vortex field, (b) solution at halftime (6 days) and (c) solution at after full evolution (12 days). The vortices move along north-east direction ($\alpha_0 = \pi/4$) while evolving. A cubed-sphere with $N_c = 80$ and CFL = 0.25 is used for the simulation.	54
5.9	Height errors (numerical - analytic) after a revolution with the moving vortices test on $80 \times 80 \times 6$ grid. (a) KP, (b) WENO-33, (c) WENO-5 and (d) WENO-35 schemes, other experiment setting is same as in Figure. (5.8).	56
5.10	Time evolution of the normalized error norms ℓ_1 , ℓ_2 and ℓ_∞ for (a) KP, (b) WENO-33, (c) WENO-5, (d) WENO-35 and (e) KL schemes. All other settings are same as in Figure 5.8. Note that y -axis scaling for WENO-5, KL and WENO-35 are different from that of KP and WENO-33.	58
5.11	Numerical solution for the deformational flow test on a cubed sphere with mesh $90 \times 90 \times 6$ with twin slotted cylinders as initial condition. The initial solution is shown in the panel (a), these two cylinders move along the zonal direction while deforming, and reach at the initial position after making a complete revolution (12 days). Panels (b) and (d) show the solution after time $T/2$ and T ($=5$) respectively using WENO-35 scheme, and panel (c) shows the solution after time $T/2$ using WENO-5 scheme. A CFL of 0.75 is used for the simulation.	59
5.12	Same as in Figure 5.11, but the panels (a), (b), (c) and (d) indicate the solution after one cycle of revolution using KP, WENO-33, WENO-5 and WENO-35 schemes respectively.	60

5.13	A performance comparison of WENO schemes with respect to the KP scheme for the slotted-cylinder test, execution time and ℓ_2 error measure are used for this comparison. The solid-line indicates execution time comparison, estimated as the ratio of the time taken by KP scheme and the time taken by each scheme. Similarly, the dashed line indicates ℓ_2 error comparison, estimated as the ratio of ℓ_2 error of KP scheme and ℓ_2 error of each scheme. It shows that KL and WENO-5 are more efficient and accurate than other three central schemes, while WENO-33 is most computationally expensive.	62
6.1	Schematic of shallow water model, which consists of a thin sheet of fluid of thickness h and h_s is the height of underlying mountains.	66
6.2	Height errors (Numerical - Analytic) after 5 days with steady state geostrophic flow test on $40 \times 40 \times 6$ grid, and a CFL of 0.50 is chosen. (a) Initial height field, (b) KL, (c) WENO-5 and (d) WENO-35. Contour lines for (b), (c), and (d) are plotted from -2.0 to 2.0 with an interval of 0.2 m.	73
6.3	Numerical solution for the zonal flow over an isolated mountain test on $40 \times 40 \times 6$ grid and CFL = 0.50 with flow angle $\alpha = 0$. Contour levels are from 5050 m to 5950 m in intervals of 50 m. The top, middle and bottom rows represents the solution obtained by KL, WENO-5 and WENO-35 schemes respectively, the left and right columns represents the solution at 5 and 15 days respectively.	75
6.4	Numerical solution of vorticity field for the zonal flow over an isolated mountain test, experiment settings are same as in Figure 6.3. Contour levels are from (-3 to 3 in intervals of .50) $\times 10^{-5}$. The top, middle and bottom rows represents the solution obtained by KL, WENO-5 and WENO-35 schemes respectively, the left and right columns represents the solution at 5 and 15 days respectively.	76

6.5	All the experiment settings are same as in Figure. 6.3. Evolution of the normalized conservation errors of potential enstrophy (left) and total energy (right).	77
6.6	All the experiment settings are same as in Figure. 6.7, except the grid resolution is $40 \times 40 \times 6$. Evolution of the normalized conservation errors of potential enstrophy (left) and total energy (right).	78
6.7	Numerical solution for the Rossby-Haurwitz wave test on $48 \times 48 \times 6$ grid and CFL = 0.50 with flow angle $\alpha = 0$. Contour levels are from 8100 m to 10500 m in intervals of 100 m. The top, middle and bottom rows represents the solution obtained by KL, WENO-5 and WENO-35 schemes respectively, the left and right columns represents the solution at 7 and 14 days respectively.	79
A.1	Illustration of gnomonic mapping between sphere with radius R and the inscribed cube with side of length $2a$. One-eighth of the cube is shown here. A point on the cube face P_1 is marked by a solid square with local Cartesian coordinates (x^1, x^2) , and the corresponding point on the sphere is marked by a solid circle with absolute Cartesian coordinates (X, Y, Z) . The spherical polar coordinates, longitude and latitude, are λ and θ respectively. r is the radial distance from the center to any point on the cube face (Note: Figure is taken from [52].	100

Chapter 1

Introduction

In the past few decades, supercomputing in general have evolved enormously. Far from Control Data Corporation's single-operation scalar processors in the 1960s, to present day petascale computers that are believed to be capable of performing one quadrillion floating-point operations per second. To utilize this massive computing potential available, atmospheric modelers are obliged to develop grid systems and numerical algorithms that can facilitate exceptional level of scalability on these parallel petascale systems. For this reason atmospheric numerical modeling has been going through drastic changes over the past decade [53]. The ideal numerical algorithms that can address these challenges should possess the local properties such as high on-processor operation count and minimum parallel communication i.e. high parallel efficiency. The numerical method should also satisfy the following properties [46] such as:

- Inherent local and global conservation,
- High-order accuracy,
- Geometric flexibility,
- Non-oscillatory property,
- Monotonicity,
- Positivity preservation.

Conservation of mass is an essential feature that an atmospheric numerical method should possess [33]. For example, ensuring conservation of mass prevents the surface pressure from drifting to highly unrealistic values in long-term integrations of atmospheric

models. One can obtain this feature in a numerical scheme mainly by two ways, either by an inherently conservative numerical method or by using mass fixers. Conservation of total energy, momentum etc. are also important features for a numerical method. If there are no new local extrema are generated and the absolute values of pre-existing local extrema is non-increasing then this is termed as monotonicity preserving [18]. Strict monotonicity preservice is hard to achieve. The numerical schemes for atmospheric modeling should not produce negative values in the solution, i.e. the solution has to be strictly positive. The schemes should not produce oscillations (Gibbs phenomenon) in the solution, and this property is called as non-oscillatory (no maxima or minima) property. The scheme that is monotone is positive-definite and non-oscillatory but it is not necessarily true vice-versa.

To achieve these desired properties, I consider finite-volume (FV) based discretization techniques, these type of techniques are becoming increasingly popular for developing new generations of atmospheric and ocean numerical models. The FV methods offer inherent conservation properties and geometric flexibility to adapt complex grid systems, and have the potential to exploit current petascale computers. Explicit FV schemes are relatively easy to implement and they have lenient Courant-Friedrichs-Lewy (CFL) stability limit as opposed to conservative methods such as the discontinuous Galerkin (DG) method with given order of accuracy [50]. The FV methods can be applied to a wide range of problems governed by conservative systems (partial differential equations) that can be written in integral control-volume form (flux form) over a domain. Two effective and inexpensive filters are employed here in the present work to achieve strictly-positive solution and to preserve the bounds of the initial solution.

Design or choice of the grid system for the computational domain also plays a vital role in overall efficiency of the modern FV based model. For example, the global FV climate model based on conventional latitude-longitude spherical grid system [11] has a stringent limitation to scale to massively parallel machines with processor count ranging from tens to hundreds of thousands. Because of the computational problems (including scalability issues) associated with the polar singularities, latitude-longitude grid system

is not considered for next generation global modelling systems. Other choices for global grid systems which can provide quasi-uniform grid structures (control-volumes) are the icosahedral hexagonal grid [69], Yin-Yang grid [58] and cubed-sphere grid [63].

However, the cubed-sphere grid system is very well suited for FV discretization, because the underlying control-volumes (grid cells) are logically rectangular, facilitating an easy implementation. Moreover, the cubed-sphere grid system is free of polar singularities, and its grid uniformity leads to excellent parallel efficiency [60, 76]. Recently, a number of high-order FV schemes on cubed-sphere have been developed (see, [59, 7, 6, 71]). Cubed-sphere grid system is adopted for the proposed global FV schemes.

In this work, I solve the transport (advection) problem on the 2D Cartesian plane and on the cubed-sphere geometry using the proposed C-FV schemes, I demonstrate the performance of these schemes by using a standard test suite for transport schemes accepted by the atmospheric modeling community, the test suite consists of various solid-body rotation and deformational flow tests. The transport C-FV schemes are then extended to shallow water model on cubed-sphere grid. In modeling of the global atmospheric flows, the shallow water equations on sphere are considered to be the standard test problems. Williamson et al. [75] standardized a suite of tests for global shallow water models, which are employed to study the C-FV schemes on a cubed-sphere. The shallow water equations are only a first test because they don't represent the whole atmospheric system [67], but intently imitates the atmospheric flow in a single layer. The results for different schemes are compared, and are also compared with the results for the same tests for various schemes available in literature.

1.1 OUTLINE

The present material is organized as following: In chapter 2, I discuss about the history of the atmospheric modeling and numerical methods for atmospheric modeling followed by the overview and background of the C-FV schemes.

Chapter 3 discusses the methodology of the C-FV schemes, detailed description is given

about the 1D KP scheme and brief description of 2D KP scheme is mentioned. Third order compact 2D WENO methodology is given followed by a 1D description of WENO-5 is presented. The combination procedure of WENO-33 and WENO-5 to attain WENO-35 scheme is mentioned and the details of fourth order KL scheme is discussed. The filters used to preserve positivity and bounds are also explained herein. Finally, the time integration schemes utilized in this present work are discussed in this chapter.

In chapter 4, the details of the numerical experiments and the results attained by all the different schemes is given. The tests considered are classified into two types, i.e. solid body rotation and deformational test cases.

Chapter 5 discusses the cubed-sphere geometry and shows how the transformations are done between a cube and a cubed-sphere geometry. The methodology considered to patch the cube faces is given here in this chapter. I also present the details of different test cases considered to test the performance of the C-FV schemes on a cubed-sphere geometry with the results.

Chapter 6 introduces the shallow water equations on the cubed-sphere. Again, I test the C-FV schemes using different tests whose details and results are presented in this chapter.

Concluding remarks and future work are given in chapter 7.

Chapter 2

Overview and Background

The ensuing material in this chapter is divided into the following: Firstly, I talk about the evolution of atmospheric modeling. Secondly, a brief overview of numerical methods for atmospheric modeling is given, different schemes considered by the atmospheric modelers in the past is mentioned. Finally, the overview and background of C-FV schemes is mentioned.

2.1 ATMOSPHERIC MODELING

The quest for weather forecasting led to the development of atmospheric sciences. For predicting the behavior of atmosphere in 1860s Robert FitzRoy used telegraph systems to relay local weather information between base stations across Europe. In the early 20th century, Lewis Fry Richardson developed a complete numerical system for weather forecasting, which is termed as numerical weather forecasting (or atmospheric modeling using numerical methods). The work by Richard was ignored because of the complexity of the method and lack of computing power, until the 1940s. But by 1950, Jule Gregory Charney developed the first successful numerical weather prediction model on Electronic Numerical integrator and Computer (ENIAC) ([41]). The first atmospheric general circulation model was developed by Norman Phillips in 1955. In 1966, West Germany and the United States began producing operational forecasts based on primitive-equation models, followed by the United Kingdom in 1972 and Australia in 1977. The development of global forecasting models led to the first climate models. The development of limited area (regional) models facilitated advances in forecasting the tracks of tropical cyclone as well as air quality in the 1970s and 1980s. Since then, the numerical models for weather predictions ([34] [40]) have become more elaborate and the computing power has grown immensely.

Apart from weather forecasting, there are many other applications of atmospheric modeling including climate predictions, seasonal to decadal predictions attribution of climate changes etc. There is a need for improving the quality of predictions either by increasing the spatial resolution, or by adding more physical phenomenon, or by using more accurate numerical models, etc. This dissertation focuses on the dynamical core component of general circulation models (GCMs). The dynamical core is an essential component of any large-scale model and is responsible for the solution of the fluid equations. Here, I focus on developing new technologies for atmospheric modeling, which also includes implementing methodologies existing in other fields, which have been proven to be robust, efficient and accurate.

2.2 HISTORY OF NUMERICAL METHODS FOR ATMOSPHERIC MODELING

Over the past two decades, Global Spectral Transform methods have dominated in climate simulation [21]. Spherical harmonics spectral methods provide a completely isotropic representation of a scalar function on the sphere with higher accuracy. However, the spectral transform methods have disadvantages, monotonicity and positivity are not guaranteed, and the dispersive errors mainly occurred near the regions where the solutions are not perfectly smooth in the spectral model. This can lead to Gibbs phenomenon and so there is a need to damp high-frequency waves explicitly. Global methods based on spherical harmonic basis functions have difficulty exploiting the full potential of current petascale systems, due to the expensive non-local communication operations.

In recent years, researchers have focused on local methods [43], which adapt favorably to parallel systems [12] [42]. The quest for a positive and accurate scheme led to an increase in the popularity of high-order methods, the spectral element (SE) methods that are high-order methods, have become more popular during this era [68]. Spectral elements combine the accuracy of conventional spectral methods and the geometric flexibility of finite element methods. The SE method is not inherently conservative [42] because it is

not based on conservation laws. For atmospheric applications, the exact conservation of integral invariants such as mass and energy is crucial. It is very crucial to have atmospheric models based on conservative numerical methods; it has been shown that the models that are not based on conservation tend to lose mass over a period of time [44].

Recently, Discontinuous Galerkin (DG) methods gained a lot of popularity in atmospheric modeling, these are based on conservation laws which are hybrid approaches that combine properties from both finite element and finite volume methods. Cockburn et al. constructed a DG method, a high-order conservation algorithm for the non-linear systems of conservation laws [9]. Nair et al. [51] developed a conservative transport scheme on a cubed-sphere using the DG method and extended for the shallow water model. There is a need for a slope limiter in DG method, if the solution contains large discontinuities. There are no known efficient limiters for multi-dimensional DG methods of polynomial order greater than 4. The capability of the conventional slope limiter to control spurious oscillation diminishes as the order of the polynomial increases [20]. This limits the applicance of high-order DG method in atmospheric modeling. The DG methods have stringent limitation on the CFL stability limit.

In atmospheric modeling, finite volume methods are a popular approach, these methods ensure conservation in atmospheric models. They treat the equations in flux-form with control volumes, obtaining conservation through careful discretization of the control volume fluxes. Wang and Liu [74] developed a conservative high-order spectral finite volume (SFV) method for the solution of 2D systems of conservation laws. SFV method is based on classical finite volume scheme and applied to each cell appearing in a spectral element, with the reconstruction based on a high-order method. It is easy to incorporate traditional multidimensional limiters in a finite volume approach. Choi et al. [8] developed a SFV method for the numerical solution of the shallow water equations. A flux-corrected transport (FCT) scheme is incorporated to enforce monotonicity near strong discontinuities or under-resolved gradients. Vani et al. [7], in their work developed a SFV scheme for transport equation. SFV scheme employs rectangular elements with high-order nodal dis-

cretization based on GaussLobattoLegendre points [23]. Recently, a number of high-order FV schemes on cubed-sphere have been developed (see, [59, 6, 71]).

2.3 OVERVIEW AND BACKGROUND OF C-FV SCHEMES

A large class of FV methods for solving hyperbolic conservation laws are based on high-order extensions of the Godunov scheme [16], collectively known as the Godunov-type schemes [70]. Godunov's scheme is a conservative numerical scheme used for solving partial differential equations. These type of schemes are projection-evolution methods, the conservative variables are considered as piecewise constant over the grid cells at every time step and the time evolution is determined by the exact solution of the Riemann problem at the inter-cell boundaries [15]. These schemes essentially have three basic steps in the solution process:

1. Reconstruction: piecewise polynomials are reconstructed over the grid cells spanning the domain from known cell-averages (piecewise constant data) from the previous time level.
2. Evolution: The reconstructed interpolant is evolved in time according to considered conservation laws.
3. Projection: New cell-averages are computed on each cell by projecting the evolved polynomials onto cell-averages.

Depending on the final (projection) step, the Godunov type of schemes are classified into two types:

1. Upwind: This type of schemes employ Riemann solvers to resolve discontinuity at cell interfaces, this requires characteristic information of the wave propagation at the discontinuity (Riemann fans), often resulting in a complex and expensive upwind algorithm. Note that exact Riemann solvers do not exist for many practical problems,

and approximate Riemann solvers are often computationally expensive and require characteristic decomposition of the hyperbolic problem. The MUSCL scheme (Monotone Upstream-centred Schemes for Conservation Laws) by Van Leer et al. [73], and the PPM (Piecewise parabolic Method) by Colella et al. [10] are respectively, second- and third-order examples of upwind schemes.

2. Central: These schemes do not require characteristic decomposition or Riemann solvers, and the projection operation is done by averaging over the Riemann fans; this procedure makes central schemes simple and easy to implement. The classic Lax-Friedrichs scheme is the first-order (very dissipative) central scheme. Its second-order sequel was developed by Nessyahu et al. [54], this scheme is fully discretized and employs a staggered grid. A major issue with fully discretized central scheme is that it is diffusive, and higher than second-order extension is cumbersome due to grid staggering. The advantage of the higher-order schemes is that they reduce the excessive numerical viscosity, typical for the Lax-Friedrichs scheme, and give much sharper resolution of the shocks and rarefactions. However, a semi-discretized (continuous in time) central scheme does not require Riemann solvers or staggered grid while being accurate [31]. Semi-discretized formulations give more flexibility for choosing ODE (ordinary differential equation) solvers, resulting from the spatial discretization, for high-order temporal accuracy and increased CFL stability limit.

Central schemes are used to solve non-linear advection-diffusion equations. These schemes can be implemented in a straight forward manner as black-box solvers to solve various general conservation laws and related equations governing the spontaneous evolution of large gradient phenomena, therefore the central schemes can be considered as universal finite-difference methods. The central schemes available today are originated from the first-order Lax-Friedrichs scheme, which was developed by Lax [35]. This is a numerical method for the solution of hyperbolic partial differential equations based on finite differences. The method can be described as the forward in time and centered in space (FTCS) scheme.

Nessyahu et al. in their work, [54] presented a family of non-oscillatory, second order, central difference approximations to nonlinear systems of hyperbolic conservation laws. These approximations can be viewed as natural extensions of the first-order Lax-Friedrichs (LxF) scheme. This scheme offers high resolution while retaining the simplicity of the Riemann-solver-free approach. Liu et al. developed a third order, non-oscillatory central difference scheme for the approximate solution of non-linear systems of hyperbolic conservation laws [39]. This scheme is the extension of first order Lax-Friedrichs scheme and second order central scheme of Nessayhu and Tadmor (NT).

The examples given for central schemes do not provide good resolution when small steps are enforced, and they do not admit semi-discrete form. These difficulties are resolved in the scheme constructed in Kurganov et al. [31], In the new construction of this scheme, the evolution step is executed by integrating over non-equal control volumes, here the sizes are proportional to the local speeds of propagation. The evolved solution is then projected back onto the original grid, which requires an additional piecewise polynomial reconstruction. This ensures, a non-staggered fully-discrete central scheme. This is therefore reduced to a semi-discrete scheme. The multidimensional semi-discrete scheme in [31] was obtained by so called dimension-by-dimension approach.

Several high-order semi-discretized central schemes were developed more than a decade ago [39, 31, 13, 26]. These schemes have computationally attractive features such as low dissipation and non-oscillatory properties. However, I am particularly interested in a semi-discrete formulation, the so-called *central-upwind* scheme proposed by [30], hereafter referred to as KP (central) scheme. For the KP scheme, flux computation is based on local speeds of propagation and the reconstruction relies on non-oscillatory quadratic polynomials employing regular non-staggered grids. This scheme has an upwind flavor since the CFL related local speed of wave propagation is utilized in the projection step for integration over Riemann fans. It is a good compromise between the classical upwind and central schemes. Recently, the KP scheme was used for a multilevel ocean shallow-water model [1].

The spatial order of accuracy as well as non-oscillatory property of C-FV scheme de-

depends on the reconstruction polynomials. The KP scheme uses quadratic reconstruction polynomials with built-in limiters to control spurious oscillations. However, the high-order Weighted Essentially Non-Oscillatory (WENO) method [38] can be exploited in the reconstruction stage as showed in [13]. The WENO schemes are based on the essentially non-oscillatory (ENO) schemes originally introduced by [19]. The WENO philosophy of [22] involves a weighted sum of polynomials where the least oscillatory polynomials are weighted the highest, which results in a class of robust reconstruction procedure. In order to improve the spatial accuracy and monotonic limiting properties, I replace the quadratic reconstruction polynomials in KP scheme with high-order WENO-based and KL [28] reconstruction polynomials. These reconstruction polynomials optionally use positivity-preserving and bound preserving filters.

Chapter 3

C-FV Methods for the Transport Problem

Conservative transport (advection) plays a vital role in atmospheric dynamics, especially on the global scale where quantities such as potential vorticity and geostrophic height are naturally conserved. In this chapter, the methodology of the C-FV schemes and discretization of transport equation in 1D and on 2D Cartesian plane, a detailed explanation for 1D Kurganov-Petrova (KP) [30] scheme and a brief description for 2D framework are described. The other four schemes that are considered are explained here in this chapter are a third-order compact central Weighted Essentially Non-Oscillatory (WENO-33) [13], a fifth-order WENO (WENO-5) [64], combination of WENO-33 and WENO-5 (WENO-35), and a fourth-order Kurganov-Liu (KL) [28]. The bound preserving and positivity filters are elucidated here in this chapter. The details of the time integration schemes used for the present work are also mentioned.

3.1 SEMI-DISCRETE CENTRAL SCHEME IN 1D

A 1D scalar conservation law is considered to explain the methodology of 1D KP scheme, as follows:

$$\frac{\partial u}{\partial t} + \frac{\partial f(u)}{\partial x} = 0, \quad \text{in } \Omega \times (0, T] \quad (3.1)$$

where $u = u(x, t)$ is a scalar (conservative) quantity which is subjected to the initial condition $u(x, 0) = u_0(x)$. For simplicity, the domain Ω is assumed to be periodic and is partitioned into N_x non-overlapping cells I_i of equal length such that $I_i = [x_{i-1/2}, x_{i+1/2}]$, $i = 1, \dots, N_x$. The cell interfaces (edges) are defined by $x_{i\pm 1/2}$, with cell width $\Delta x_i = (x_{i+1/2} - x_{i-1/2})$, and the cell centers are defined to be $x_i = (x_{i+1/2} + x_{i-1/2})/2$. Figure 3.1 depicts the 1D computational domain. The time discretization is denoted by $t^n = n\Delta t$,

where n represents a time level and Δt is the time step.

The central schemes for conservation laws can be derived by representing Equation. (3.1) in its integral form. For that, the cell averages $\bar{u}(x, t)$ are defined as follows:

$$\bar{u}(x, t) = \frac{1}{\Delta x} \int_{x-\Delta x/2}^{x+\Delta x/2} u(x, t) dx \quad (3.2)$$

By integrating Equation. (3.1) over a cell $I(x)$ for a time interval $[t, t + \Delta t]$ yields:

$$\begin{aligned} \bar{u}(x, t + \Delta t) &= \bar{u}(x, t) - \frac{1}{\Delta x} \times \left[\int_{\tau=t}^{t+\Delta t} f(u(x + \frac{\Delta x}{2}, \tau)) d\tau \right. \\ &\quad \left. - \int_{\tau=t}^{t+\Delta t} f(u(x - \frac{\Delta x}{2}, \tau)) d\tau \right] \end{aligned} \quad (3.3)$$

Reconstruction is a crucial step for FV discretization, for which the solution $u(x, t)$ at a time level $t = t^n$ is approximated to polynomial functions in a piecewise manner on every cell I_i . For a typical r^{th} -order accurate FV scheme, the reconstruction polynomial can be written as:

$$p(x, t^n) = u(x, t^n) + \mathcal{O}((\Delta x)^r).$$

However, for FV formulation, the known discrete cell-averages $\bar{u}(x_i, t^n) = \bar{u}_i^n$ are used for reconstructing piecewise polynomials $p_i^n(x)$ on each cell I_i . Because of the piecewise nature, the polynomials are discontinuous at the cell interfaces $x_{i\pm 1/2}$. The reconstructed polynomials (or subgrid-scale distribution) are subject to the following constraint, which guarantees conservation:

$$\bar{u}_i^n = \frac{1}{\Delta x} \int_{x_{i-1/2}}^{x_{i+1/2}} p_i^n(x) dx. \quad (3.4)$$

In general, the new estimates of cell average \bar{u}_i^{n+1} is computed from a discrete analog of Equation. (3.3), using \bar{u}_i^n and corresponding reconstructed values.

The integral form in Equation. (3.3) can be used for formulating a variety of Godunov-type fully discretized FV schemes. This is done by choosing appropriate value for x and approximating the time integrals. For example, by choosing $x = x_i$ results in an upwind based FV method (e.g., MUSCL) where $\bar{u}(x)$ is predicted at the cell centres and Riemann

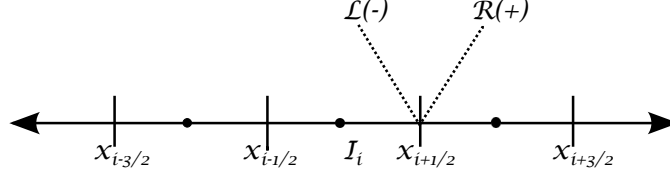


Figure 3.1: Schematic of a 1D computational stencil, where the domain is partitioned into N_x cells $I_i = [x_{i-1/2}, x_{i+1/2}]$, with cell interfaces $x_{i\pm 1/2}$. The values of the solution are reconstructed from the cell-averages \bar{u}_i using a polynomial approximation. The left and the right limits of the solution at the interface $x_{i+1/2}$ are denoted by $L(-)$ and $R(+)$, respectively.

solvers are employed to resolve discontinuities of the reconstructed values at the cell interfaces. Alternatively, by choosing $x = x_{i+1/2}$ and approximating time integrals results in fully discretized central schemes (e.g., [54]) where $\bar{u}(x)$ is predicted at the cell interfaces. This type of C-FV schemes are free from Riemann solvers but a staggered grid is required to project the updated values to the cell centers. The main focus here is on semi-discretized KP scheme. First, I briefly outline the 1D scheme to introduce basic ideas. The details including theoretical discussions of KP scheme can be found in [30].

After rearranging the Equation. (3.3) and applying the following limit:

$$\frac{d}{dt} \bar{u}_i(t) = \lim_{\Delta t \rightarrow 0} \left(\frac{\bar{u}_i^{n+1} - \bar{u}_i^n}{\Delta t} \right) \quad (3.5)$$

the r^{th} order semi-discretized central scheme is obtained, and is given by:

$$\frac{d}{dt} \bar{u}_i(t) = - \frac{H_{i+1/2}(t) - H_{i-1/2}(t)}{\Delta x} \quad (3.6)$$

where $H_{i\pm 1/2}(t) = H(x_{i\pm 1/2}, t)$ is the numerical flux defined at the cell interfaces. At the (right) interface,

$$H_{i+1/2}(t) = \frac{f(u_{i+1/2}^+(t)) + f(u_{i+1/2}^-(t))}{2} - \frac{a_{i+1/2}(t)}{2} [u_{i+1/2}^+(t) - u_{i+1/2}^-(t)] \quad (3.7)$$

where $u_{i+1/2}^\pm(t)$, are the cell interface values from the right (+) and the left (-) of the interface at $x_{i+1/2}$ (see, Figure 3.1). $a_{i+1/2}(t)$ is the local maximum speed derived from the

flux Jacobian $\partial f / \partial u$. If Equation. (3.1) represents a linear transport problem, $a_{i+1/2}(t)$ is then simply the local maximum wind speed. In that case, $f(u) = a u$, and Equation. (3.7) is same as the local Lax-Friedrichs or Russanov flux, which is widely used for the DG methods [9]. There are several flux formulae with increasing complexity available, however, I consider only the simple flux formula (3.7) in this work.

The interface values $u_{i+1/2}^\pm(t)$ can be written in terms of the reconstruction polynomials as follows:

$$u_{i+1/2}^+(t) = p_{i+1}^n(x_{i+1/2}), \quad u_{i+1/2}^-(t) = p_i^n(x_{i+1/2}).$$

The KP scheme is specifically designed to attain a third-order non-oscillatory scheme, therefore, the piecewise polynomials can be decomposed into linear (L_i^n) and quadratic function (q_i^n) combined with a limiter function θ_i^n , as follows:

$$p_i^n(x) = (1 - \theta_i^n)L_i^n(x) + \theta_i^n q_i^n(x), \quad 0 < \theta_i^n < 1. \quad (3.8)$$

where the linear and quadratic functions are defined as,

$$L_i^n(x) = \bar{u}_i^n(x) + s_i^x(x - x_i), \quad (3.9)$$

$$q_i^n(x) = \left[\bar{u}_i^n(x) - \frac{(\Delta x)^2}{24} D_+ D_- \bar{u}_i^n(x) \right] + D_0 \bar{u}_i^n(x - x_i) + \frac{1}{2} D_+ D_- \bar{u}_i^n(x - x_i)^2. \quad (3.10)$$

In Equation. (3.9), s_i^x is the slope after applying a *minmod* limiter [73] to suppress oscillations; D_- , D_0 and D_+ in Equation. (3.10) are the backward, centered and forward finite-difference operators, respectively.

The *minmod* function, which limits the slope (s_i^x) of the linear function $L_i^n(x)$, is defined as follows:

$$s_i^n = \minmod \left(\frac{\bar{u}_i^n - \bar{u}_{i-1}^n}{\Delta x}, \frac{\bar{u}_{i+1}^n - \bar{u}_i^n}{\Delta x} \right),$$

and

$$\minmod(a, b) = \frac{\text{sign}(a) + \text{sign}(b)}{2} \min\{|a|, |b|\}. \quad (3.11)$$

The limiter function θ_i^n used in KP scheme is defined as follows:

$$\theta_i^n = \begin{cases} \min(M^+, m^-, 1) & \text{if } \bar{u}_{i-1}^n < \bar{u}_i^n < \bar{u}_{i+1}^n \\ \min(M^-, m^+, 1) & \text{if } \bar{u}_{i-1}^n > \bar{u}_i^n > \bar{u}_{i+1}^n \\ 1 & \text{otherwise} \end{cases}$$

where

$$\begin{aligned} M^+ &= \frac{M_{i+1/2}^n - L_i^n(x_{i+1/2})}{M_i^n - L_i^n(x_{i+1/2})}, & M^- &= \frac{M_{i-1/2}^n - L_i^n(x_{i-1/2})}{M_i^n - L_i^n(x_{i-1/2})}, \\ m^+ &= \frac{m_{i+1/2}^n - L_i^n(x_{i+1/2})}{m_i^n - L_i^n(x_{i+1/2})}, & m^- &= \frac{m_{i-1/2}^n - L_i^n(x_{i-1/2})}{m_i^n - L_i^n(x_{i-1/2})}, \\ M_i^n &= \max\{q_i^n(x_{i+1/2}), q_i^n(x_{i-1/2})\}, & m_i^n &= \min\{q_i^n(x_{i+1/2}), q_i^n(x_{i-1/2})\}, \\ M_{i\pm 1/2}^n &= \max\{(L_i^n(x_{i\pm 1/2}) + L_{i\pm 1}^n(x_{i\pm 1/2}))/2, q_{i\pm 1}^n(x_{i\pm 1/2})\}, \\ m_{i\pm 1/2}^n &= \min\{(L_i^n(x_{i\pm 1/2}) + L_{i\pm 1}^n(x_{i\pm 1/2}))/2, q_{i\pm 1}^n(x_{i\pm 1/2})\}. \end{aligned}$$

It can be shown that the non-oscillatory reconstruction (given in Equation. (3.8)) satisfies the conservation constraint Equation. (3.4). The computational stencil required for the 1D KP scheme (with limiters) is 5 cell-wide (see Figure. 3.2) including the cell in question, located at the center, and comparable to that of the upwind-based piecewise parabolic method (PPM) in [10].

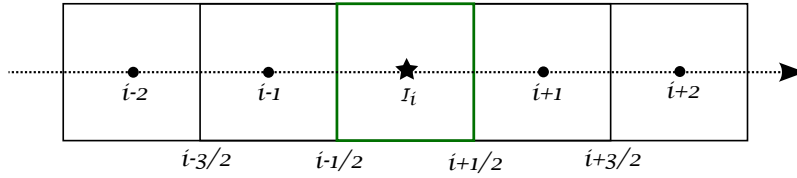


Figure 3.2: Schematic of a 1D Stencil used for the KP scheme and WENO-5 scheme in 1D. New updates for the cell average \bar{u}_i^{n+1} is computed at the central cell I_i .

Once the numerical fluxes in the right side of the ordinary differential equation (ODE) (3.6) are computed using Equation. (3.7) and (3.8), the ODE can be solved for the cell-averages \bar{u}_i^n at the next time-level t^{n+1} , by a variety of numerical methods. The ODE

solvers used for this work are discussed in Section. (3.6). This completes the description of the 1D KP scheme, which is a basic ingredient for developing the 2D KP scheme.

3.2 SEMI-DISCRETE CENTRAL SCHEME IN 2D SPACE

In order to describe various 2D central schemes, Firstly, I consider the following conservation law on (x, y) Cartesian plane as follows:

$$\frac{\partial u}{\partial t} + \frac{\partial F(u)}{\partial x} + \frac{\partial G(u)}{\partial y} = 0, \text{ in } \Omega \times (0, T], \quad (3.12)$$

where $u = u(x, y, t)$ is a conservative quantity with initial value $u_0 = u(x, y, 0)$, $F(u)$ and $G(u)$ are the flux functions in the x and y directions, respectively. The domain Ω is assumed to be rectangular and doubly periodic with non-overlapping rectangular cells $I_{ij} = [x_{i-1/2}, x_{i+1/2}] \otimes [y_{i-1/2}, y_{i+1/2}]$, with the grid-spacings Δx and Δy . Other definitions are similar to that already described in 1D case.

The 2D semi-discrete scheme can be derived analogous to the 1D case as follows [30],

$$\frac{d}{dt} \bar{u}_{ij}(t) = - \frac{H_{i+1/2,j}^x(t) - H_{i-1/2,j}^x(t)}{\Delta x} - \frac{H_{i,j+1/2}^y(t) - H_{i,j-1/2}^y(t)}{\Delta y} \quad (3.13)$$

where H^x and H^y are numerical fluxes at the cell walls along the x and y directions, respectively. The numerical fluxes on east edge $x_{i+1/2,j}$ and $y_{i,j+1/2}$ of the cell is given by:

$$\begin{aligned} H_{i+1/2,j}^x(t) = \frac{1}{12} & \left\{ F(u_{i+1,j}^{NW}(t)) + F(u_{ij}^{NE}(t)) + 4(F(u_{i+1,j}^W(t)) + F(u_{ij}^E(t))) + \right. \\ & \left. F(u_{i+1,j}^{SW}(t)) + F(u_{ij}^{SE}(t)) \right\} - \frac{a_{i+1/2,j}^x(t)}{12} \times \left[u_{i+1,j}^{NW}(t) - \right. \\ & \left. u_{ij}^{NE}(t) + 4(u_{i+1,j}^W(t) - u_{ij}^E(t)) + u_{i+1,j}^{SW}(t) - u_{ij}^{SE}(t) \right], \end{aligned}$$

$$\begin{aligned}
H_{i,j+1/2}^y(t) = \frac{1}{12} & \left\{ F(u_{i,j+1}^{SW}(t)) + F(u_{ij}^{NW}(t)) + 4(F(u_{i,j+1}^S(t)) + F(u_{ij}^N(t))) + \right. \\
& \left. F(u_{i,j+1}^{SE}(t)) + F(u_{ij}^{NE}(t)) \right\} - \frac{a_{i,j+1/2}^y(t)}{12} \times \left[u_{i,j+1}^{SW}(t) - \right. \\
& \left. u_{ij}^{NW}(t) + 4(u_{i,j+1}^S(t) - u_{ij}^N(t)) + u_{i,j+1}^{SE}(t) - u_{ij}^{NE}(t) \right]. \quad (3.14)
\end{aligned}$$

where $a_{i+1/2,j}^x(t)$ and $a_{i,j+1/2}^y(t)$ are the maximum local speeds in the x and y -directions respectively. To evaluate the flux $H_{i+1/2,j}^x$ and $H_{i,j+1/2}^y$ in Equation. (3.14), eight point-values along the cell walls (as indicated in Figure. 3.4) are required. These values are computed from 2D (piecewise) reconstruction polynomials $P_{ij}^n(x, y) \approx u_{ij}^n(x, y)$, subject to the following conservation constraint:

$$\bar{u}_{ij}^n = \frac{1}{\Delta x \Delta y} \int_{y_{j-1/2}}^{y_{j+1/2}} \int_{x_{i-1/2}}^{x_{i+1/2}} P_{ij}^n(x, y) dx dy, \quad (3.15)$$

where \bar{u}_{ij}^n is the cell-average at time $t = t^n$, $u_{ij}^n(x, y) = u(x, y, t^n)|_{I_{ij}}$. The piecewise polynomial $P_{ij}^n(x, y)$ has the following general form:

$$\begin{aligned}
P_{ij}^n(x, y) = & a_{00} + a_{10}(x - x_i) + a_{01}(y - y_j) + \\
& a_{11}(x - x_i)(y - y_j) + a_{20}(x - x_i)^2 + a_{02}(y - y_j)^2
\end{aligned}$$

where the coefficients a_{kl} are derived from the cell-averages \bar{u}_{ij}^n in such a way that the constraint (3.15) is satisfied, additional details are given in [30].

For the KP scheme, the 2D non-oscillatory third-order accurate reconstruction polynomial is created by the so-called “dimension-by-dimension” approach, which involves a couple of 2D independent reconstructions. For a cell I_{ij} as shown in Figure 3.4, a piecewise polynomial $p_{ij}^n(x, y)$ is constructed for estimating four point-values on the cell edges at east, north, west and south sides; which are shown in Figure. (3.4) as E, N, W and S , respectively. Following this, a second 2D piecewise polynomial $\hat{p}_{ij}^n(x, y)$ is constructed specifically for estimating four corner point-values at NE, NW, SW and SE as shown in Figure. (3.4) with corresponding (i, j) indices.

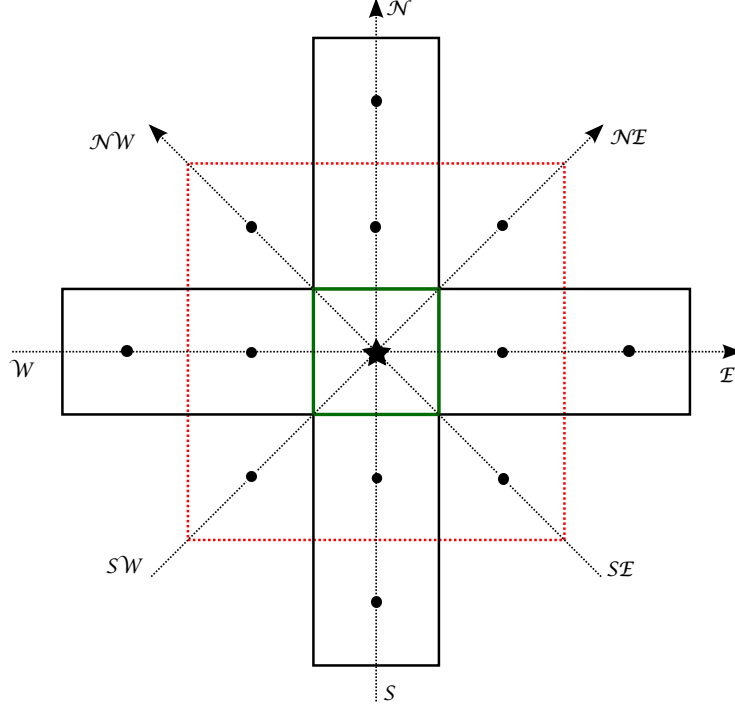


Figure 3.3: 2D stencil for KP, WENO-35 and KL schemes. Thick lines indicate the 2D stencil for WENO-5 scheme. The dashed lines indicate the 2D stencil for WENO-33 scheme.

However, the individual reconstruction polynomials $p_{ij}^n(x, y)$ and $\hat{p}_{ij}^n(x, y)$ satisfy Equation. (3.15) by design, and can be combined as a convex combination to a single polynomial function $R(x, y)$ as follows,

$$R_{ij}(x, y) = (1 - \gamma) p_{ij}^n(x, y) + \gamma \hat{p}_{ij}^n(x, y), \quad (3.16)$$

where γ is the weight function such that $\gamma \in [0, 1]$, and satisfies $\gamma_{i\pm 1/2, j\pm 1/2} = 0$, $\gamma_{i\pm 1/2, j} = \gamma_{i, j\pm 1/2} = 1$. It is clear that $R_{ij}(x, y)$ preserves cell-averages, and the eight point-values required in the flux Equation. (3.14) can be computed as follows (see Figure. (3.4)),

$$u_{ij}^k = R_{ij}^k, \quad k \in \{N, E, W, S, NE, NW, SE, SW\}.$$

Computational stencil required for the reconstruction polynomial $R_{ij}(x, y)$ is shown in Figure. (3.3). In Equation.(3.16), $p_{ij}^n(x, y)$ requires the 1D stencils in W - E and S - N directions,

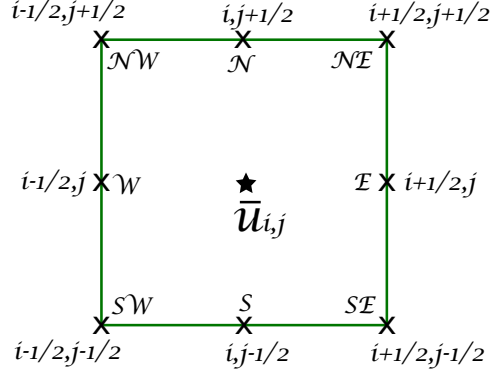


Figure 3.4: Schematic of a 2D control volume, where the fluxes are evaluated on the cell boundaries at eight points ('X' marks). Non-oscillatory reconstruction polynomials are used for the flux evaluation

and $\hat{p}_{ij}^n(x, y)$ requires additional cells along the diagonal $SW-NE$ and $SE-NW$ directions. The flux $H_{i+1/2,j}^x$ in Equation. (3.14) is derived by using the point-wise flux formula (Equation. (3.7)) along the east cell wall (this require values from both sides of the wall), followed by a three-point flux integral using Simpson's rule.

The KP scheme is inherently non-oscillatory, the reconstruction polynomials in Equation. (3.16) is limited in each co-ordinate direction using the limiter used for 1D case. At first, the polynomials are separated into bilinear and biquadratic parts, for example,

$$p_{ij}^n(x, y) = (1 - \theta_{ij}^n) L_{ij}^n(x, y) + \theta_{ij}^n q_{ij}^n(x, y), \quad (3.17)$$

where θ_{ij}^n is the 2D limiter function such that $0 < \theta_{ij}^n < 1$, and the bilinear part

$$L_{ij}^n(x, y) = \bar{u}_{ij}^n + s_{ij}^x(x - x_i) + s_{ij}^y(y - y_j)$$

with directional slopes s_{ij}^x and s_{ij}^y . A *minmod* limiter is applied to make slopes monotonic. The limiter function $\theta_{ij}^n = \min(\theta_i^x, \theta_j^y)$, where θ_i^x and θ_j^y are directional (1D) limiter functions applied as in the 1D case (Equation. (3.8)). A similar procedure is applied to the diagonal reconstruction function $\hat{p}_{ij}^n(x, y)$. Detailed definitions for limiter and quadratic polynomial function can be found in Appendix. (A.1).

3.3 C-FV SCHEMES BASED ON WENO METHODS

The WENO schemes are very robust and widely used for solving conservation laws. A comprehensive review for WENO scheme is given in [64]. The C-FV scheme based on WENO methodology is also known as the CWENO scheme [13]. I consider C-FV schemes based on WENO method. Firstly, a compact third-order fully 2D WENO reconstruction is considered, and the resulting scheme is referred to as WENO-33. The second WENO scheme is based on a fifth-order accurate dimension-splitting 2D scheme, for which a basic 1D reconstruction (fifth-order) is used in each coordinate direction, hereafter this is referred to as WENO-5. I also consider a hybrid scheme which combines both WENO-33 and WENO-5 reconstruction procedure, and referred to as WENO-35.

3.3.1 Third-Order Compact 2D WENO

Levy [13] developed a fully 2D WENO-based central scheme for conservation laws. I adopt the same third-order reconstruction procedure for WENO-33, however, the fluxes are computed at eight point-values on the edges of cell I_{ij} , and the FV stencil is same as the one (Figure. (3.4)) used for the KP scheme. A typical WENO reconstruction process involves a main computational stencil and several sub-stencils within. The basic idea of the WENO method is to use a convex combination of reconstructions from all the stencils, and employ nonlinear weights to gain highest order of accuracy in smooth regions. The stencils which contains non-smooth solution (oscillations) is weighted out by this procedure. For the compact WENO-33, a 3×3 stencil shown in Figure. (3.5) is used, which contains four 2×2 sub-stencils, including the target cell I_{ij} .

The first step is to reconstruct a third-order accurate 2D interpolation polynomial $R_{ij}(x, y)$ on a cell I_{ij} , with a convex combination of four one-sided piecewise linear interpolants p_{NE} , p_{NW} , p_{SW} and p_{SE} , and a centred quadratic interpolant p_C . These polynomials are constructed from the cell averages \bar{u}_{ij} in the computational stencils shown in

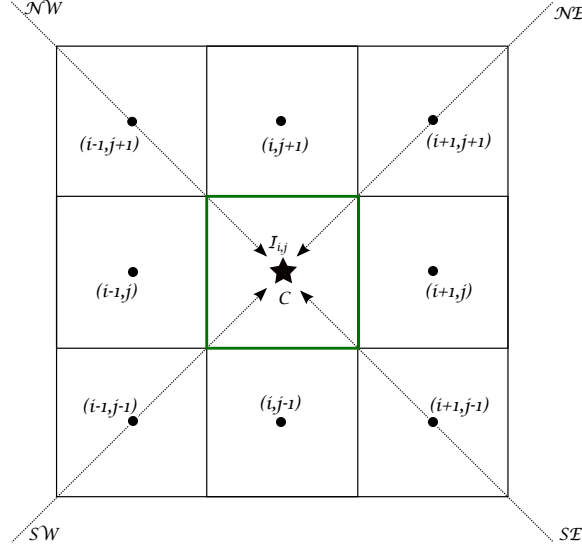


Figure 3.5: The 2D compact stencil for WENO-33 scheme. Reconstruction procedure requires a 3×3 stencil for the quadratic reconstruction, and four sub-stencils employing 2×2 cells for the linear reconstructions.

Figure. (3.5). Thus reconstruction in the cell I_{ij} can be written as:

$$R_{ij}(x, y) = \sum_k w_k^{ij} p_k^{ij}(x, y); \quad k \in \{NE, NW, SE, SW, C\} \quad (3.18)$$

where the weights $w_k^{ij} \geq 0$ and $\sum_k w_k^{ij} = 1$. The weights are computed using the *smoothness indicators* IS_k^{ij} , they detect oscillatory stencils and automatically switch to stencils that cause least oscillatory reconstructions.

The non-linear weights are defined as follows [13] :

$$w_k^{ij} = \frac{\alpha_k^{ij}}{\sum_l \alpha_l^{ij}}, \quad \alpha_k^{ij} = \frac{C_k^{ij}}{(\epsilon + IS_k^{ij})^2}, \quad k, l \in \{NE, NW, SE, SW, C\}.$$

where $\epsilon = 1.1 \times 10^{-12}$, and values for C_{NE} , C_{NW} , C_{SE} and C_{SW} are set to $1/8$, and $C_C = 1/2$. The smoothness indicators are defined as

$$IS_k = h^2[(u'_{ij})^2 + (u''_{ij})^2]; \quad k \in \{NE, NW, SE, SW, C\}$$

and smoothness indicator for centre reconstruction with $\Delta x = \Delta y = h$ is defined to be,

$$IS_c = h^2[(u'_{ij})^2 + (u^\wedge_{ij})^2] + \frac{h^4}{3}[13(u''_{ij})^2 + 14(u^\wedge_{ij})^2 + 13(u^\nabla_{ij})^2],$$

where

$$\begin{aligned} u'_{ij} &= \frac{\bar{u}_{i+1,j}^n - \bar{u}_{i-1,j}^n}{2\Delta x}, & u^\wedge_{ij} &= \frac{\bar{u}_{i,j+1}^n - \bar{u}_{i,j-1}^n}{2\Delta y}, \\ u''_{ij} &= \frac{\bar{u}_{i+1,j}^n - 2\bar{u}_{ij}^n + \bar{u}_{i-1,j}^n}{\Delta x^2}, & u^\nabla_{ij} &= \frac{\bar{u}_{i,j+1}^n - 2\bar{u}_{ij}^n + \bar{u}_{i,j-1}^n}{\Delta y^2}, \\ u^\wedge_{ij} &= \frac{\bar{u}_{i+1,j+1}^n + \bar{u}_{i-1,j-1}^n - \bar{u}_{i+1,j-1}^n - \bar{u}_{i-1,j+1}^n}{4\Delta x\Delta y}. \end{aligned}$$

The four one-sided linear reconstructions required in Equation. (3.18) are given as below,

$$\begin{aligned} p_{NE}(x, y) &= \bar{u}_{ij}^n + \frac{\bar{u}_{i+1,j}^n - \bar{u}_{ij}^n}{\Delta x}(x - x_i) + \frac{\bar{u}_{i,j+1}^n - \bar{u}_{ij}^n}{\Delta y}(y - y_j), \\ p_{NW}(x, y) &= \bar{u}_{ij}^n + \frac{\bar{u}_{ij}^n - \bar{u}_{i-1,j}^n}{\Delta x}(x - x_i) + \frac{\bar{u}_{i,j+1}^n - \bar{u}_{ij}^n}{\Delta y}(y - y_j), \\ p_{SW}(x, y) &= \bar{u}_{ij}^n + \frac{\bar{u}_{ij}^n - \bar{u}_{i-1,j}^n}{\Delta x}(x - x_i) + \frac{\bar{u}_{ij}^n - \bar{u}_{i,j-1}^n}{\Delta y}(y - y_j), \\ p_{SE}(x, y) &= \bar{u}_{ij}^n + \frac{\bar{u}_{i+1,j}^n - \bar{u}_{ij}^n}{\Delta x}(x - x_i) + \frac{\bar{u}_{ij}^n - \bar{u}_{i,j-1}^n}{\Delta y}(y - y_j), \end{aligned}$$

The central quadratic polynomial is defined as:

$$\begin{aligned} p_C(x, y) &= \hat{u}_{ij}^n + u'_{ij}(x - x_i) + u^\wedge_{ij}(y - y_j) + 2u^\nabla_{ij}(x - x_i)(y - y_j) \\ &\quad + u''_{ij}(x - x_i)^2 + u^\nabla_{ij}(y - y_j)^2, \end{aligned}$$

where

$$\hat{u}_{ij}^n = \bar{u}_{ij}^n - \frac{1}{12} [(\Delta x^2 u''_{ij}) + (\Delta y^2 u^\nabla_{ij})].$$

Note that the reconstruction polynomial, $R_{ij}(x, y)$ in Equation. (3.18), which is a convex combination of conservative linear and quadratic reconstruction polynomials, preserves the cell-averages. $R_{ij}(x, y)$ can be used for estimating fluxes at the eight point-values, similar to the KP scheme. Thus the final form for the semi-discrete WENO-33 scheme is same as Equation. (3.13), with fluxes given in Equation. (3.14).

3.3.2 Fifth-Order WENO Scheme (WENO-5)

The fifth-order WENO (or WENO-5) scheme is one of the most widely used scheme for various applications including atmospheric modeling [56, 55]. Recently, Byron et al. [4] applied a 1D central WENO-5 scheme for a system of conservation laws. One can rigorously derive fifth-order accurate fully 2D WENO scheme, the computational stencil in this case will be 5×5 , and the resulting scheme may be very expensive. However, I consider a dimension-split 2D scheme, which employs the basic 1D fifth-order WENO scheme in each coordinate direction. Computational stencil for the 1D scheme is 5 cell-wide, as depicted in Figure. (3.2). In Figure. (3.3), the 2D stencil (thick solid lines) for the WENO-5 is schematically shown in $W-E$ and $S-N$ directions. Flux evaluation for the split-scheme is required only at four cell walls, making the computational procedure relatively simple.

The reconstruction function $R(x_{i+1/2})$ at cell interface $x_{i+1/2}$, can be written in the following way:

$$R_{i+1/2} = \sum_{k=0}^{r-1} w_k p_{i+1/2}^k \quad (3.19)$$

where $r = 3$, and

$$p_{i+1/2}^k = \sum_{m=0}^{r-1} c_{km} \bar{u}_{i-k+m}, \quad k = 0, \dots, r-1,$$

values of constants c_{km} , are given in 3.1 [38]. The nonlinear weight are given as

$$w_k = \frac{\alpha_k}{\sum_{s=0}^{r-1} \alpha_s}, \quad \alpha_k = \frac{C_k}{(\epsilon + IS_k)^2}, \quad k = 0, \dots, r-1$$

where $C_0 = 3/10, C_1 = 3/5, C_2 = 1/10$, and the smooth indicators IS_k are defined by:

$$\begin{aligned} IS_0 &= \frac{13}{12}(\bar{u}_i - 2\bar{u}_{i+1} + \bar{u}_{i+2})^2 + \frac{1}{4}(3\bar{u}_i - 4\bar{u}_{i+1} + \bar{u}_{i+2})^2, \\ IS_1 &= \frac{13}{12}(\bar{u}_{i-1} - 2\bar{u}_i + \bar{u}_{i+1})^2 + \frac{1}{4}(\bar{u}_{i-1} - \bar{u}_{i+1})^2 \\ IS_2 &= \frac{13}{12}(\bar{u}_{i-2} - 2\bar{u}_{i-1} + \bar{u}_i)^2 + \frac{1}{4}(\bar{u}_{i-2} - 4\bar{u}_{i-1} + 3\bar{u}_i)^2 \end{aligned}$$

Table 3.1: Values of constants c_{km}

k	m=0	m=1	m=2
-1	11/6	- 7/6	1/3
0	1/3	5/6	-1/6
1	-1/6	5/6	1/3
2	1/3	-7/6	11/6

The 2D scheme can be obtained directly by extending the same framework used for the 1D case. This is a dimension-by-dimension approach in x - and y -directions. The reconstruction details of 2d WENO-5 scheme are given in Appendix. (A.2).

The fluxes are evaluated using the following simple form, which is a special case of Equation. (3.14).

$$\begin{aligned}
H^x_{i+1/2,j}(t) &= \frac{F(u^+_{i+1/2,j}(t)) + F(u^-_{i+1/2,j}(t))}{2} - \frac{a^x_{i+1/2,j}(t)}{2} \left[u^+_{i+1/2,j}(t) - u^-_{i+1/2,j}(t) \right], \\
H^y_{i,j+1/2}(t) &= \frac{G(u^+_{i,j+1/2}(t)) + G(u^-_{i,j+1/2}(t))}{2} - \frac{a^y_{i,j+1/2}(t)}{2} \left[u^+_{i,j+1/2}(t) - u^-_{i,j+1/2}(t) \right].
\end{aligned} \tag{3.20}$$

3.3.3 A Hybrid Central WENO Scheme (WENO-35)

Finally, I combine WENO-33 and WENO-5 reconstruction procedures to form the central WENO-35, which is at least third-order accurate. The hybrid scheme requires eight point-value evaluation for the flux and utilizes the full computational stencil used for the KP scheme (Figure. (3.3)). the combination of the schemes is done in the following way: the point values of the reconstruction functions on the edges are calculated using the WENO-5 scheme, and the values on the corners are obtained by using compact WENO-33 reconstructions. Final semi-discretized form, given by Equation. (3.13), for which the flux is evaluated using Equation. (3.14).

3.4 A FOURTH ORDER KURGANOV LIU SCHEME (KL)

Finally, I consider a fourth order semi-discrete central-upwind FV method developed by Kurganov et al. [28]. This method is based on Godunov type methods which are very simple and computationally inexpensive. The KL method is based on unlimited high-order piecewise polynomial reconstruction. In this scheme the stability is enforced by adding a new adaptive artificial viscosity, whose coefficients are proportional to the size of the weak local residual and whose values are sufficiently large at the shock regions, much smaller in the smooth parts of the computed solution. Therefore, there is no need for computationally expensive non-linear limiters. These reconstruction polynomials optionally use positivity preserving filters. The reconstruction functions and other details are given in [28]. The KL scheme requires eight point-value evaluation for the flux; which are shown in Figure. (3.3) as E, N, W, S, NE, NW, SE , and SW . The computational stencil utilized by KL scheme is shown in Figure. (3.3).

The reconstructed point values at eight points on a single cell (i.e. $E, W, N, S, SE, SW, NE, NW$) can be obtained by the following:

$$\begin{aligned}
u_{ij}^E &= C_1 + C_2 + C_4 + C_9 + C_{12}, & u_{ij}^W &= C_1 - C_2 + C_4 - C_9 + C_{12}, \\
u_{ij}^S &= C_1 + C_3 + C_5 + C_{10} + C_{13}, & u_{ij}^N &= C_1 - C_3 + C_5 - C_{10} + C_{13}, \\
u_{ij}^{NE} &= u_{ij}^E + C_3 + C_5 + C_6 + C_7 + C_8 + C_{10} + C_{11} + C_{13}, \\
u_{ij}^{SE} &= u_{ij}^E - C_3 + C_5 - C_6 - C_7 + C_8 - C_{10} + C_{11} + C_{13}, \\
u_{ij}^{NW} &= u_{ij}^W + C_3 + C_5 - C_6 + C_7 - C_8 + C_{10} + C_{11} + C_{13}, \\
u_{ij}^{NE} &= u_{ij}^W - C_3 + C_5 + C_6 + C_7 - C_8 - C_{10} + C_{11} + C_{13}.
\end{aligned} \tag{3.21}$$

the details of the auxillary quantities $C'S$ are given in Appendix. (A.3).

3.5 FILTERS AND BOUND PRESERVATION

The WENO schemes can remove spurious oscillations, nevertheless, there is no guarantee that it will always keep the numerical solution within the legitimate (physical) bounds.

The numerical solution may still have small amplitude oscillations even after the application of limiter. In other words, these schemes are only “essentially” non-oscillatory not strictly positivity preserving. Another issue is that the final semi-discrete FV formula itself may be a source for spurious negative numbers. On the right-side of Equation. (3.13), time tendencies are computed as differences of fluxes through the cell walls. When the values of the fluxes are very close, the net result may have a negative sign (with very small magnitude) because of the numerical precision errors. For many atmospheric tracers such as humidity and mixing ratios, the global maximum and minimum values are known in advance, and they have “zero tolerance” for negative values. To address this issue, I implement an optional positivity-preserving filters to the C-FV schemes.

First, I discuss a bound-preserving (BP) conservative filter, which is particularly useful when the global minimum and maximum value of the solution is known in advance. In the present work, I implemented the BP filter for the WENO-based and KL schemes. The BP filter relies on local reconstruction polynomial, and it is computationally inexpensive. The BP filter is based on limiter given in [39]. Recently, Zhang et. al. [77] extended this for high-order discontinuous Galerkin (DG) schemes, Nair et. al. [78] implemented BP filter for a DG transport scheme on the cubed-sphere.

Let $p_{ij}(x, y)$ be a reconstruction polynomial on a cell I_{ij} with known cell average \bar{u}_{ij} . The BP filter replaces $p_{ij}(x, y)$ by a bound preserving reconstruction $\tilde{p}_{ij}(x, y)$ as follows:

$$\tilde{p}_{ij}(x, y) = \theta_{ij} p_{ij}(x, y) + (1 - \theta_{ij}) \bar{u}_{ij}, \quad (3.22)$$

the limiter function $\theta_{ij} \in [0, 1]$, is defined as:

$$\theta_{ij} = \min \left\{ \left| \frac{M - \bar{u}_{ij}}{M_{ij} - \bar{u}_{ij}} \right|, \left| \frac{m - \bar{u}_{ij}}{m_{ij} - \bar{u}_{ij}} \right|, 1 \right\}, \quad (3.23)$$

where M and m are the global maximum and minimum values of the initial condition. The local extrema M_{ij} , m_{ij} are given by:

$$M_{ij} = \max_{(x,y) \in I_{ij}} \{p_{ij}(x, y)\}, \quad m_{ij} = \min_{(x,y) \in I_{ij}} \{p_{ij}(x, y)\}.$$

$\tilde{p}_{ij}(x, y)$ can be used for computing fluxes.

A scheme is considered to be positive-definite, if it does not introduce any negative values in the computed solution from non-negative initial values. However, due to arithmetic precision errors as mentioned above, the solutions with very small magnitude might still have negative signs. A positivity (or sign) preserving (PP) filter may be applied at the final stage of computation to completely eliminate unacceptable negative solution.

To ensure the positivity of the solution, I employ the PP filter based on an upstream re-normalization approach developed by Smalarkiewicz [65]. This filter is local, computationally cheap and easy to implement. Recently, Blossey et. al. [3] implemented PP filter for their FV schemes. The details of the PP algorithm can be found in [65].

3.6 TIME INTEGRATION SCHEMES

After the spatial discretization with FV schemes, the continuous equation (3.12) reduces to a semi-discretized ODE (3.13), which can be represented in the following general form:

$$\frac{d}{dt}\bar{u}(t) = L(\bar{u}) \quad \text{in } (0, T]. \quad (3.24)$$

There are a wide variety of time integrators available to solve the ODE (3.24), however, I only consider the explicit Runge-Kutta (RK) time integration methods.

3.6.1 SSP-RK3 scheme

In this present work, I use a strong stability preserving (SSP) third-order and three-stage RK (SSP-RK3) time integration [17] for the KP and WENO-33 schemes. The SSP time integration schemes are widely used in DG literature [9], these schemes do not generate new local maxima or minima (or total variation diminishing property in time) due to the

time discretization. The SSP-RK3 scheme can be written as follows,

$$\begin{aligned}\bar{u}^{(1)} &= [\bar{u}^n + \Delta t L(\bar{u}^n)], \\ \bar{u}^{(2)} &= \frac{3}{4}\bar{u}^n + \frac{1}{4} [\bar{u}^{(1)} + \Delta t L(\bar{u}^{(1)})], \\ \bar{u}^{n+1} &= \frac{1}{3}\bar{u}^n + \frac{2}{3} [\bar{u}^{(2)} + \Delta t L(\bar{u}^{(2)})].\end{aligned}$$

Here the superscripts n and $n + 1$ denotes the time level t and $t + \Delta t$ respectively. The CFL limit for KP scheme with SSP-RK3 for the linear transport problem is approximately 1.0.

3.6.2 SSP-RK (5,4) Scheme

A new class of optimal high-order SSP and low-storage SSP RK schemes with stage (s) > order (p), have been proposed by Spiteri et. al. [66]. These schemes are more efficient than the known schemes with $s = p$, due to the increase in the allowable timestep which more than compensates the added computational cost per step. Moreover it is recommended to keep the order of the scheme and time integration scheme consistent. In the present work, I used 5-stage 4th-order SSP-RK scheme (or SSP-RK (5,4)) for the WENO-35, K1, and WENO-5 schemes. Note that the allowable time-step for this scheme is greater than that of the Shu-Osher fourth-order scheme and fourth-order explicit RK scheme. The CFL limit for this scheme is approximately 1.5. The SSP-RK (5,4) scheme can be written in the following way:

$$\begin{aligned}\bar{u}^{(0)} &= \bar{u}^n, \\ \bar{u}^{(i)} &= \sum_{k=0}^{(i-1)} [\alpha_{ik}\bar{u}^k + \Delta t\beta_{ik}L(\bar{u}^k)], \quad i = 1, 2, \dots, s \\ \bar{u}^{n+1} &= \bar{u}^{(s)}.\end{aligned}$$

Here the superscripts n and $n + 1$ denotes the time level t and $t + \Delta t$ respectively.

Constants α_{ik} and β_{ik} are given in Appendix. (A.4).

3.7 DISCUSSION AND SUMMARY

This chapter presents the first problem considered, i.e. the transport (advection) problem to be solved using the numerical methods which are also explained in detail here. The discretization of the transport problem in 1D and 2D is given. The methodology for evaluating flux and the reconstruction details of individual scheme is mentioned in this chapter. The flux evaluation utilizes the upwind flavor i.e. the one sided local speeds to get rid of the staggering present in the central schemes. I employ a third-order SSP-RK3 time integration scheme for KP and WENO-33 schemes, since these schemes are third-order, and for the rest, I used a fourth-order five-stage SSP-RK(5,4) time integration scheme. These two time integration schemes are also explained in detail here. Despite the presence of smoothness and weight factors present in WENO type and KL schemes, there are spurious oscillations and negative values observed in the solution, to address this issue, I utilized two filters, bound preserving and positivity filters, which are also explained in this chapter.

Chapter 4

2D Numerical Experiments

Three benchmark tests are employed to validate the proposed schemes on a 2D Cartesian domain, by solving the transport equation (3.12), where the scalar field being advected is $\phi(x, y, t)$. The initial conditions and numerical results of test cases on a 2D Cartesian plane are given in this chapter. The normalized errors are calculated in the height field making use of the global error norms, and can be given as:

$$\begin{aligned}\ell_1(h) &= \frac{I[|h - h_t|]}{I[|h_t|]}, \\ \ell_2(h) &= \sqrt{\frac{I[(h - h_t)^2]}{I[h_t^2]}}, \\ \ell_\infty(h) &= \frac{\max[|h - h_t|]}{\max[|h_t|]},\end{aligned}\tag{4.1}$$

where h_t is the true (initial) height field and I denotes an approximation to the global integral, and is given by:

$$I[x] = \sum_n x_n A_n\tag{4.2}$$

Here n is the total number of cells and A_n is the area of the cell n .

Table 4.1: L_2 norms for 2D solid body rotation of a Gaussian hill.

N	KP	WENO-33	WENO-5	WENO-35	KL
16	0.3652	0.3493	0.2438	0.2820	0.1242
32	0.0914	0.0801	0.0246	0.0436	0.0119
64	0.0216	0.0114	0.0015	0.0045	0.0006
128	0.0066	0.0013	0.00005	0.0004	0.00006

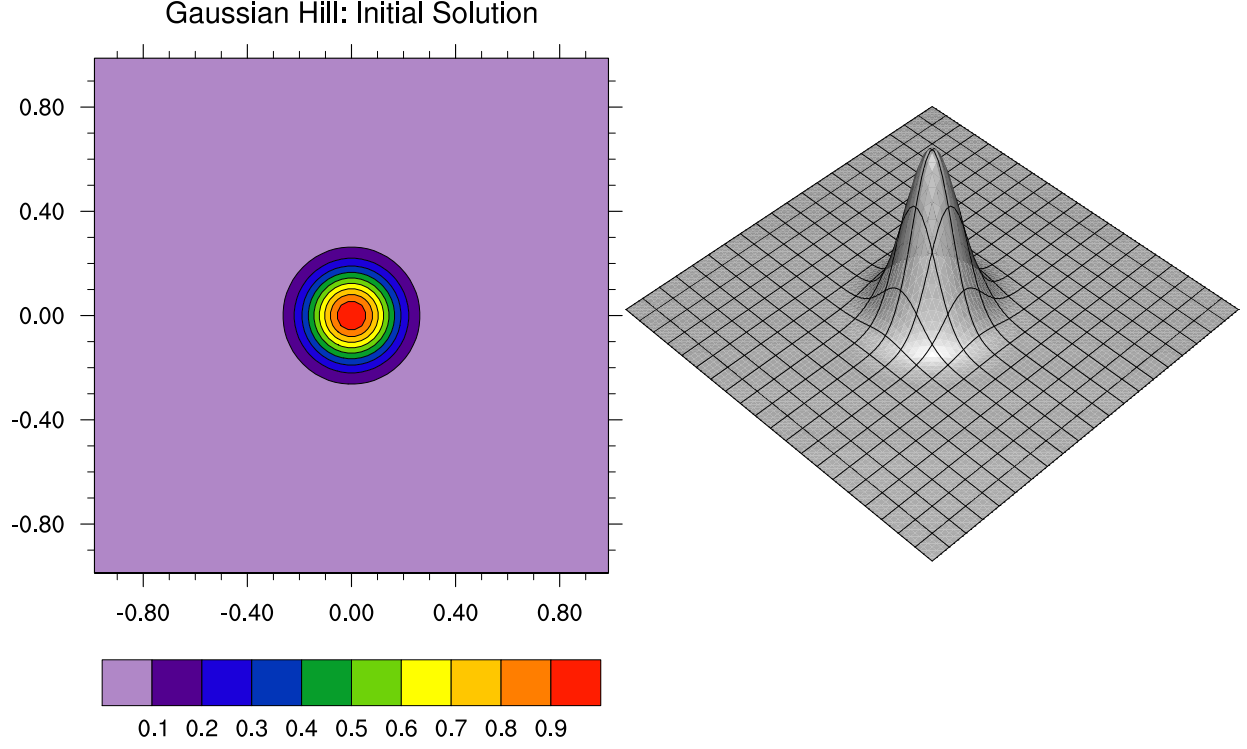


Figure 4.1: Initial solution for test case, solid body rotation of smooth function. A gaussian hill is placed at the center of the 2D Cartesian plane.

4.1 SOLID-BODY ROTATION OF A SMOOTH FUNCTION

The first test considered is a solid-body rotation of a smooth function, i.e. Gaussian hill ϕ , defined on a periodic domain $\Omega = [-1, 1] \times [-1, 1]$. This test is used to study the convergence properties of the numerical schemes. The initial condition is defined as:

$$\phi(x, y, t = 0) = a_0 \exp\{-b_0[(x - x_0)^2 + (y - y_0)^2]\},$$

where $a_0 = 1$ and $b_0 = 81/3$, $x_0 = 0$ and $y_0 = 0$. The velocity field is given by $\mathbf{v} = (-\omega y, \omega x)$ with a constant angular velocity ($\omega = 1$). The analytic solution to this problem is known at any time. The initial solution can be depicted from the Figure. (4.1), a Gaussian hill is placed at the center of the 2D Cartesian plane and is rotated around its own axis.

I evaluated the different schemes: KP, WENO-33, WENO-5, WENO-35 and KL at

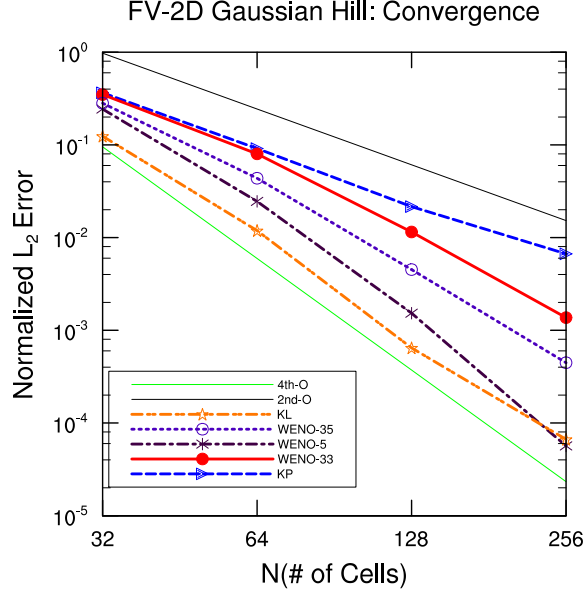


Figure 4.2: Convergence plot for 2D Cartesian solid-body (Gaussian hill) after one full revolution. All the five schemes KP, WENO-33, WENO-5, WENO-35 and KL are used for the convergence plots. Here CFL (0.50) is kept constant for different number of cells.

various resolutions increasing from 16×16 to 128×128 for the Gaussian hill test case. The CFL number of 0.50 is used for this experiment. The convergence of normalized ℓ_2 errors, for each scheme, is shown in Figure. (4.2) and the normalized ℓ_2 errors are given in Table 4.1. In this case both the filters (BP and PP) are used for WENO-33, WENO-5, WENO-35 and KL schemes. It is clear from the results that the order of accuracy is not degraded while using the WENO schemes as opposed to the KP scheme.

The WENO-5 and KL schemes produce almost similar kind of results and they produce more accurate results than KP, WENO-35 and WENO-33 schemes. The order of accuracy in increasing manner of the schemes, can be stated as $KP < WENO-33 < WENO-35 < WENO-5 \cong KL$.

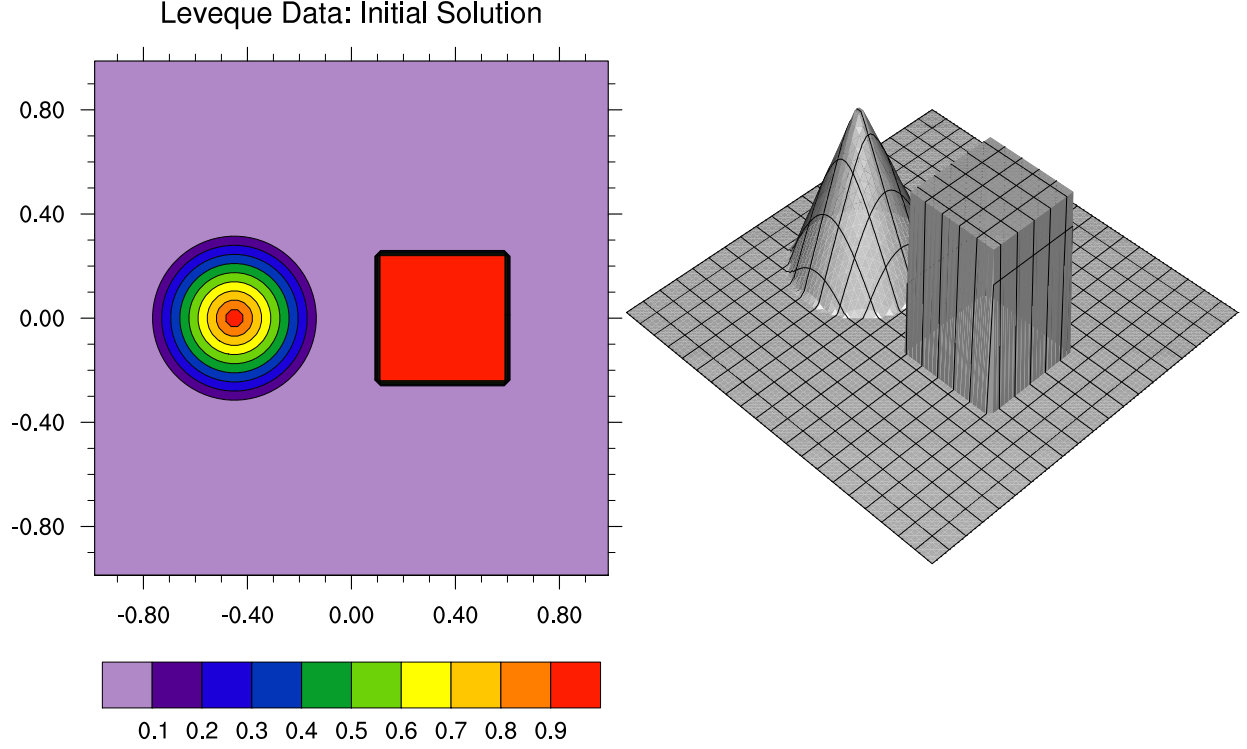


Figure 4.3: Initial solution for test case: solid body rotation of non-smooth function. The initial data consists of a cosine cone and a square block, and they rotate around the center of axis of 2D Cartesian plane.

4.2 SOLID-BODY ROTATION OF A NON-SMOOTH FUNCTION

The second test is again a solid-body rotation test but with a non-smooth function (i.e. Leveque data) given in [36]. The non-smooth initial data comprise a circular cone and a square-block. The initial data is given in Figure. 4.3. This test analyses the monotonicity behaviour of the scheme due to the presence of quasi-continuous data. The initial data ϕ is defined by:

$$\phi(x, y, 0) = \begin{cases} 1 & \text{if } \max(|x - 0.35|, |y - 0|) \leq 0.25, \\ 1 - \frac{r}{0.35} & \text{if } r = \sqrt{(x + 0.4)^2 + y^2} < 0.35, \\ 0 & \text{otherwise.} \end{cases}$$

The velocity field and the domain is the same as that used for the Gaussian hill test.

I would like to give some emphasis on the limiter used for limiting the solution. So, I chose KP scheme to do the analysis and the results are given in the Figure. 4.4. In this figure, the solution after one revolution is shown, here I use a resolution of 40×40 , and a time step is chosen such that CFL limit is 0.50, a limiter is not used to limit the solution, it can be clearly see from the Figure. (4.4), the overshoots and undershoots at the edges of the square block, this is termed as Gibbs phenomenon.

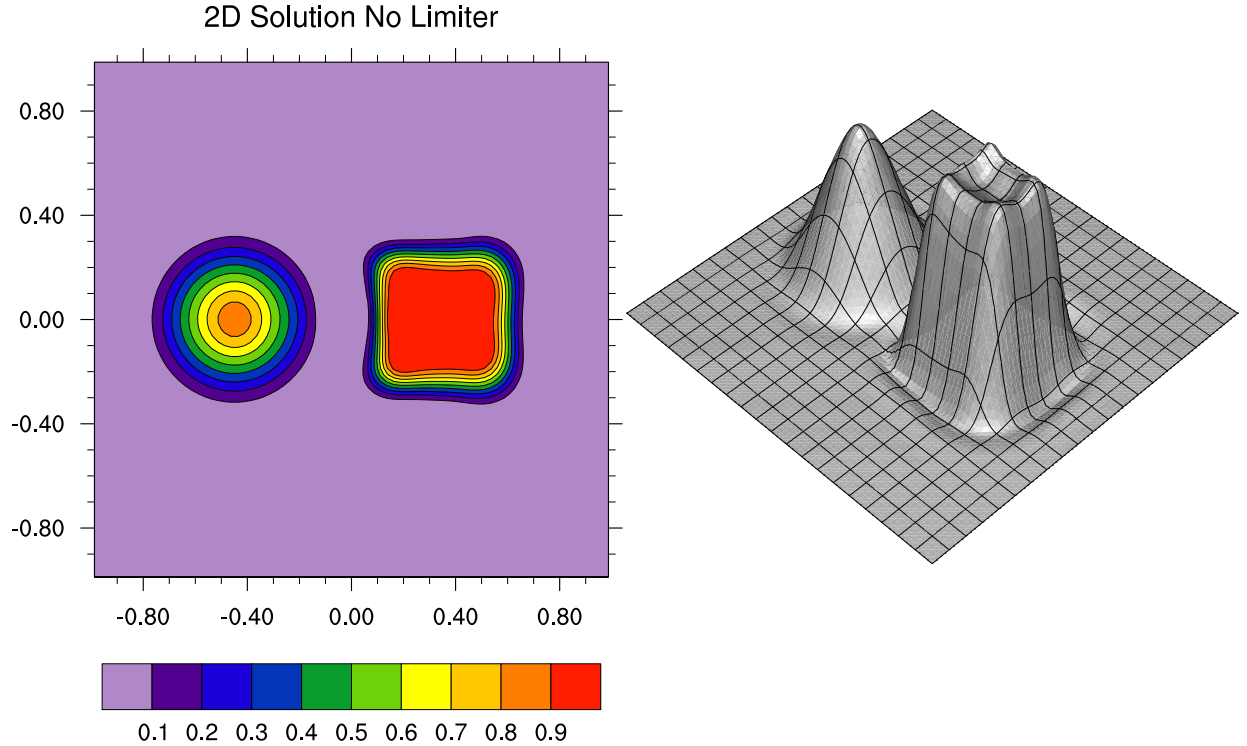


Figure 4.4: The solution after one revolution of Leveque data using KP scheme without limiter, a resolution of 40×40 , and CFL limit of 0.50 is used here. The aim of this figure is to illuminate the Gibbs phenomenon i.e. the spurious oscillations at the top and bottom of the square block, that are introduced into the solution if no limiter is used.

In Figure. (4.5), the results of the solid body rotation of Leveque data is given, obtained by KP scheme with a limiter. From the results it is clear that the Gibbs phenomenon showed

in Figure. 4.4, are deleted. The solution attained is smooth and is free from the spurious oscillations, this shows that the effectiveness of the limiter.

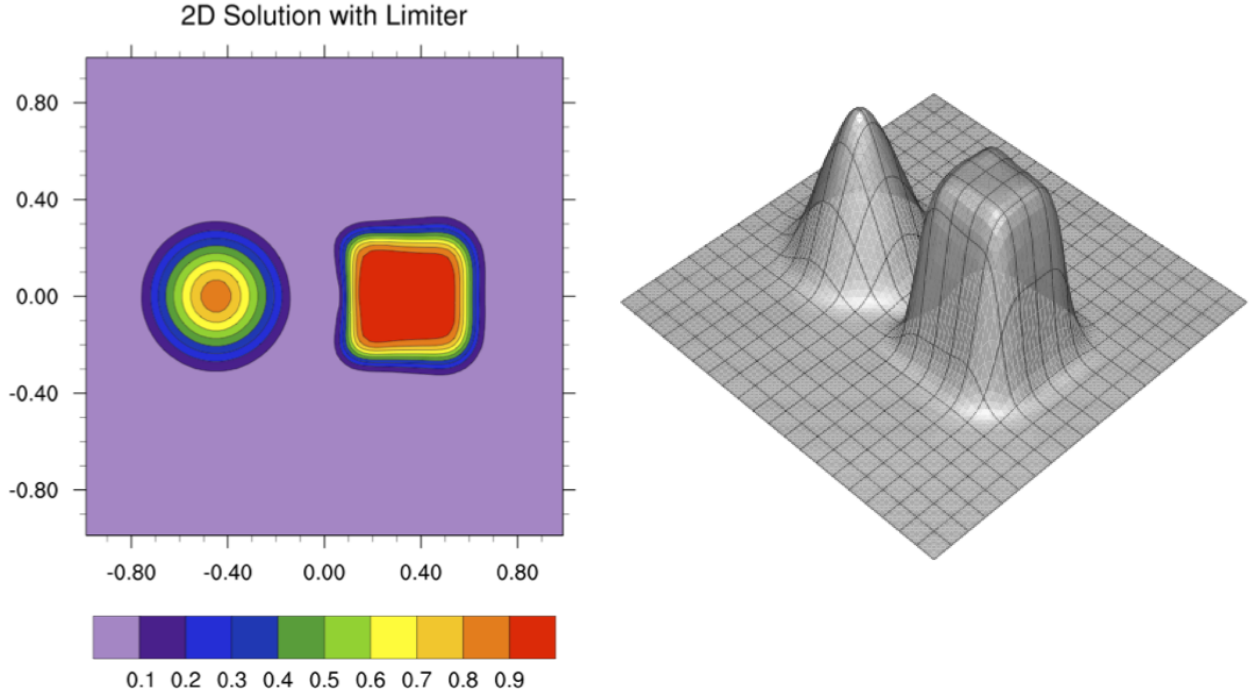


Figure 4.5: All the details are same as in Figure. 4.4, but a limiter is used in KP scheme to attain the solution. It can be clearly seen that the spurious oscillations are smoothened by the use of a limiter.

The results for the solid-body rotation of non-smooth initial data are given in Figure. (4.6) for all the C-FV schemes considered. The contour plots of the numerical results after one revolution and exact (reference) solution are given. The grid resolution used to generate the simulation is 80×80 , and the time step is chosen such that CFL number is set to 0.50. In this test case both filters (BP and PP) are employed for the WENO and KL schemes. From the results, I notice that the WENO and KL schemes with filters remove spurious oscillations, they are positive-definite and able to preserve the shape of the initial data. However, even with a built-in limiter, the KP scheme produces spurious oscillations, as seen in Figure. (4.6). In general, the KL scheme preserves the shape of the solution better

Initial and Final Fields: Solid-Body Rotation Test

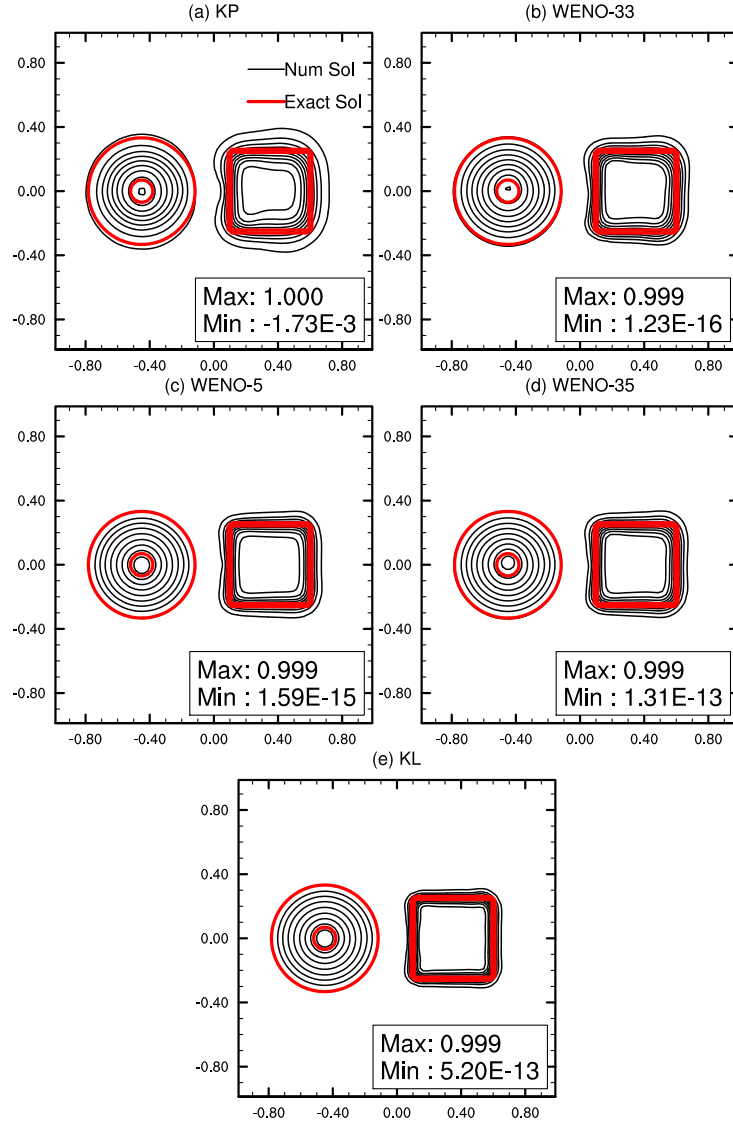


Figure 4.6: Numerical results of solid-body rotation of non-smooth function [36], after one revolution with $\text{CFL} = 0.50$ and $\Delta x = \Delta y = .025$ on a domain $\Omega = [-1, 1]^2$, using (a) KP scheme, (b) WENO-33 scheme, (c) WENO-5 scheme, (d) WENO-35 scheme (e) KL scheme. The numerical solution is represented by the solid lines in which the contour values are from 0.05 to 0.95 with increment of 0.1. Thick solid-lines represent the exact reference solution with a contour value of 0.05 and 0.75.

than all the other schemes and the WENO schemes achieve a substantial improvement in the quality of the numerical solution compared to the KP scheme.

4.3 DEFORMATIONAL FLOW TEST

The third test I considered is a deformational flow test given in [3]. This test is a very challenging test-case due to the time-varying swirling flow that deforms an initially well resolved circular patch. The initial data ϕ is given by:

$$\phi(x, y, t = 0) = \begin{cases} \phi_0 + (\frac{1+\cos(\pi\tilde{r})}{2})^2 & \text{if } \tilde{r} \leq 1 \\ \phi_0 & \text{if } \tilde{r} > 1, \end{cases}$$

where $\tilde{r} = 5\sqrt{(x - 0.3)^2 + (y - 0.5)^2}$. The background scalar concentration is $\phi_0 = 0$. The velocity field on the domain($\Omega = [0, 1] \times [0, 1]$) is given by

$$u_d(x, y, t) = u_\theta(r, t) \sin \theta_d, \quad v_d(x, y, t) = -u_\theta(r, t) \cos \theta_d$$

where

$$\begin{aligned} r &= \sqrt{(x - 0.5)^2 + (y - 0.5)^2}, \\ \theta_d &= \tan^{-1} \left(\frac{y - 0.5}{x - 0.5} \right), \\ u_\theta(r, t) &= \frac{4\pi r}{T} \left[1 - \cos \left(\frac{2\pi t}{T} \right) \frac{1 - (4r)^6}{1 + (4r)^6} \right], \end{aligned}$$

and the final time $T = 5$ units.

This test is performed on a square domain $[0, 1]^2$, with a mesh resolution of 100×100 , which gives $\Delta x = \Delta y = 0.01$. A CFL maximum of 0.50 is chosen. The evolution of the circular patch at different time $t = 0 (T)$, $T/4$, $T/2$ and $t = 3T/4$; is shown in [3]. Contours of the numerical solution after one (full) evolution ($t = T$), and the exact solution (initial field) with different schemes are shown in Figure. (4.8). The maximum and minimum values at final time are also shown in the figure. All the simulations are performed under uniform conditions. In Figure. (4.7), the evolution of the circular patch at time $T/4$, $T/2$, and $3T/4$ is presented.

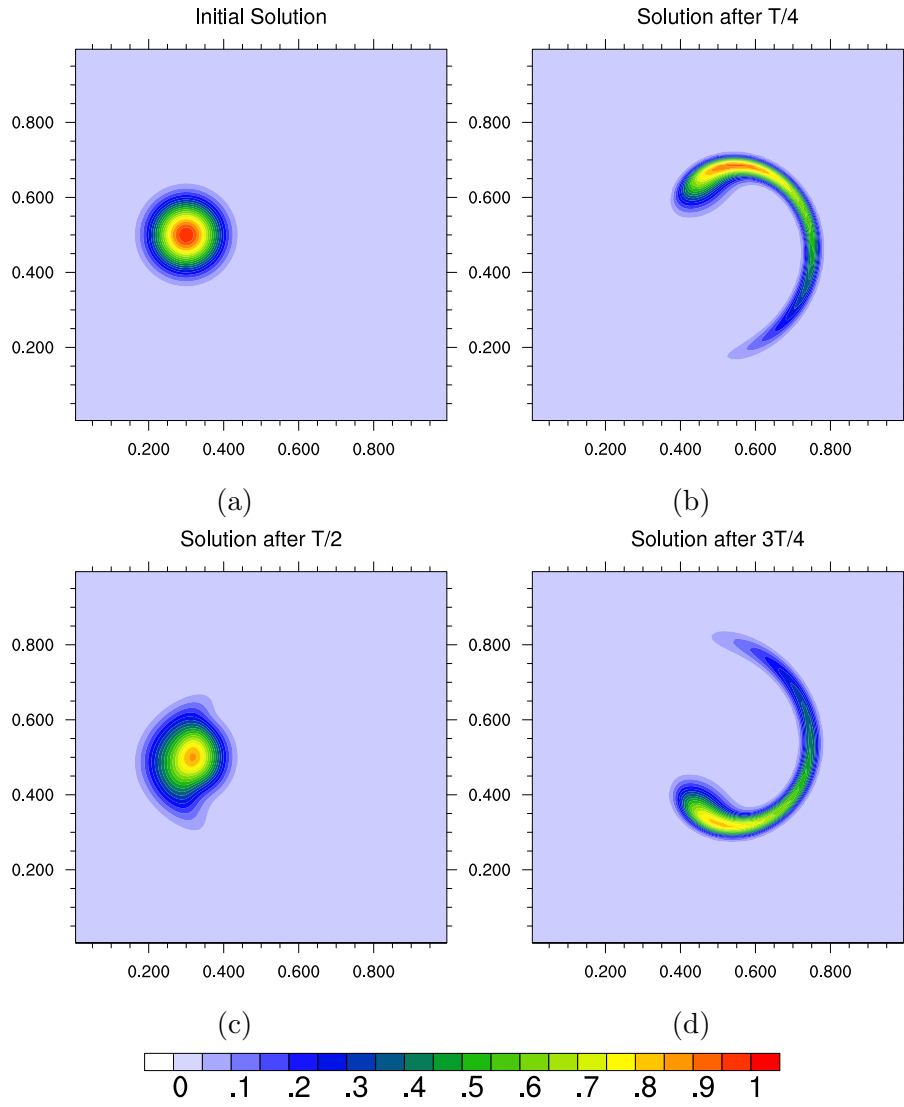


Figure 4.7: Numerical results of Deformational flow test mentioned in test case 3 with CFL=0.50, $\Delta x = \Delta y = .01$ on a 2D Cartesian domain, $\Omega = [0, 1]^2$ using WENO-35 scheme. The figure (a) shows the initial solution, and the panels (b), (c) and (d) show the deformation of the initial solution at $T/4$, $T/2$, and $3T/4$ respectively.

Initial and Final Fields: Deformational Flow Test

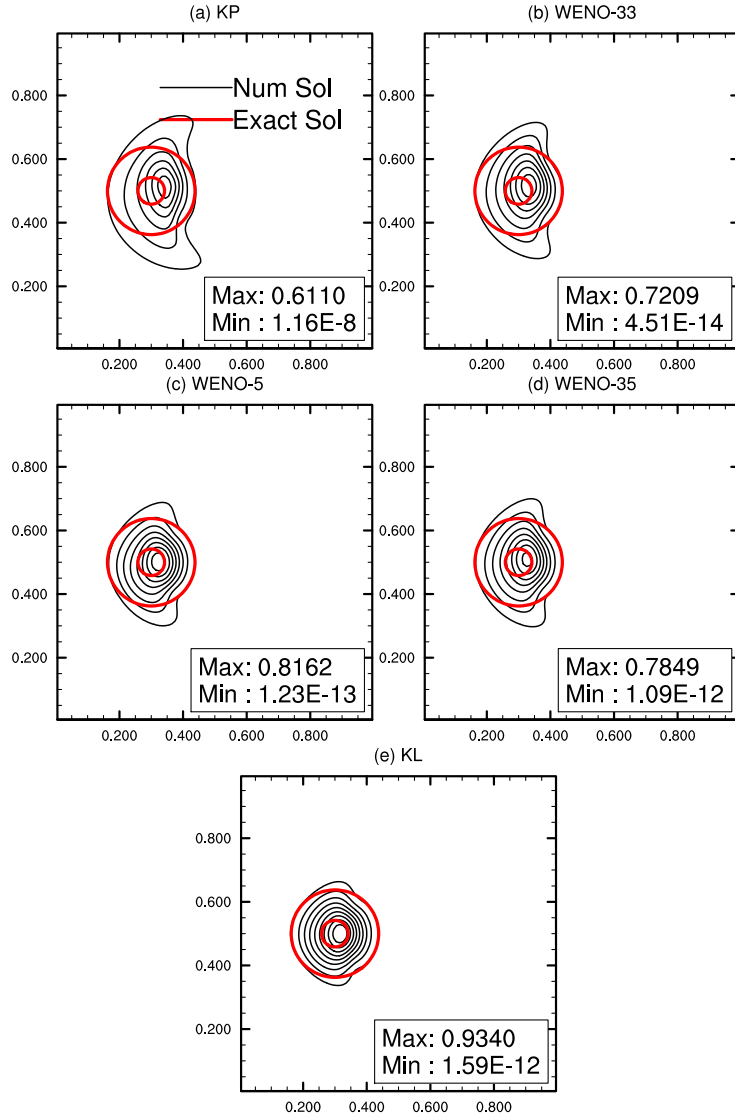


Figure 4.8: Numerical results of deformational flow test at the final time T , with $CFL=0.50$, $\Delta x = \Delta y = .01$ on domain $\Omega = [0, 1]^2$, using different schemes (a) KP, (b) WENO-33, (c) WENO-5, (d) WENO-35 and (e) KL schemes. The numerical solution is represented by the solid lines in which the contour values are from 0.05 to 0.95 with increment of 0.1. Thick solid-lines represent the exact reference solution with a contour value of 0.05 and 0.75.

From the results it is clear that the KL scheme preserves the shape of the initial data better than all the other schemes, WENO schemes preserve the shape of the initial data, and achieving a substantial improvement in the quality of the numerical solution, as opposed to a KP scheme. Moreover, the WENO-5 scheme produces better numerical solution than all the other schemes except KL scheme. WENO-35 scheme falls in between WENO-33 and WENO-5 schemes.

4.4 DISCUSSION AND SUMMARY

The five schemes considered are developed on a 2D cartesian plane to solve the transport (advection) problem. The performance and accuracy of the schemes is analysed using solid body rotation and deformational flow tests. Solid body rotation of a smooth function (Gaussian hill) along the center is utilized to study the convergence properties of the numerical schemes. From the results, it is clear that the order of convergence of all the schemes fall between second- and fourth-order. WENO type and KL schemes perform better than KP in terms of accuracy. The order of accuracy in increasing manner of the schemes, can be stated as $KP < WENO-33 < WENO-35 < WENO-5 \cong KL$. The second test is the rotation of non-smooth function, i.e. Leveque data. KL scheme preserves the shape of the initial solution better than all the other schemes, WENO-5 produces almost similar results. The third test is more challenging, a well resolved circular patch is evolved in time and after one revolution, the exact solution is the initial solution. KL scheme preserves the shape compared to all the other schemes, next comes WENO-5, and KP being the least accurate scheme, with WENO-35 and WENO-33 falling between WENO-5 and KP schemes.

Finally, from the results attained from the three test cases, the decreasing order of accuracy of the schemes can be stated as $KL \geq WENO-5 > WENO-35 > WENO-33 > KP$. The external limiters i.e. BP and PP limiters used in WENO type and KL schemes did not degrade the order of accuracy. From the results (min/max values) in test case two and three, it can be clearly seen that, there are no overshoots or undershoots (spurious oscillations) in the solution, and strictly positive solution is attained for WENO type and

KL schemes, where I utilized BP and PP filters, this proves that the limiters are effective.

Chapter 5

Numerical Experiments on the Cubed-Sphere Geometry

The cubed-sphere geometry is illustrated and the procedure adopted to patch the faces of the cubed-sphere is given here in this chapter. The C-FV schemes are evaluated on the cubed-sphere using the standard test suite which consists of solid body rotation and deformational tests.

Sadourny [63] originally introduced the quasi-uniform spherical grid (or “cubed-sphere”) to avoid the pole problems associated with the conventional latitude-longitude spherical grids. Recently, the cubed-sphere geometry [62, 61] became popular in global modeling, because it offers a quasi-uniform rectangular grid (logically rectangular) on the sphere. This type of grid system is ideally suited for the cell-centered FV methods [59, 6, 71, 32] or the high-order element-based Galerkin methods [45].

Spherical coordinates are typically used for the equations in global atmospheric models. The notation given in Pedlosky [57] and Durran [14] is used here, locations on the surface of the sphere are given in terms of longitude (λ) and latitude (θ), and the horizontal wind is given by $\mathbf{v} = (u, v)$, where u and v are orthogonal components in the West-East and South-North directions, respectively.

5.1 CUBED-SPHERE GEOMETRY

A new level of parallelism (2D domain decomposition) is supported by cubed-sphere geometry, which is a highly desirable quality for currently available massively parallel computer architectures. There are different variants for the cubed-sphere grid system, however, I consider the cubed-sphere geometry employing the equiangular central (gnomonic) pro-

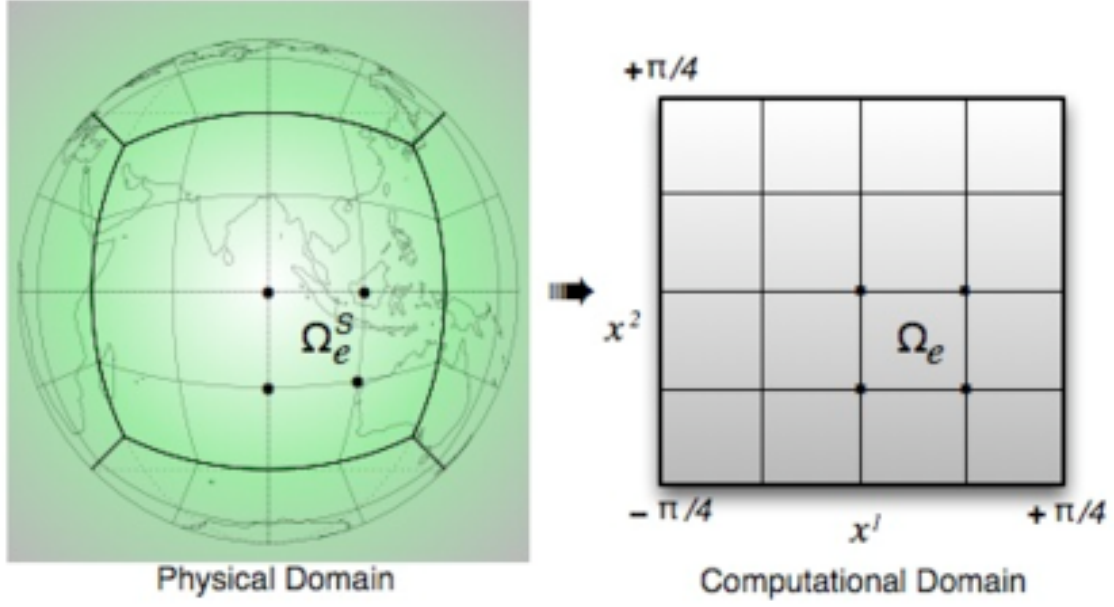


Figure 5.1: A cubed-sphere generated by equiangular central projection. Each face of the cubed-sphere is partitioned into $N_c \times N_c$ cells (control volumes) for the FV discretization, $6 N_c^2$ cells span the entire spherical surface.

jection as described in [52].

In order to generate a cubed-sphere, a sphere \mathcal{S} with radius R_a is decomposed into six identical regions, by an equiangular central (gnomonic) projection of the faces of an inscribed cube. The central angles of projection $x^1 = x^1(\lambda, \theta)$, $x^2 = x^2(\lambda, \theta)$ are the local coordinates for each face such that $x^1, x^2 \in [-\pi/4, \pi/4]$, where λ and θ , are respectively, the longitude and the latitude of the sphere \mathcal{S} . This results in a non-orthogonal curvilinear coordinate system (x^1, x^2) , which is free of singularities. Figure. (5.1) shows a cubed-sphere with $N_c \times N_c$ cells (control volumes) on each face. The orientation of the different cube faces and their local connectivity is shown in Figure. (5.2), where the lateral faces are identified by $\mathcal{F}_n, n = 1, \dots, 4$, and the top and bottom faces are \mathcal{F}_5 and \mathcal{F}_6 , which represent north and south polar panels, respectively.

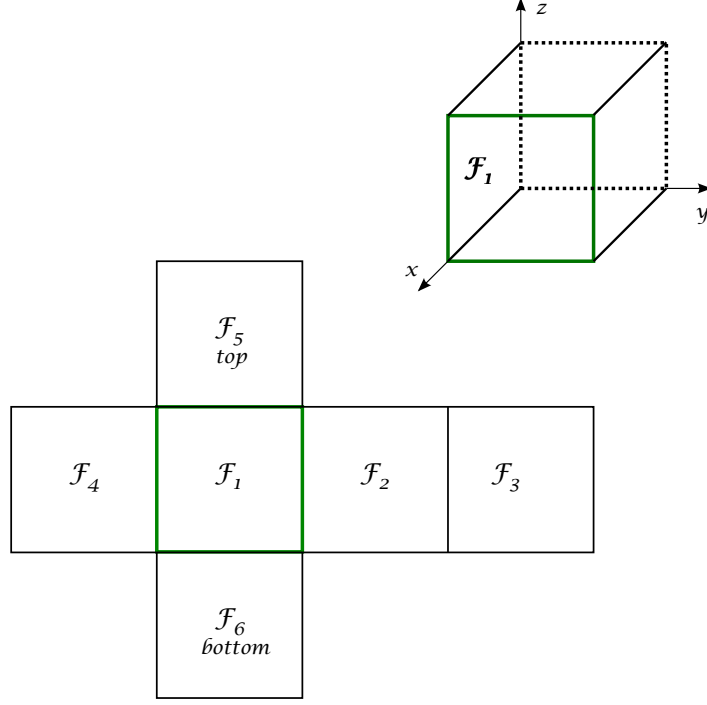


Figure 5.2: Schematic showing orientation of the different cube faces and their local connectivity. The cube faces are marked as \mathcal{F}_n , $n = 1, \dots, 6$.

The metric tensor associated with the central projection is given by:

$$g_{ij} = \frac{R_a^2}{\rho^4 \cos^2 x^1 \cos^2 x^2} \times \begin{bmatrix} 1 + \tan^2 x^1 & -\tan x^1 \tan x^2 \\ -\tan x^1 \tan x^2 & 1 + \tan^2 x^2 \end{bmatrix} \quad (5.1)$$

where $\rho^2 = 1 + \tan^2 x^1 + \tan^2 x^2$, and the tensor indices $i, j \in \{1, 2\}$. The Jacobian (metric term) of the transformation is $\sqrt{g} = \sqrt{\det[g_{ij}]}$. The horizontal velocity vector on the sphere $\mathbf{v}(\lambda, \theta) = (u_s, v_s)$ can be expressed in terms of covariant (u_1, u_2) and contravariant (u^1, u^2) vectors, which are related through the tensor relation $u_i = g_{ij}u^j$, $u^i = g^{ij}u_j$ where $g^{ij} = g_{ij}^{-1}$. For each face of the cubed-sphere,

$$\begin{bmatrix} u^1 \\ u^2 \end{bmatrix} = \mathbf{A}^{-1} \begin{bmatrix} u_s \\ v_s \end{bmatrix}, \quad \begin{bmatrix} u_1 \\ u_2 \end{bmatrix} = \mathbf{A}^T \begin{bmatrix} u_s \\ v_s \end{bmatrix}$$

where

$$\mathbf{A} = R_a \begin{bmatrix} \cos \theta (\partial \lambda / \partial x^1) & \cos \theta (\partial \lambda / \partial x^2) \\ \partial \theta / \partial x^1 & \partial \theta / \partial x^2 \end{bmatrix}.$$

The matrix \mathbf{A} is local to each face of the cubed-sphere such that $g_{ij} = \mathbf{A}^T \mathbf{A}$. The details of the local transformation laws and the matrix \mathbf{A} are given in Appendix A.5.

5.2 DISCRETIZING THE ADVECTION EQUATION ON A CUBED SPHERE

The advection equation in the curvilinear coordinates on the sphere without the source term, is equivalent to the following:

$$\frac{\partial \phi}{\partial t} + \frac{1}{\sqrt{g}} \frac{\partial}{\partial x^1} [u^1 \sqrt{g} \phi] + \frac{1}{\sqrt{g}} \frac{\partial}{\partial x^2} [u^2 \sqrt{g} \phi] = 0 \quad (5.2)$$

The equation can be rearranged in the following flux form similar to Equation (3.12),

$$\frac{\partial}{\partial t} [\psi] + \frac{\partial}{\partial x^1} [F_1(\psi)] + \frac{\partial}{\partial x^2} [F_2(\psi)] = 0 \quad (5.3)$$

where $\psi = \sqrt{g} \phi$ and fluxes $F_1(\psi) = u^1 \psi$, $F_2(\psi) = u^2 \psi$. The solution procedure for Equation (5.3) in (x^1, x^2) -space is the same as that for the 2D Cartesian case (see, [37], for the details including treatment of fluxes at the cubed-sphere edges).

5.2.1 Arrangement of Cells on a Cubed-Sphere

The computational physical arrangement of cells on a cubed-sphere is clearly shown in Figure. (5.3). The thick dots in the figure are the cell centers for individual cells. Due to the equi-angular projection of the grid on cube onto a sphere, a logically rectangular grid on the sphere is attained and the cell width in x^1 - and x^2 - direction are equal, i.e. $\Delta x^1 = \Delta x^2$. In the Figure. (5.3), $10 \times 10 \times 6$ number of cells span the entire surface of the sphere.

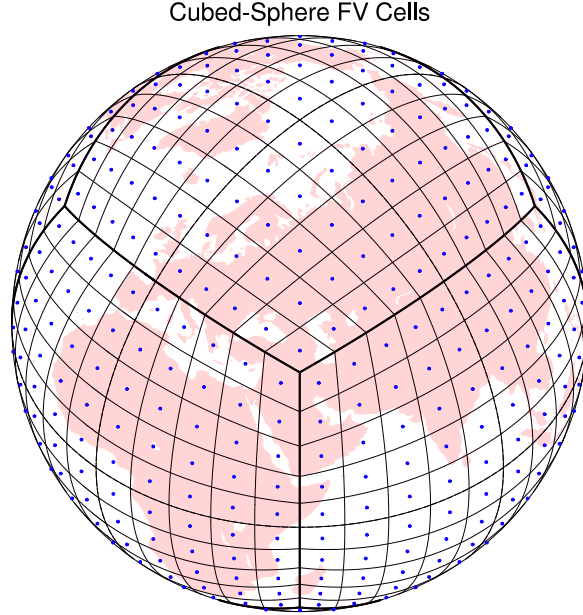


Figure 5.3: Schematic of cell centers (FV cells) on a cubed-sphere geometry. In this figure each face has 10×10 cells and $10 \times 10 \times 6$ cells span the surface of the sphere.

5.3 GHOST CELLS

As explained above, each face of the cubed-sphere has rectangular cells and can be dealt with differently, but to couple all the faces together, one needs to carefully pass the values between faces i.e. element values must be remapped across coordinate discontinuities, and moreover the C-FV schemes herein require information from neighboring cells in order to evaluate the fluxes. This requirement results in the need for wider ghost regions near coordinate discontinuities on parallel systems in order to accommodate remapping. Schemes with local degrees of freedom, for example DG and SE methods, may be more favorable in this aspect since communication between neighboring faces is not required, and hence computation can be distributed evenly on parallel architectures. At all the boundaries of each cubed-sphere one needs to create ghost cells, whose values can be attained from neighboring faces. One method for is to directly copy the values from the cells in the neighboring face to the ghost cells, this method is inexpensive but not very accurate, especially for non-

linear case (e.g. shallow water model). Another method is to obtain the values by doing an interpolation as described in ([62], [5]), which is adapted here in the present work. The interpolation should be done in Cartesian or spherical coordinates form before and then transform into the cubed-sphere coordinates form, because the coordinate bases differ from one face to another on the cubed-sphere. I used a linear interpolation rather than using a high order interpolation since it did not impact the accuracy of the schemes, only 1D interpolation is needed since the center points of ghost cells lie on the same line as the center points of the cells in the neighboring face, it can be clearly seen in Figure. (5.4).

CS: Face-Edge Halo Regions

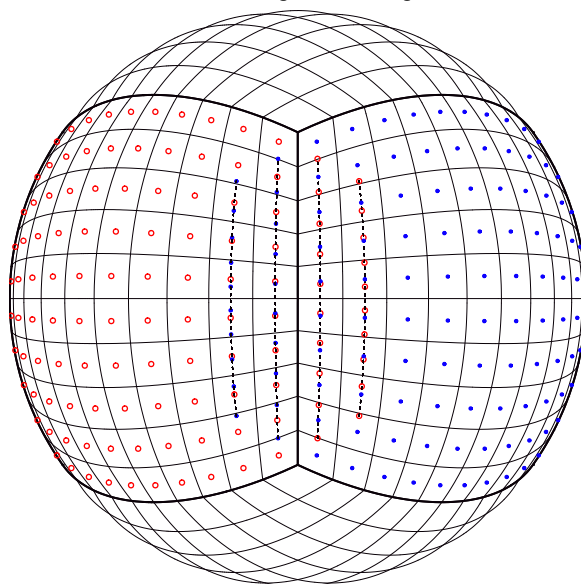


Figure 5.4: Treatment of connectivity between each face for the cubed-sphere. The center points of ghost cells lie on the same line as the center points of cells on the neighboring face.

5.4 LINEAR TRANSPORT PROBLEM ON THE CUBED-SPHERE

The C-FV schemes, tested in Cartesian cases are again analyzed by solving Equation (5.3) on the cubed-sphere. For the spherical advection experiments, I use benchmark tests such as the solid-body rotation of a cosine-bell and the deformational-flow tests. One

can use the point-values created at the cell-centers with the (analytic) initial condition $\phi(t = 0)$, as the cell-averages [32]. The cell centers for the cells on a cubed-sphere geometry are clearly shown in Figure. (5.3). However, for better consistency, I create 3×3 point-values initially on each cell (see Figure. (3.4)), and then the cell-averaged value $\bar{\phi}_{ij}$ is computed by the following Simpsons averaging formula:

$$\bar{\phi}_{ij} = \frac{1}{36} \left(\phi_{i-1/2,j-1/2} + \phi_{i-1/2,j+1/2} + \phi_{i+1/2,j-1/2} + \phi_{i+1/2,j+1/2} + 4\phi_{i-1/2,j} + 4\phi_{i+1/2,j} \right. \\ \left. + 4\phi_{i,j-1/2} + 4\phi_{i,j+1/2} + 16\phi_{ij} \right). \quad (5.4)$$

The normalized standard errors ℓ_1 , ℓ_2 and ℓ_∞ used for the test-cases are as those defined in [49].

5.4.1 Solid-Body Rotation of a Cosine-Bell

I first consider the solid-body rotation test proposed by Williamson [75], where a “cosine-bell” is used as scalar field ϕ . Since the exact solution is known at all times, error measures can be computed. Initially the cosine-bell is defined as follows:

$$\phi(\lambda, \theta, 0) = \begin{cases} (h_0/2) [1 + \cos(\pi r_d/r_0)] & \text{if } r_d < r_0 \\ 0 & \text{if } r_d \geq r_0 \end{cases}$$

where r_d is the great-circle distance between (λ, θ) and center of the bell. The cosine-bell with base radius $r_0 = R_a/3$ is placed at $(3\pi/2, 0)$, which corresponds to the center of face (\mathcal{F}_4) on the cube. The height of the bell is $h_0 = 1000\text{m}$, and radius of the earth $R_a = 6.37122 \times 10^6\text{m}$. The spherical velocity components (u_s, v_s) of the non-divergent wind field is defined to be:

$$u_s = u_0(\cos \alpha_0 \cos \theta + \sin \alpha_0 \cos \lambda \sin \theta), \\ v_s = -u_0 \sin \alpha_0 \sin \lambda.$$

Here $u_0 = (2\pi R_a)/(12 \text{ days})$ and α_0 is the axis of cosine-bell rotation and the polar axis of the spherical co-ordinate system. When $\alpha_0 = 0, \pi/2$ and $\pi/4$, the flow is oriented

along the equator (east-west), poles (north-south) and diagonal (north-east) directions, respectively. The flow along north-east direction is the most challenging case, since the bell passes through four vertices and two edges to complete one revolution around the sphere, I use this particular configuration.

First, I demonstrate the effect of BP and PP filters on WENO schemes with the cosine-bell advection test. For this experiment WENO-35 scheme was selected on a $48 \times 48 \times 6$ cubed-sphere grid ($N_c = 48$). It takes 12 simulated days (288 hours) to complete one revolution around the sphere, and time step was chosen such that $CFL = 0.25$. The solutions after one revolution are shown in Figure. (5.5) for different combinations of the filters. Without using any filter WENO-35 scheme produces spurious oscillations (see, Figure. (5.5) panel (b), where the minimum value ≈ -21). Spurious oscillations in the solution are successfully suppressed by the BP filter. Nevertheless, there are still minute negative values ($\mathcal{O}(-10^{-5})$) left in the solution, which are completely removed by applying the PP filter, as seen in Figure. (5.5) panel (d). Time traces of normalized ℓ_2 error are given in Figure. (5.6) for different combinations of the filters.

The ℓ_2 error plots for WENO-35 with BP and PP filter is less than that without filters. This clearly shows that application of BP and PP filters with WENO-35 will not degrade the accuracy of the scheme per se, instead there is an improvement in the accuracy.

In Figure. (5.7), time traces of normalized ℓ_1 , ℓ_2 and ℓ_∞ errors for the cosine-bell test are shown, with the schemes KP, WENO-33, WENO-35, WENO-5 and KL. The cubed-sphere grid with $N_c = 90$ (i.e., approximately equal to 1° resolution), and a the time-step is chosen such that $CFL = 0.25$. Note that KP scheme is non-oscillatory and WENO and KL schemes include both BP and PP the filters making them monotonic. By comparing the five schemes, WENO-5 and KL stand out in terms of errors measures and efficiency, and KP scheme found to be least accurate. The error measures of schemes (WENO-35, WENO-5 and KL) are comparable to that of the fourth-order FV schemes developed by Putman et. al. [59]. The results with WENO-5 and Kl schemes are comparable to the results reported for recent cubed-sphere based FV schemes, including a FV semi-Lagrangian CSLAM [32],

Demonstration of Filters: Cosine-Bell Advection Test

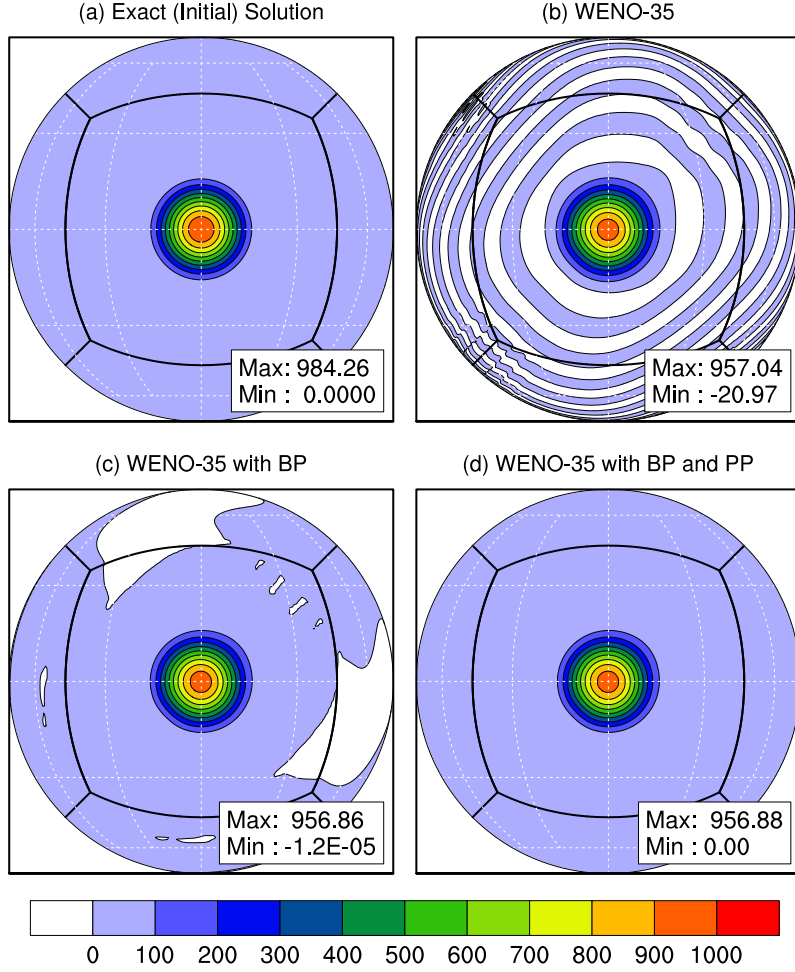


Figure 5.5: Results of cosine-bell advection test on the cubed-sphere after one revolution (12 days) with the WENO-35 scheme. The wind field is oriented along the north-east direction ($\alpha_0 = \pi/4$), on a $48 \times 48 \times 6$ grid (or $N_c = 48$), with $CFL = 0.25$. The panels (a) indicates the initial (cell-averaged) height of the cosine-bell, (b) numerical solution without any filter, (c) solution with BP filter and (d) solution with BP and PP filter.

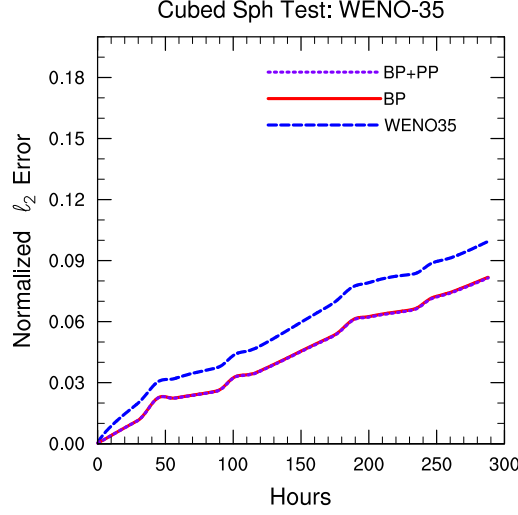


Figure 5.6: Time traces of the normalized ℓ_2 error for the simulations in Figure 5.5. Different combinations of filters used with the WENO-35 scheme, and the BP filter enhances the accuracy of the scheme.

and a third-order non-oscillatory DG scheme by [78].

5.4.2 Deformational Flow Test: Moving Vortices

First deformational test used is the “moving vortices” test-case introduced in [47]. Two steady vortices are created on a sphere, whose centers are located at diametrically opposite sides. The flow field is non-divergent, time-dependent and highly deformational, the vortices move along a great-circle trajectory while deforming, with known analytic solution. This test is more challenging than solid-body rotation test, and particularly useful for advection schemes developed on cubed-sphere geometry. For the current tests, vortex flow-field is oriented along the north-east direction ($\alpha_0 = \pi/4$) so that the vortex centers pass through the vertex and edges of the cubed-sphere. The analytic solution at time t is defined by Nair et. al. [47]:

$$\phi(\lambda', \theta', t) = 1 - \tanh \left[\frac{\rho}{\gamma_0} \sin(\lambda' - \omega(\theta')t) \right],$$

where (λ', θ') is the rotated spherical coordinates with respect to the regular (λ, θ) coor-

Normalized Errors: Cosine-Bell Advection Test

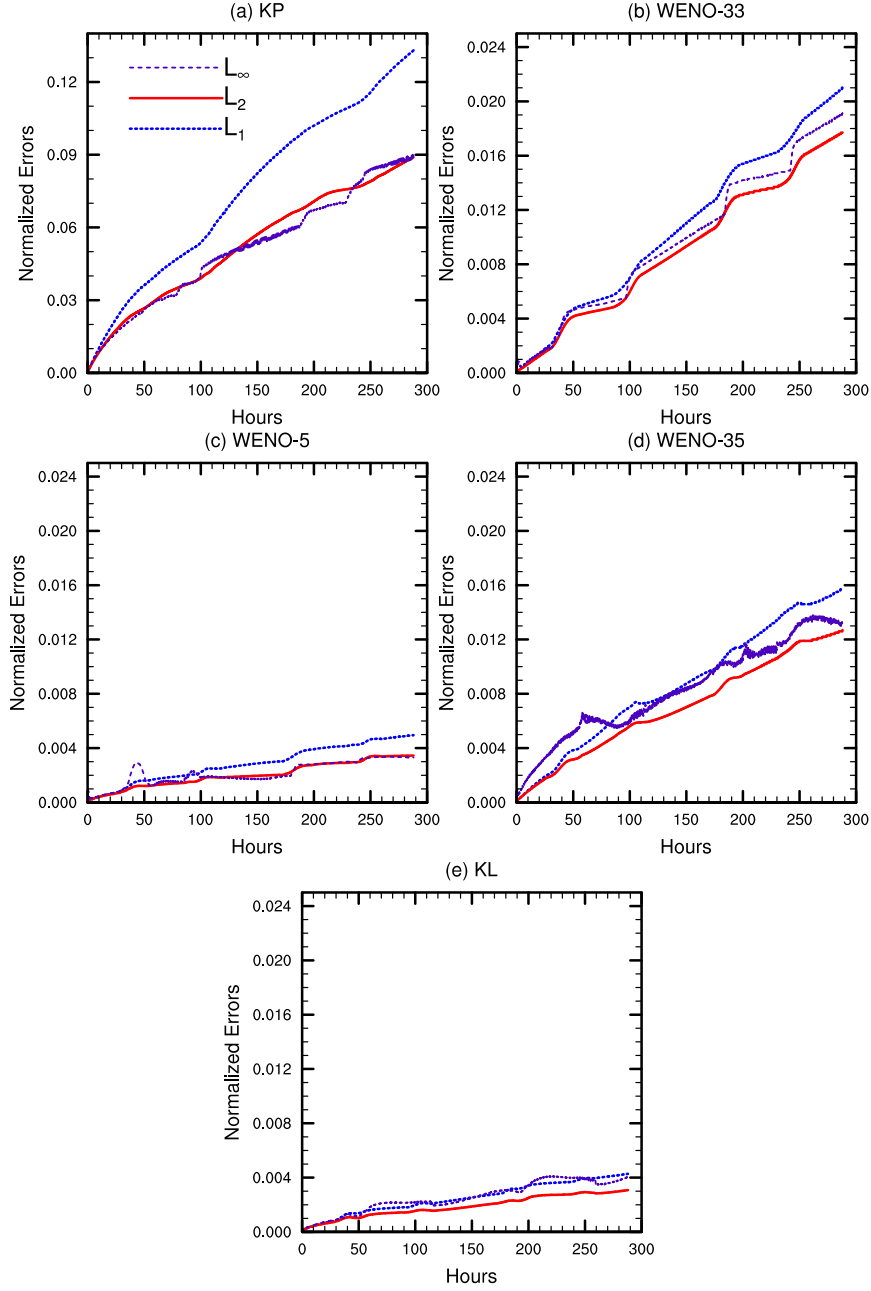


Figure 5.7: Time traces of the normalized errors ℓ_1 , ℓ_2 and ℓ_∞ for cosine-bell advection test. With (a) KP, (b) WENO-33, (c) WENO-5, (d) WENO-35 and (e) KL schemes. Flow is along north-east direction ($\alpha_0 = \pi/4$) on a cubed-sphere with $N_c = 90$ (1° resolution), and $CFL = 0.25$ for all simulations. Note that y -axis scaling for KP scheme is different from that of the WENO schemes.

(a) Initial Field

(b) WENO-35: Field after 6 Days

(c) WENO-35: Final (12 Days) Field

0.5 0.6 0.7 0.8 0.9 1 1.1 1.2 1.3 1.4 1.5

ordinates, $\rho = \rho_0 \cos \theta'$ is the radial distance of the vortex, and the parameters $\rho_0 = 3$, $\gamma_0 = 5$.

$$\omega(\theta') = \begin{cases} V_t/(R_a\rho) & \text{if } \rho \neq 0, \\ 0 & \text{if } \rho = 0. \end{cases}$$
$$V_t = u_0 \frac{3\sqrt{3}}{2} \text{sech}^2(\rho) \tanh(\rho)$$

54

sphere. The time-dependent wind field (u_s, v_s) is given by:

$$\begin{aligned}
u_s(t) &= u_0 (\cos \theta \cos \alpha_0 + \sin \theta \cos \lambda \sin \alpha_0) + \\
&\quad R_a \omega \{ \sin \theta_c(t) \cos \theta - \cos \theta_c(t) \cos [\lambda - \lambda_c(t)] \sin \theta \}, \\
v_s(t) &= -u_0 (\sin \lambda \sin \alpha_0) + \\
&\quad R_a \omega \{ \cos \theta_c(t) \sin [\lambda - \lambda_c(t)] \}.
\end{aligned}$$

where α_0 is the flow orientation parameter as used in the solid-body rotation case. Initial conditions for vortex field is $\phi(\lambda, \theta, 0)$, with a vortex center kept at $[\lambda_c(t=0), \theta_c(t=0)] = (3\pi/2)$.

The cubed-sphere resolution is chosen to be $80 \times 80 \times 6$ (or $N_c = 80$, corresponds to 1.125° resolution at the equator) so that the results could be compared to that with CSLAM and FV [59] schemes. Maximum CFL is set to 0.25 and the flow-fields are oriented along the north-east direction ($\alpha_0 = \pi/4$). Figure. (5.8) shows the initial, halftime (6 days) and final (12 days) vortex fields in panels (a), (b) and (c), respectively, where the numerical simulations (panels (b) and (c)) are done with the WENO-35 scheme. Height errors (difference between exact and numerical solution) after full evolution (or one revolution after 12 days) shown in Figure. (5.9), for KP, WENO-33, WENO-5, WENO-35 and KL schemes on panels (a), (b), (c), (d) and (e), respectively. Here again results with the WENO-5 and KL schemes are better in terms of error norms (see Figure. (5.10)) and the KP scheme gives least accurate results (note the maximum and minimum values given in the figure). The WENO-33 performs better than KP scheme but falls behind WENO-35, WENO-5 and KL schemes. For the same experiment, WENO-5 and KL perform slightly better than a monotonic version of CSLAM and a 7-th order FV [59] schemes.

5.4.3 Deformational Flow Test: Slotted-Cylinders

To further validate the five C-FV schemes on the sphere, I use a challenging benchmark deformational flow test-case recently developed by Nair et. al. [49]. I am particularly interested in two cases with non-smooth (twin slotted-cylinder) and quasi-smooth (twin

Height Errors: Moving-Vortices Test

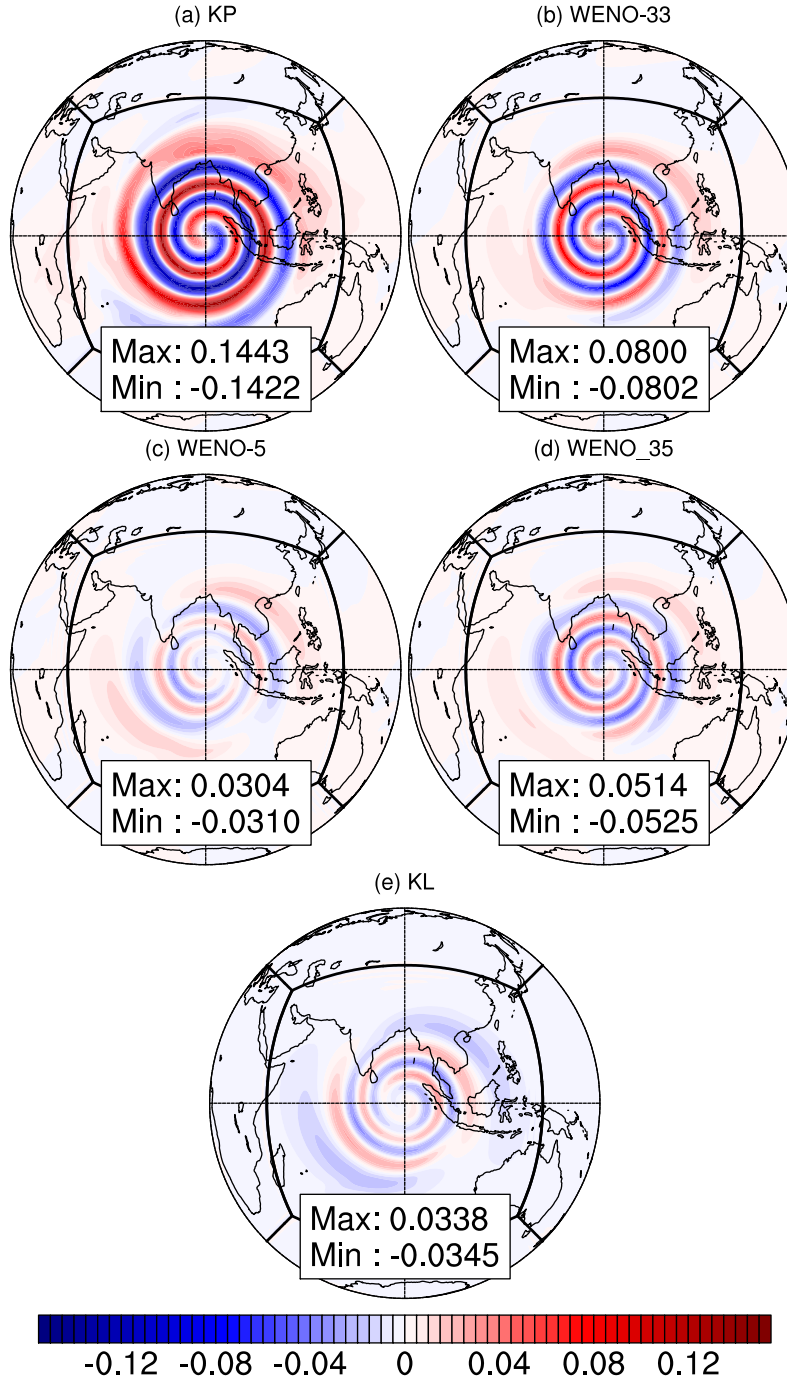


Figure 5.9: Height errors (numerical - analytic) after a revolution with the moving vortices test on $80 \times 80 \times 6$ grid. (a) KP, (b) WENO-33, (c) WENO-5 and (d) WENO-35 schemes, other experiment setting is same as in Figure. (5.8).

cosine-bell) initial conditions. The initial distributions are deformed into thin filaments half way through the simulation while they are being transported along the zonal direction by the solid-body component of the flow. The analytical solution is known only at the end of the simulation.

The initial twin slotted-cylinder data is given by:

$$\phi(\lambda, \theta) = \begin{cases} c & \text{if } r_i \leq r, |\lambda - \lambda_i| \geq r/6, i = 1, 2, \\ c & \text{if } r_1 \leq r, |\lambda - \lambda_1| < r/6, \theta - \theta_1 < -5/12r, \\ c & \text{if } r_2 \leq r, |\lambda - \lambda_2| < r/6, \theta - \theta_2 > 5/12r, \\ b & \text{otherwise,} \end{cases}$$

where $c = 1$, $b = 0.1$, the radius of the cylinder $r = 1/2$ and $r_i = r_i(\lambda, \theta)$ is the great-circle distance between (λ, θ) and a specified center (λ_i, θ_i) , which is defined as:

$$r_i(\lambda, \theta) = \arccos[\sin \theta_i \sin \theta + \cos \theta_i \cos \theta \cos(\lambda - \lambda_i)].$$

The initial positions of the centers of the distributions are at $(\lambda_1, \theta_1) = (5\pi/6, 0)$ and $(\lambda_2, \theta_2) = (7\pi/6, 0)$, respectively. The slots are oriented in opposite directions for the two cylinders so that they are symmetric with respect to the flow. Figure. (5.11) panel (a) shows the initial position.

For the quasi-smooth case, the slotted cylinders are replaced by two symmetrically located cosine bells, which are defined as follows:

$$\phi(\lambda, \theta) = \begin{cases} b + c h_1(\lambda, \theta) & \text{if } r_1 < r, \\ b + c h_2(\lambda, \theta) & \text{if } r_2 < r, \\ b & \text{otherwise.} \end{cases} \quad (5.5)$$

where $c = 0.9$, $b = 0.1$ and

$$h_i(\lambda, \theta) = \frac{h_{\max}}{2} [1 + \cos(\pi r_i / r)] \quad \text{if } r_i < r.$$

Other parameters are the same as those used for the slotted-cylinder case.

The wind field is non-divergent but highly deformational. The initial distributions are deformed into thin filaments half way through the simulation while they are being

Normalized Errors: Moving Vortices Test

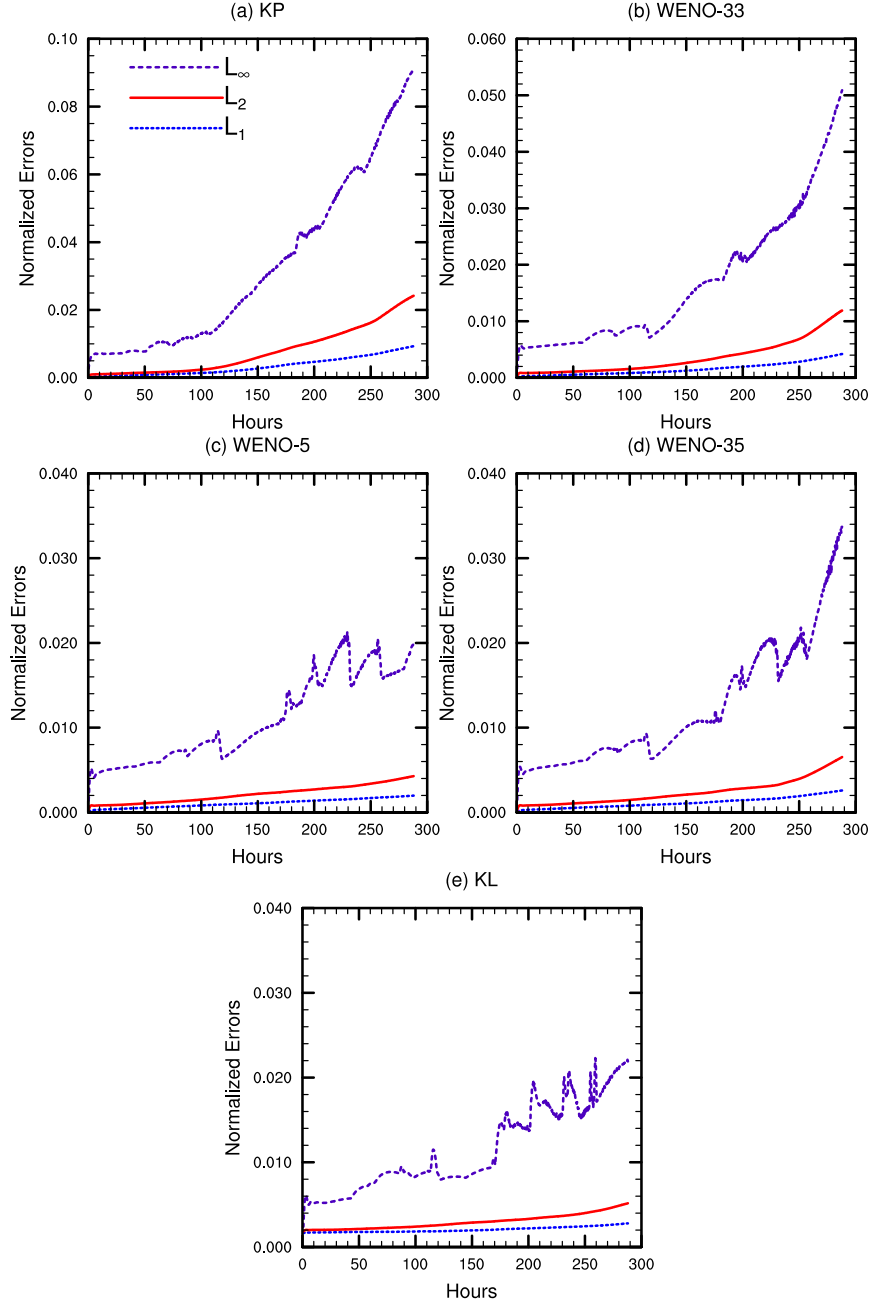


Figure 5.10: Time evolution of the normalized error norms ℓ_1 , ℓ_2 and ℓ_∞ for (a) KP, (b) WENO-33, (c) WENO-5, (d) WENO-35 and (e) KL schemes. All other settings are same as in Figure 5.8. Note that y -axis scaling for WENO-5, KL and WENO-35 are different from that of KP and WENO-33.

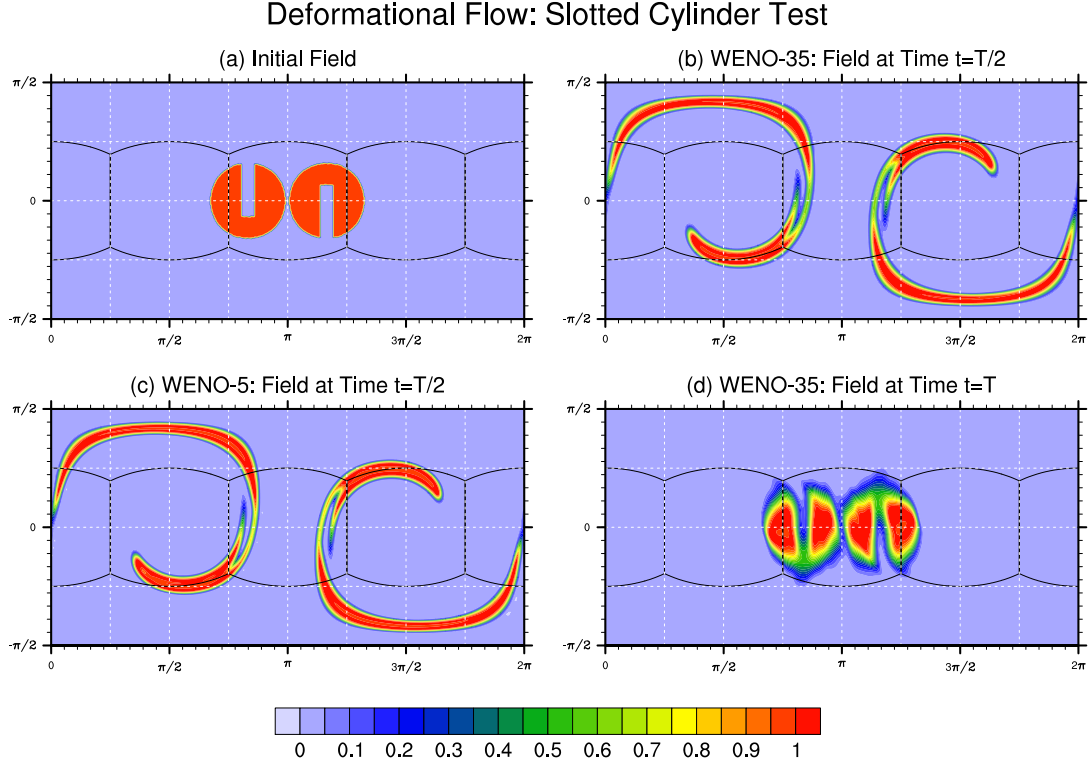


Figure 5.11: Numerical solution for the deformational flow test on a cubed sphere with mesh $90 \times 90 \times 6$ with twin slotted cylinders as initial condition. The initial solution is shown in the panel (a), these two cylinders move along the zonal direction while deforming, and reach at the initial position after making a complete revolution (12 days). Panels (b) and (d) show the solution after time $T/2$ and T ($=5$) respectively using WENO-35 scheme, and panel (c) shows the solution after time $T/2$ using WENO-5 scheme. A CFL of 0.75 is used for the simulation.

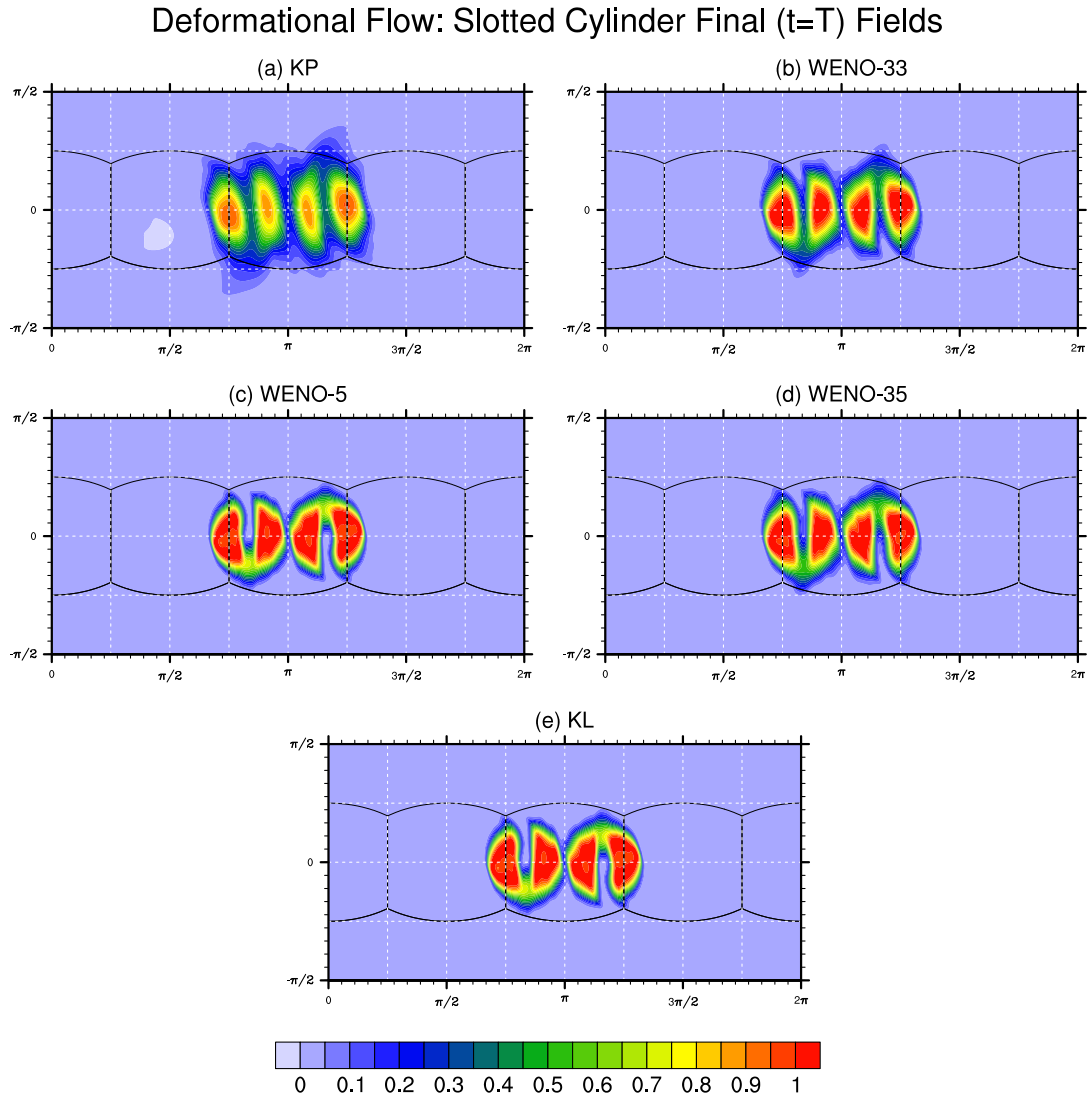


Figure 5.12: Same as in Figure 5.11, but the panels (a), (b), (c) and (d) indicate the solution after one cycle of revolution using KP, WENO-33, WENO-5 and WENO-35 schemes respectively.

transported along the zonal direction by the solid-body component of the flow. Note that an exact solution for this test is only available at the final time $t = T$, and it is identical to the initial condition. The time dependent non-divergent wind field is defined as:

$$\begin{aligned} u_s(\lambda, \theta, t) &= \kappa \sin^2(\lambda') \sin(2\theta) \cos(\pi t/T) + 2\pi \cos(\theta)/T \\ v_s(\lambda, \theta, t) &= \kappa \sin(2\lambda') \cos(\theta) \cos(\pi t/T) \end{aligned}$$

where $\lambda' = \lambda - 2\pi t/T$, $\kappa = 2.0$, and $T = 5$ units.

Figure. (5.11) shows the results of the deformational flow tests with the WENO-35 scheme, on panels (b) and (d) at half-time ($t = T/2$) and final-time ($t = T$). In Figure. (5.11), panel (c) shows the results with WENO-5 at halftime. Maximum CFL for this simulation was 0.75, on a cubed-sphere grid with $N_c = 90$. Numerical results with the five C-FV schemes are shown in Figure. (5.12) at final time $t = T$. WENO-5, KL and WENO-35 schemes results are comparable to those reported in [49]. For the KP scheme, the final solution is very much diffused, this may due to excessive limiting. WENO-33 solution is inferior to that by other WENO variants. It can be clearly seen that the WENO and KL schemes preserve the shape of the slotted cylinders better than KP scheme. Moreover, it is clear from Figure. (5.12) that BP and PP filters used in WENO schemes completely remove the spurious oscillations and produce a positive definite solution.

I roughly calculated the execution time taken by each scheme for the same test, by using the KP scheme as a baseline. In Figure. (5.13), the thick line indicates the relative execution time of each scheme compared to KP scheme's execution time. For each scheme the time factor is calculated as a ratio of execution time by KP scheme and that by individual scheme. From the results it is clear that WENO-33 and WENO-35 schemes take more time to compute than KP scheme, where as WENO-5 and KL schemes has less execution time than KP scheme. In the same way the ℓ_2 error is also compared, and is indicated by the dashed line in Figure. (5.13). The results indicate that the accuracy for the schemes can be represented in the following way: $KP < WENO-33 < WENO-35 < WENO-5 \cong KL$.

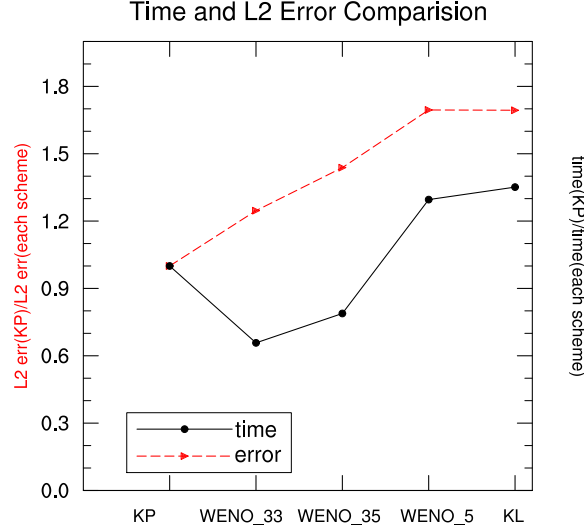


Figure 5.13: A performance comparison of WENO schemes with respect to the KP scheme for the slotted-cylinder test, execution time and ℓ_2 error measure are used for this comparison. The solid-line indicates execution time comparison, estimated as the ratio of the time taken by KP scheme and the time taken by each scheme. Similarly, the dashed line indicates ℓ_2 error comparison, estimated as the ratio of ℓ_2 error of KP scheme and ℓ_2 error of each scheme. It shows that KL and WENO-5 are more efficient and accurate than other three central schemes, while WENO-33 is most computationally expensive.

5.4.4 Deformational Flow Test: Twin Cosine-Bells

I repeated the experiment given in Section. (5.4.3), for quasi-smooth deformational test by using twin cosine-bells. For this test case CFL maximum value is set to 0.50, the normalized standard errors for different schemes are given in Table. (5.1). The error norms are computed as recommended in [49], the results obtained from WENO-5 and KL schemes are comparable to that with a third-order DG method [78].

5.5 DISCUSSION AND SUMMARY

Cubed-sphere geometry is considered to analyze the performance of the five C-FV

Table 5.1: Error norms for deformational-flow test with twin cosine-bells on a cubed sphere, with $N_c = 90$ and a CFL maximum value set to 0.50. All four C-FV schemes are used for the test.

Scheme	ℓ_1	ℓ_2	ℓ_∞	ϕ_{max}	ϕ_{min}
KP	0.1550	0.3362	0.4804	-0.5070	-0.0006
WENO-33	0.0764	0.1618	0.2208	-0.2310	-0.0373
WENO-5	0.0175	0.0347	0.0533	-0.0314	-0.0253
WENO-35	0.0438	0.0942	0.1276	-0.1270	-0.0382

schemes on a sphere (Earth). I developed all the five C-FV schemes to solve the transport problem on a cubed-sphere. The details of the transformation between cube and sphere, and patch interface of the faces on the cubed-sphere are explained in detail here in this chapter.

Solid-body rotation and deformational tests namely solid-body rotation of a cosine bell, deformational flow of moving vortices, two slotted cylinders and two cosine-bells are employed to validate C-FV schemes on a cubed-sphere. From the results, it is clear that KL and WENO-5 produce more accurate results than all the other schemes, with KP scheme producing least accurate results. The filters BP and PP are effective, i.e. they suppress the spurious oscillations and produce strictly positive solution. The accuracy in the increasing order from the results can be stated as $KP < WENO-33 < WENO-35 < WENO-5 \cong KL$. The error measures of schemes WENO-5 and KL are comparable to that of a FV semi-Lagrangian CSLAM [32], and a third-order non-oscillatory DG scheme by Nair et al. [78], a fourth-order FV scheme by Ullrich et al. [71], a 7-th order FV scheme by Putman et al. [59], and a FV scheme by multi-moment by Chen et al. [6].

Time and error comparison is done using the deformational flow test of two slotted cylinders, WENO-5 and KL produce accurate results and computationally less expensive than KP, WENO-33 and WENO-35. WENO-35 and WENO-33 take more time to compute

than KP scheme but produce better results. WENO-35 takes less time to produce more accurate results than WENO-33 scheme.

The C-FV schemes considered here are simple and computationally less expensive than the ones mentioned in Ullrich et al. [71], that uses Riemann solvers (computationally expensive). The FV scheme given in [6] is also expensive than the C-FV schemes mentioned here. The computational stencil is smaller when compared to the stencil utilized for fourth-order FV scheme in [71]. These schemes also have the potential to be highly scalable to many processors and utilize the massive computing power available today, these properties make them good contenders for global atmospheric models.

Chapter 6

The Shallow Water Model

This chapter consists of FV discretization of shallow water equations (SWE) on the cubed-sphere geometry. I only considered three C-FV schemes from the five schemes to do the analysis with shallow water model on the cubed-sphere, since I am convinced from the results obtained for transport problem, that WENO-35, WENO-5 and KL schemes outperform the rest. I demonstrate the performance of these three schemes using test suite developed by Williamson [75]. In this work, I consider the cubed-sphere geometry and the continuous flux form non-linear shallow water (SW) equations in curvilinear coordinates to test the performance of C-FV schemes.

6.1 SHALLOW WATER MODEL

The shallow water equations are derived from depth-integrating Navier-Stokes equations, the horizontal length scale is considered to be much greater than the vertical length scale. Under this condition, conservation of mass implies that the vertical velocity of the fluid is insignificant. The SWE are used for studying the horizontal aspects of atmospheric dynamics, and are also used as test-bed to evaluate various discretization techniques ([75], [72]).

The flux form or conservative form of SWE on a rotating sphere are defined as ([50], [57]):

$$\frac{\partial}{\partial t}(h\mathbf{v}) + \nabla \cdot (\mathbf{v}h\mathbf{v}) = -f\hat{\mathbf{k}} \times h\mathbf{v} - g_r h \nabla(h + h_s), \quad (6.1)$$

$$\frac{\partial}{\partial t}(h) + \nabla \cdot (h\mathbf{v}) = 0. \quad (6.2)$$

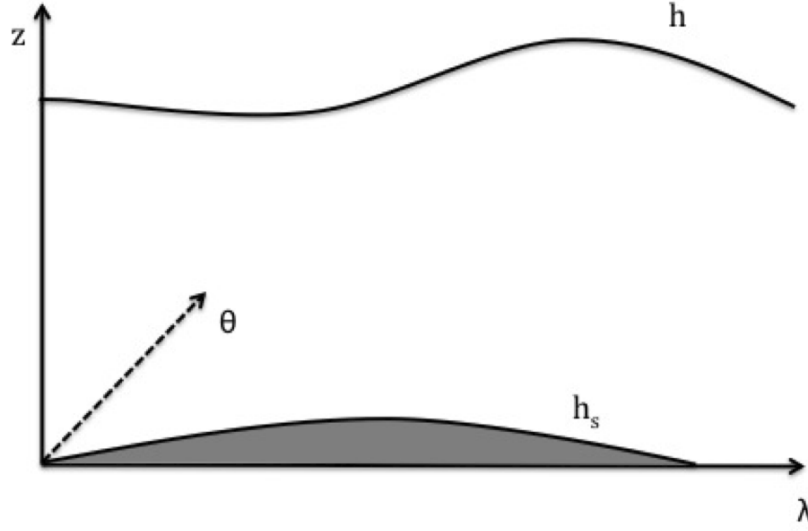


Figure 6.1: Schematic of shallow water model, which consists of a thin sheet of fluid of thickness h and h_s is the height of underlying mountains.

Here, h is the height of the fluid above the solid surface and is related to free surface geo-potential height (above sea level) $\phi = g_r(h_s + h)$, here h_s is the height of underlying topography (mountains), which can be clearly seen in the Figure. (6.1), and gravitational acceleration is denoted by g_r . \mathbf{v} is the horizontal wind vector, f is the cariolis parameter, $\hat{\mathbf{k}}$ is the unit vector along the outward radial direction. Here the divergence ($\nabla \cdot$) and gradient (∇) are not particular to any spherical grid system. $(\mathbf{v}h\mathbf{v})$ is a second-order tensor term. For atmospheric modeling applications, the popular *vector invariant form*, a simplified version of the momentum equations can be represented by the following:

$$\frac{\partial}{\partial t}(\mathbf{v}) + \nabla(\phi + \frac{1}{2}\mathbf{v} \cdot \mathbf{v}) = -(\zeta + f)\hat{\mathbf{k}} \times \mathbf{v} \quad (6.3)$$

Here, $\zeta = \hat{\mathbf{k}} \cdot (\nabla \times \mathbf{v})$ is the relative vorticity. The Equation. 6.3 is still in flux form and the fluxes being addressed are the energy fluxes $(\phi + \frac{1}{2}\mathbf{v} \cdot \mathbf{v})$.

6.2 SHALLOW WATER MODEL ON THE CUBED-SPHERE

The SWE on cubed-sphere are treated in tensor form, the details of the transformations, vectors etc. are given in Section. 5.1. Flux form shallow water equations (SWE) in curvilinear coordinates are considered in this present work (see [63]). The governing equations for an inviscid flow of a thin layer of fluid in 2D are the horizontal momentum and continuity equations for the shallow water system in curvilinear coordinates, can be represented as follows ([63]; [2]; [61]):

$$\frac{\partial}{\partial t}(\sqrt{g}h) + \frac{\partial}{\partial x^1}(\sqrt{g}u^1h) + \frac{\partial}{\partial x^2}(\sqrt{g}u^2h) = 0, \quad (6.4)$$

$$\frac{\partial u_1}{\partial t} + \frac{\partial}{\partial x^1}(E) = \sqrt{g}u^2(f + \zeta), \quad (6.5)$$

$$\frac{\partial u_2}{\partial t} + \frac{\partial}{\partial x^2}(E) = -\sqrt{g}u^1(f + \zeta), \quad (6.6)$$

Where

$$E = \phi + \frac{1}{2}(u_1u^1 + u_2u^2), \quad \zeta = \frac{1}{\sqrt{g}} \left[\frac{\partial u_2}{\partial x^1} - \frac{\partial u_1}{\partial x^2} \right], \quad f = 2\omega \sin\theta.$$

Here f is the Coriolis parameter, and ω is the rotation rate of the earth, E is the total energy.

The six local Cartesian coordinate systems (x^1, x^2) are projected onto the sphere using equi-angular central projection ([52]), in such a way that $x^1 = x^1(\lambda, \theta)$, $x^2 = x^2(\lambda, \theta)$, and $-\frac{\pi}{4} \leq x^1, x^2 \leq \frac{\pi}{4}$. The flux form of the shallow water equations (6.4) - (6.6) can be written as:

$$\frac{\partial}{\partial t}(\psi) + \frac{\partial}{\partial x^1}\mathbf{F}_1(\psi) + \frac{\partial}{\partial x^2}\mathbf{F}_2(\psi) = \mathbf{S}(\psi) \quad (6.7)$$

Where $\psi = [\sqrt{g}h, u_1, u_2]^T$, $\mathbf{F}_1 = [\sqrt{g}hu^1, E, 0]^T$, $\mathbf{F}_2 = [\sqrt{g}hu^2, 0, E]^T$ and source term $\mathbf{S} = [0, \sqrt{g}u^2(f + \zeta), -\sqrt{g}u^1(f + \zeta)]^T$.

6.3 THE FV DISCRETIZATION OF SWE

For simplicity, a scalar component of Equation. (6.7) is considered to describe discretization. The flux form Equation. (6.7) can be represented as follows:

$$\frac{\partial u}{\partial t} + \nabla \cdot F(u) = S(u), \quad \text{in } D \times (0, T), \quad (6.8)$$

for all $(x^1, x^2) \in D$, and initial condition $u_0(x^1, x^2) = u(x^1, x^2, t = 0)$. In Equation. (6.7), $u = u(x^1, x^2, t)$, gradient operator $\nabla = (\partial/\partial x^1, \partial/\partial x^2)$, $F = (F_1, F_2)$ is the flux function, and $S(u)$ is the source term. D is the computational domain, spanning six identical non-overlapping sub-domains of the surface of cubed-sphere. Herein, I only define discretization for single sub-domain Ω , since all the faces of cubed-sphere are identical. The sub-domain Ω is partitioned into $N_c \times N_c$ non-overlapping rectangular cells $\Omega_{i,j}$, where $i, j = 1, 2, \dots, N_c$, so that $\Omega_{ij} = [(x^1 \in (x_{i-1/2}^1, x_{i+1/2}^1), x^2 \in (x_{j-1/2}^2, x_{j+1/2}^2))]$. The total number of cells on the cubed-sphere are $M = 6 \times N_c \times N_c$. The size of each cell is $x_i^1 = (x_{i+1/2}^1 - x_{i-1/2}^1)$ and $x_j^2 = (x_{j+1/2}^2 - x_{j-1/2}^2)$ in x^1 and x^2 directions respectively.

The semi-discrete Central-Upwind FV for Equation. (6.8) can be represented by the following:

$$\frac{\partial \bar{u}_{ij}}{\partial t} = \frac{-1}{\Delta x^1 \Delta x^2} \left[\sum_{k=1}^4 \int_{\gamma_k} \mathbf{H} \cdot \mathbf{n} \right] + \bar{S}_{ij}. \quad (6.9)$$

Here \mathbf{H} is the numerical flux defined at the cell walls (interfaces). The line integrals along the cell walls are evaluated using three-point Simpson's rule. The evaluation for the east wall is shown, and the evaluation for the other walls follows the same pattern. The formula is given as:

$$\int_{\gamma_{East}} \mathbf{H} \cdot \mathbf{n} \approx \frac{\Delta x^1}{6} [H_{i+1/2, j-1/2} + 4H_{i+1/2, j} + H_{i+1/2, j+1/2}]. \quad (6.10)$$

Here, $\Delta x^1 = (x_{i+1/2}^1 - x_{i-1/2}^1)$, width of the cell in x^1 direction. The flux formula given in [29] is employed to evaluate the fluxes for the proposed FV schemes and is given by the

following:

$$\begin{aligned}
H_{i+1/2,j} &= \frac{a_{i+1/2,j}^+ F(u_{i+1/2,j}^-) - a_{i+1/2,j}^- F(u_{i+1/2}^-)}{a_{i+1/2,j}^+ - a_{i+1/2,j}^-} \\
&+ \frac{a_{i+1/2,j}^+ a_{i+1/2,j}^-}{a_{i+1/2,j}^+ - a_{i+1/2,j}^-} \left[u_{i+1/2}^+ - u_{i+1/2}^- - A_f \right]. \quad (6.11)
\end{aligned}$$

where a^+ and a^- are right- and left-sided local speeds which are introduced due to the discontinuities along the lines, they can be evaluated using:

$$a^+ = \max \left\{ u^1 \pm \sqrt{\phi g^{11}}, u^1, 0 \right\}, \quad a^- = \min \left\{ u^1 \pm \sqrt{\phi g^{11}}, u^1, 0 \right\}. \quad (6.12)$$

and A_f is the optional anti-diffusive flux. Which can be given by $A_f = A_f(f^+, f^-)$. The anti-diffusive flux term for east wall is given in Appendix. (A.6). Note: The above formula is only given for x^1 direction and can be extended to other direction using symmetry. Boundary patching of the faces of the cubed-sphere is done by using the same methodology explained in Section. (5.3).

To evaluate the flux $H_{i+1/2,j}^x$ in Equation. (6.11), eight point-values along the cell walls (as indicated in Figure. 3.4) are required. These values are computed from 2D (piecewise) reconstruction polynomials

$$p_{ij}^n(x, y) \approx u_{ij}^n(x, y), \quad (6.13)$$

subject to the following conservation constraint,

$$\bar{u}_{ij}^n = \frac{1}{\Delta x^1 \Delta x^2} \int_{x_{j-1/2}^2}^{x_{j+1/2}^2} \int_{x_{i-1/2}^1}^{x_{i+1/2}^1} p_{ij}^n(x^1, x^2) dx^1 dx^2. \quad (6.14)$$

where Δ is the width of the individual cell, $\Delta x^1 = (x_{i+1/2}^1 - x_{i-1/2}^1)$ and $\Delta x^2 = (x_{j+1/2}^2 - x_{j-1/2}^2)$, width of the cell in x^1 and x^2 directions respectively. where \bar{u}_{ij}^n is the cell-average at time $t = t^n$, $u_{ij}^n(x^1, x^2) = u(x^1, x^2, t^n)|_{I_{ij}}$. These reconstruction polynomials can be obtained by different approaches. Here, I utilize three techniques using WENO and Kurganov-Liu framework.

6.4 TREATMENT OF DISCRETE DERIVATIVES

The discrete derivatives present in the evaluation of vorticity (ζ) are calculated in equi-angular coordinates using the central differencing methods and are second order accurate since cell-averages only represent a second order approximation to the center value, and it can be given by the following:

$$\left(\frac{\partial u_2}{\partial x^1}\right)_{(i,j)} = \frac{-\bar{u}_{2(i+2,j)} + 8\bar{u}_{2(i+1,j)} - 8\bar{u}_{2(i-1,j)} + \bar{u}_{2(i-2,j)}}{12\Delta}, \quad (6.15)$$

$$\left(\frac{\partial u_1}{\partial x^2}\right)_{(i,j)} = \frac{-\bar{u}_{1(i,j+2)} + 8\bar{u}_{1(i,j+1)} - 8\bar{u}_{1(i,j-1)} + \bar{u}_{1(i,j-2)}}{12\Delta}. \quad (6.16)$$

I use backward and forward differencing method near the boundaries and can be defined by:

$$\left(\frac{\partial u_2}{\partial x^1}\right)_{(i,j)} = \frac{-3\bar{u}_{2(i,j)} + 4\bar{u}_{2(i+1,j)} - \bar{u}_{2(i,j)}}{6\Delta}, \quad (6.17)$$

$$\left(\frac{\partial u_2}{\partial x^1}\right)_{(i,j)} = \frac{3\bar{u}_{2(i,j)} - 4\bar{u}_{2(i-1,j)} + \bar{u}_{2(i,j)}}{6\Delta}. \quad (6.18)$$

where Δ is the width of the individual cell, for example, $\Delta x^1 = (x_{i+1/2}^1 - x_{i-1/2}^1)$, width of the cell in x^1 direction. By using symmetry the Equation. (6.18) can be extended in x^2 direction, I could have used higher order differencing methods here, but I tested the impact on the accuracy, which was very negligent.

6.5 NUMERICAL EXPERIMENTS AND RESULTS

A test suite for the shallow water equations on the cubed-sphere, was proposed by Williamson et al. (see [75]) is considered in this present work to test the performance of the three C-FV schemes.

6.5.1 Steady state geostrophic flow

The first test considered is a steady state geostrophic flow test problem, which has a steady-state solution of the full non-linear SW equations. This test case represents an

Table 6.1: Relative errors in the height field for steady state geostrophic flow ($\alpha = \pi/4$ and $t = 5$ days for KL scheme with a resolution of $40 \times 40 \times 6$ and a CFL of 0.50 is chosen.

N	L_1 error	L_2 error	L_∞ error
20	5.45E-4	6.34E-4	1.20E-3
40	1.29E-4	1.50E-4	2.77E-4
80	3.16E-5	3.69E-5	6.61E-5

Table 6.2: Same as in Table. 6.1 but for WENO-5 scheme.

N	L_1 error	L_2 error	L_∞ error
20	5.83E-4	6.59E-4	1.06E-3
40	1.41E-4	1.59E-4	2.58E-4
80	3.52E-5	4.00E-5	7.40E-5

Table 6.3: Same as in Table. 6.1 but for WENO-35 scheme.

N	L_1 error	L_2 error	L_∞ error
20	7.54E-4	8.56E-4	1.40E-3
40	1.70E-4	1.99E-4	3.31E-4
80	4.08E-5	4.83E-5	8.32E-5

unstable equilibrium solution to the shallow-water equations, this can be used to study the convergence properties of the numerical methods. The wind field is uniform and the equations are geostrophically balanced during the time evolution. So, both the height and flow fields remain same during the simulation. The initial velocity and height fields can be given as follows:

$$\begin{aligned} u &= u_0(\cos \alpha_0 \cos \theta + \sin \alpha_0 \cos \lambda \sin \theta), \\ v &= -u_0 \sin \alpha_0 \sin \lambda, \\ g_r h &= g_r h_0 - \frac{u_0}{2}(2a\omega + u_0)(\sin \theta \cos \alpha_0 - \cos \lambda \cos \theta \sin \alpha_0)^2. \end{aligned}$$

where a is the earth's radius, $u_0 = 2\pi a/(12 \text{ days})$ and $g_r h_0 = 2.94 \times 10^4 m^2 s^{-2}$. Here, I chose alpha $\alpha_0 = \pi/4$, which makes the test more challenging on the cubed-sphere. The cubed-sphere resolution is chosen to be $40 \times 40 \times 6$ (or $N_c = 40$) so that the results can be compared to that of Ullrich et al. [71] schemes. Maximum CFL is set to 0.50. The numerical results of height (error = numerical - analytic) and vorticity fields after 5 model days are given in Figure. (6.2) for KL, WENO-5 and WENO-33 are given in panels (b), (c) and (d) respectively. The normalized ℓ_1 , ℓ_2 and ℓ_∞ errors for the three schemes, KL, WENO-5 and WENO-35 are given in Table. (6.1), (6.2), and (6.3) respectively. The height errors are comparable to the FV schemes given in [71]. WENO-5 scheme produces accurate results than KL and WENO-35 schemes. Increasing order of accuracy can be given in the following way: $\text{WENO-35} < \text{KL} \leq \text{WENO-5}$.

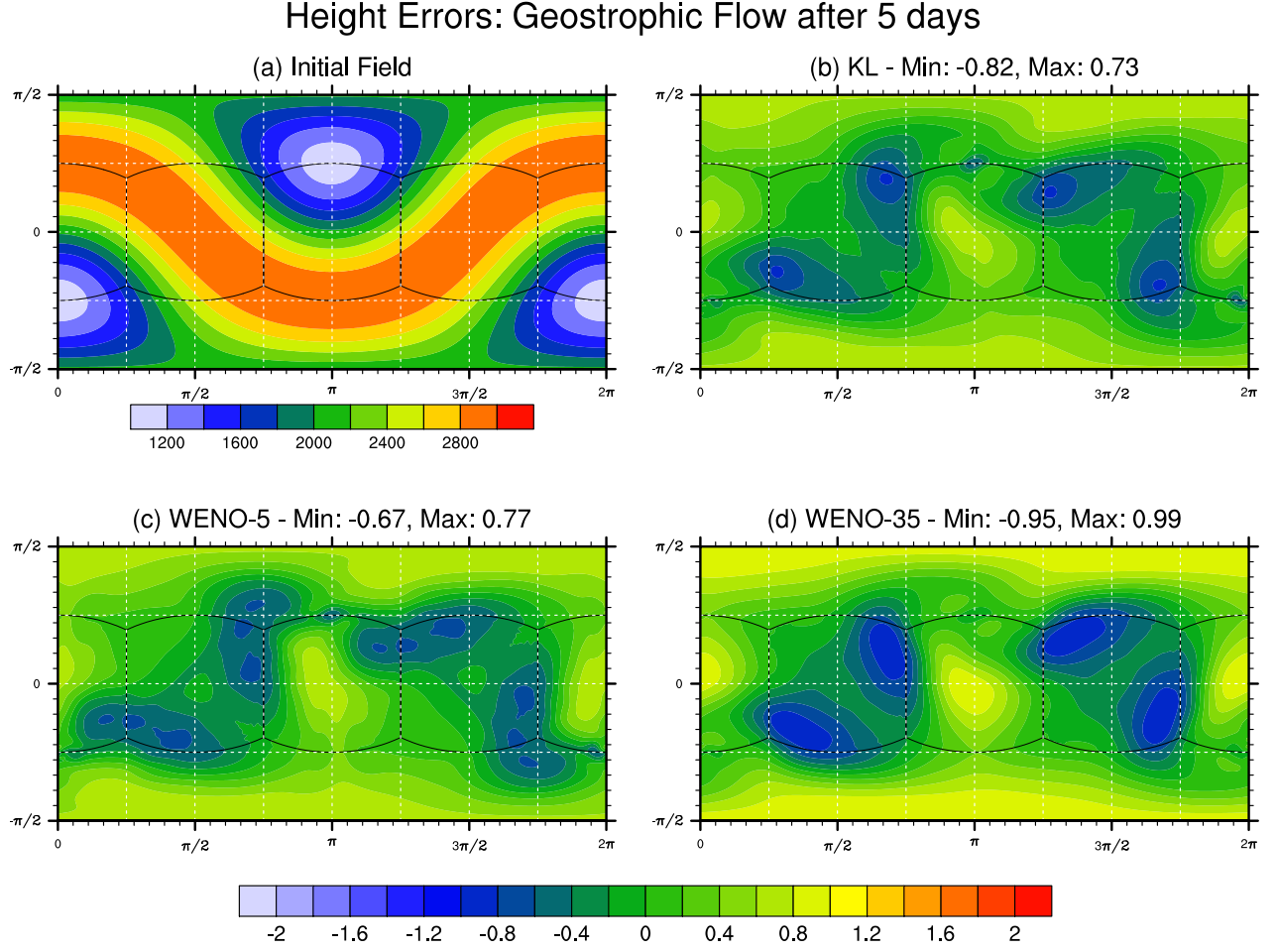


Figure 6.2: Height errors (Numerical - Analytic) after 5 days with steady state geostrophic flow test on $40 \times 40 \times 6$ grid, and a CFL of 0.50 is chosen. (a) Initial height field, (b) KL, (c) WENO-5 and (d) WENO-35. Contour lines for (b), (c), and (d) are plotted from -2.0 to 2.0 with an interval of 0.2 m.

6.5.2 Zonal flow over an isolated mountain

The second test I employed to test the C-FV schemes is test case number 5 in [75], which consists of a zonal flow of a shallow fluid over an isolated mountain. This test case is useful for studying the effectiveness of the numerical scheme in conserving integral invariants such as mass and total energy. The wind and height fields are the same as in Section. (6.5.1), except for the parameters $\alpha_0 = 0$, $h_0 = 5960m$ and $u_0 = 20m/s$. The bottom of the mountain is centered at $(\lambda_c, \theta_c) = (3\pi/2, \pi/6)$, a mountain is introduced into the flow, which can be represented by the following:

$$h_s = h_{s0} (1 - r/r_0),$$

where $h_{s0} = 2000m$, $r_0 = \pi/9$ and $r = \min \left[r_0, \sqrt{(\lambda - \lambda_c)^2 + (\theta - \theta_c)^2} \right]$.

There is no analytic solution available to this test case, so I compare the results of the solution with other results in literature. The Numerical solution of height field and vorticity field is shown in Figure. (6.3) and (6.4 respectively). The simulation is carried out on $40 \times 40 \times 6$ grid, and $CFL = 0.50$ is chosen. From the comparison to other results given in literature, I found that all the three schemes produce accurate results, the KL and WENO-5 schemes preserve the shape better than WENO-35 scheme. The vorticity field after 5 and 15 days is given in Figure. (6.4), produced by KL, WENO-5 and WENO-35 schemes, represented in top, middle and bottom rows respectively. The solution is smooth without any irregularities at edges and corners. The evolution of normalized errors of potential enstrophy and total energy are given in Figure. (6.5), the errors are comparable to the results given in [71, 6, 59]. WENO-5 performs better than WENO-35 scheme in terms of normalized error norms where as it produces almost similar results as KL scheme.

Height Field: Zonal Flow over an Isolated Mountain

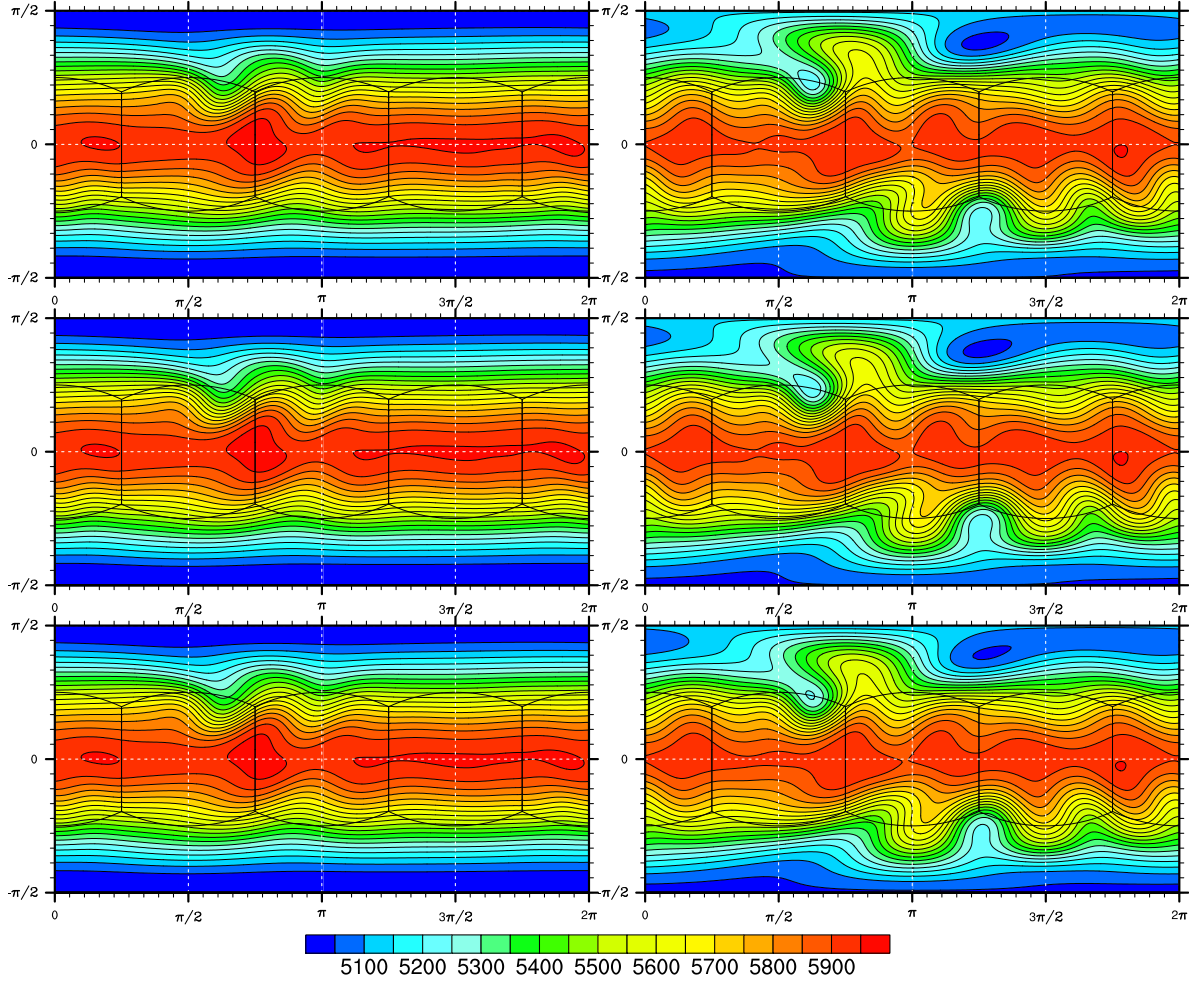


Figure 6.3: Numerical solution for the zonal flow over an isolated mountain test on $40 \times 40 \times 6$ grid and $CFL = 0.50$ with flow angle $\alpha = 0$. Contour levels are from 5050 m to 5950 m in intervals of 50 m. The top, middle and bottom rows represents the solution obtained by KL, WENO-5 and WENO-35 schemes respectively, the left and right columns represents the solution at 5 and 15 days respectively.

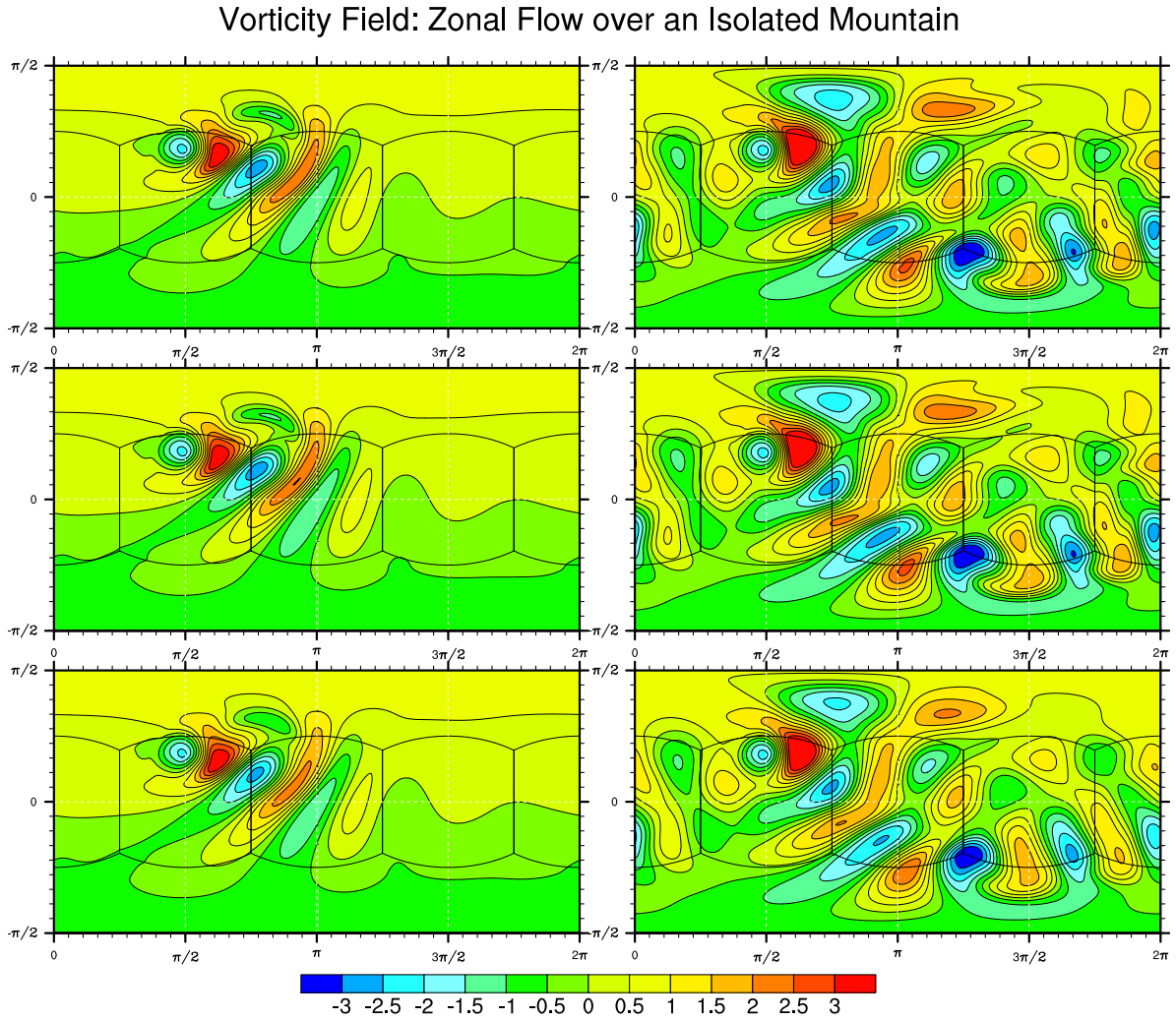


Figure 6.4: Numerical solution of vorticity field for the zonal flow over an isolated mountain test, experiment settings are same as in Figure 6.3. Contour levels are from $(-3 \text{ to } 3 \text{ in intervals of } .50) \times 10^{-5}$. The top, middle and bottom rows represents the solution obtained by KL, WENO-5 and WENO-35 schemes respectively, the left and right columns represents the solution at 5 and 15 days respectively.

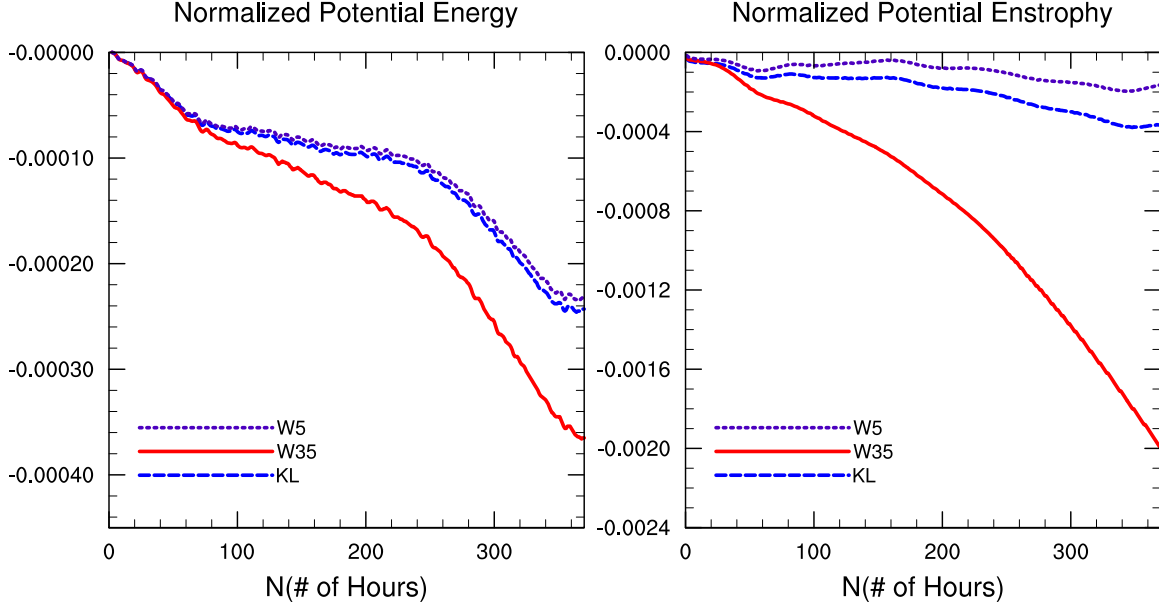


Figure 6.5: All the experiment settings are same as in Figure. 6.3. Evolution of the normalized conservation errors of potential enstrophy (left) and total energy (right).

6.5.3 Rossby-Haurwitz wave

A 4-wave Rossby-Haurwitz wave (test case 6 in [75]) is considered as the third experiment in this present work. The initial state is an exact steadily propagating solution of the non-divergent barotropic vorticity equation. This case is not considered for testing the long-term performance of a numerical model, because it is dynamically unstable, but it still provides a good test bed for short to middle-term simulations. The divergence-free flow field can be given by the following:

$$\psi = -R^2\omega \sin \theta + R^2K \cos^2 \theta \sin \theta \cos r\lambda,$$

the initial field is given by:

$$g_r h = g_r h_0 + R^2 A + R^2 B \cos r\lambda + R^2 C \cos 2r\lambda.$$

Here $\omega = K = 7.848 \times 10^{-6} s^{-1}$ and $r = 4$ are the constants, and A, B, and C are the functions of latitude. Please refer to [75] for complete details for this test case. The

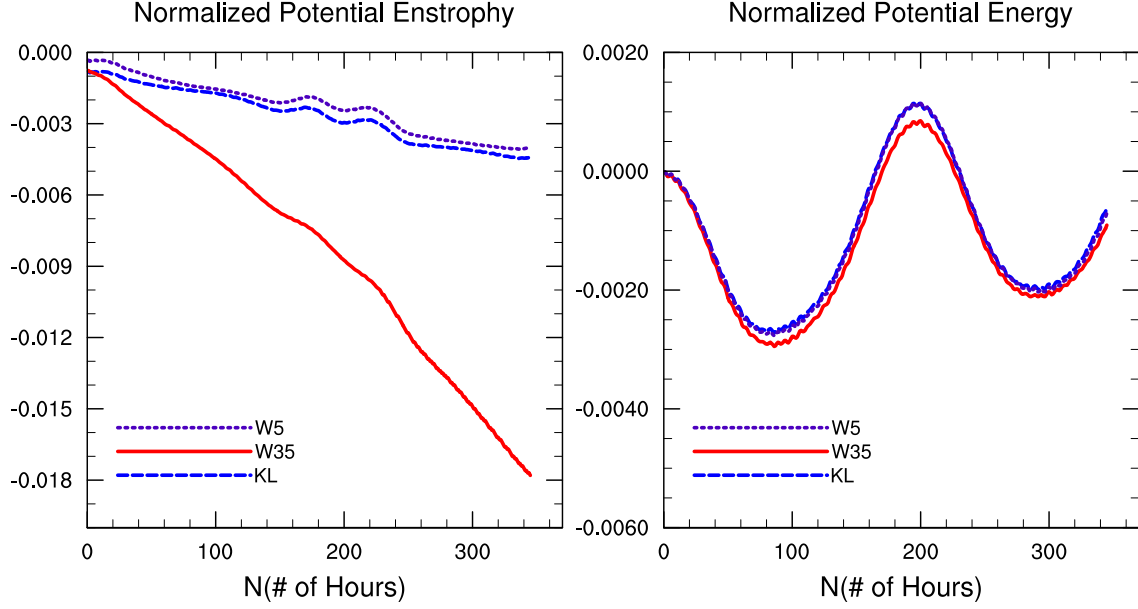


Figure 6.6: All the experiment settings are same as in Figure. 6.7, except the grid resolution is $40 \times 40 \times 6$. Evolution of the normalized conservation errors of potential enstrophy (left) and total energy (right).

Numerical solution of height field is shown in Figure. (6.7). The simulation is carried out on $48 \times 48 \times 6$ grid, and $CFL = 0.50$ is chosen. From the comparison to other results given in literature, I found that all the three schemes produce accurate results. For consistency with the test case 5, I chose a resolution of $40 \times 40 \times 6$ to produce the normalized errors. The evolution of normalized errors of potential enstrophy and total energy are given in Figure. (6.6), the errors are comparable to the results given in [71]. Here again WENO-5 and KL perform better in terms of normalized errors in comparison with WENO-35.

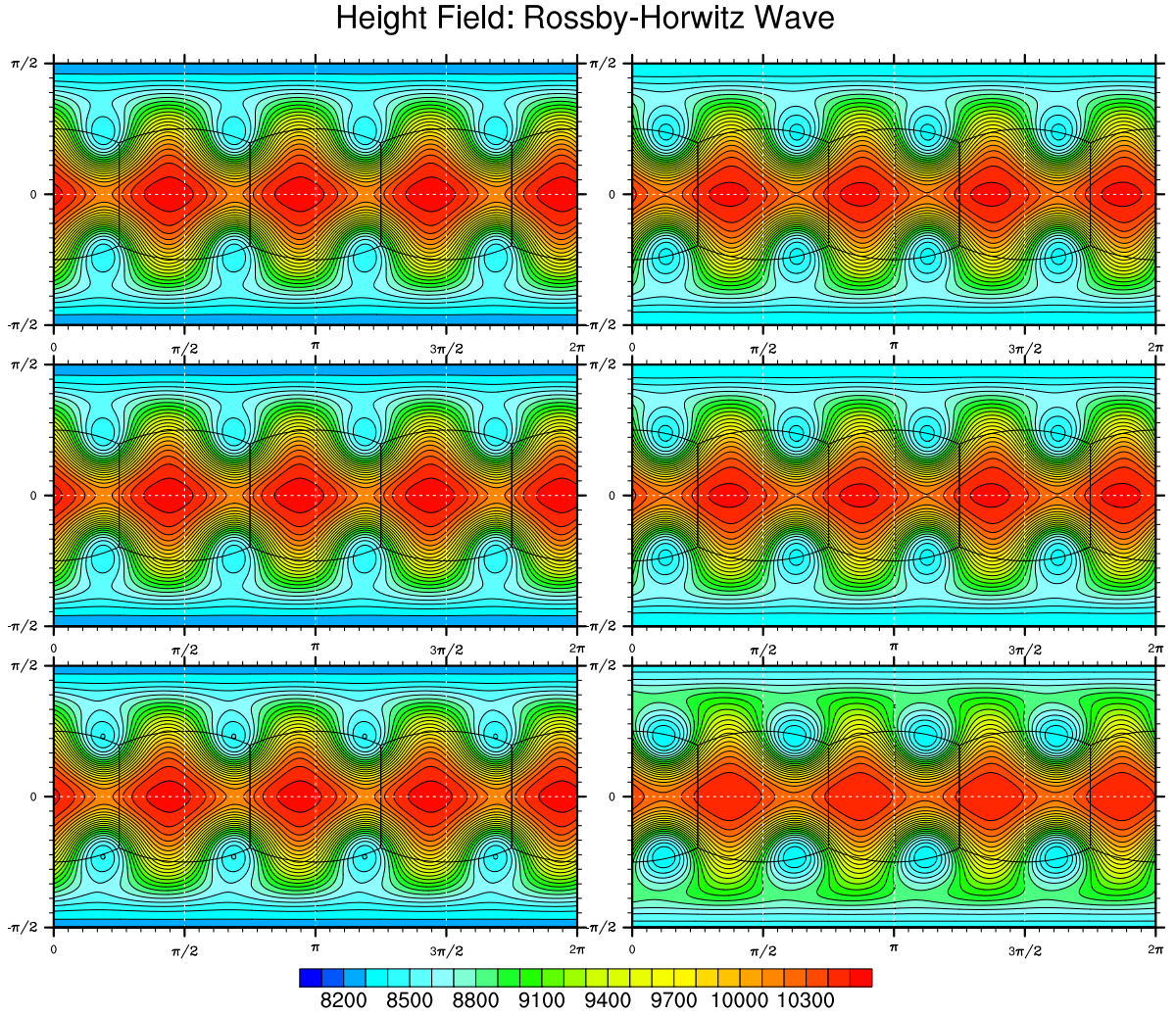


Figure 6.7: Numerical solution for the Rossby-Haurwitz wave test on $48 \times 48 \times 6$ grid and $\text{CFL} = 0.50$ with flow angle $\alpha = 0$. Contour levels are from 8100 m to 10500 m in intervals of 100 m. The top, middle and bottom rows represents the solution obtained by KL, WENO-5 and WENO-35 schemes respectively, the left and right columns represents the solution at 7 and 14 days respectively.

6.6 DISCUSSION AND SUMMARY

I extended the three C-FV (KL, WENO-5 and WENO-35) schemes developed for transport problem to solve shallow water model on a cubed-sphere. From the linear transport problem study it is clear that KP and WENO-33 are least accurate and are computationally expensive out of all the five C-FV schemes, so they are discarded for further analysis using shallow water model. Shallow water model and the discretization details are mentioned.

Three test cases from the standard test suite for shallow water model given in [75] are considered to evaluate the considered schemes. Steady state geostrophic flow, zonal flow over an isolated mountain and Rossby-Haurwitz wave, are the test cases utilized to do the performance study. From the results, the order of accuracy of these three schemes is over second order and falls behind third order. KL and WENO-5 produces similar kind of results which are better than WENO-35, and the error measures are comparable to computationally expensive schemes such as: a fourth-order FV scheme by Ullrich et al. [71], a 7-th order FV scheme by Putman et al. [59], and a FV scheme by Chen et al. [6].

WENO-5, the dimension split scheme performs equivalent to KL scheme, which does not have inbuilt non-oscillatory property, in WENO-5 the non-oscillatory property is ensured by the smoothness indicators and weight factors inbuilt into the scheme. WENO-5 has simple computational stencil which is five cells long in x^1 and x^2 direction, but where as KL computational stencil is complex given in Figure. (3.3), due to this communication cost will be minimal in WENO-5 scheme when implemented in parallel. This makes WENO-5 scheme a better choice than KL to consider for parallel architecture.

Chapter 7

Conclusion and Future Work

7.1 CONCLUSION

Central-upwind finite-volume (C-FV) schemes are a subset of Godunov-type methods for solving hyperbolic conservation laws. Unlike the Godunov-type upwind schemes, C-FV schemes do not involve Riemann solvers or characteristic decomposition, and can be implemented on non-staggered grids. Semi-discrete central schemes are high-order accurate and non-oscillatory, depending on the reconstruction procedure, and these features make them computationally attractive for atmospheric numerical modeling. I consider a semi-discretized central third-order C-FV scheme [30] (Kurganov-Petrova (KP) scheme) for linear transport problems on cubed-sphere. The cubed-sphere geometry is a challenging computational domain for finite-volume (FV) schemes, because of the non-orthogonal curvilinear geometry and grid discontinuities at the edges and corners.

In addition to the KP scheme, four more central schemes based on Weighted Essentially Non-Oscillatory (WENO) reconstruction and Kurganov-Liu (KL) methods were considered. They are, a fully 2D third-order WENO scheme (employing a compact 3×3 computational stencil) WENO-33, and a fifth-order dimension-split WENO (WENO-5) scheme, and the hybrid scheme WENO-35 combining WENO-33, WENO-5 and KL reconstructions. The WENO-based schemes are only “essentially” non-oscillatory, oscillations of small amplitude will still remain in the solution, and in a strict sense these schemes are not positivity preserving. In order to address this issue, a Bound-Preserving (BP) conservative filter was combined with WENO reconstructions, and a positivity-preserving (PP) filter optionally used. I use these filters for KL scheme as well. The BP and PP filters are local and computationally inexpensive. Time integration is performed with a third-order Runge-

Kutta method for KP and WENO-33 schemes and a fourth-order Runge-Kutta method for WENO-5, WENO-35 and KL schemes.

To validate and verify the resulting non-oscillatory central schemes, a variety of benchmark tests were performed on both 2D Cartesian plane and cubed-sphere. The tests are based on solid-body rotation and deformational flow. For convergence study a smooth solid-body rotation test is used, the computed order of accuracy ranges from second- to fourth-order, depending on the scheme. The BP and PP filter successfully eliminates oscillations and strictly preserves the positivity of the solution. The WENO-5 and KL schemes produce more accurate results than KP, WENO-35 and WENO-33 schemes. The order of accuracy, in increasing manner, for each scheme can be stated as $KP < WENO-33 < WENO-35 < WENO-5 \cong KL$.

The advection tests on the sphere includes solid-body rotation of a cosine-bell and moving (deforming) vortices. These two tests are quasi-smooth, all the error norms show that WENO-based and KL schemes performs much better than KP scheme. In addition, a new challenging deformational flow test was also used to assess the performance of the non-oscillatory scheme in the presence of discontinuities. For this test non-smooth (slotted-cylinders) and quasi-smooth (cosine-bells) initial data have been used. The BP and PP filter combination performed very well, as in the Cartesian case. In general, the performance of WENO-5, KL and WENO-35 stand out as compared to the KP and WENO-33 schemes. The execution time was roughly calculated using KP scheme as a basic reference, and it shows that WENO-5 and KL schemes takes less time to compute and produces more accurate results than all other schemes. The error norms suggest that the results with spherical WENO-5, KL and WENO-35 comparable to those published with recent high-order (global) FV schemes.

It is a bit surprising to see that the dimension-split WENO-5 scheme performs better than other fully 2D central schemes considered here. However it is not clear whether WENO-5 can perform better than a fully 2D scheme for non-linear problems. So, to assess the proposed schemes for a non-linear case, I extended them to solve a continuous flux form

non-linear shallow water model on the cubed-sphere geometry. Here I only considered three most accurate schemes out of all the C-FV. The schemes that are considered for shallow water model are WENO-35, WENO-5 and KL. Various benchmark tests are considered to test the performance of these schemes, three tests are considered, that are from Williamson test suite, that include, steady state geostrophic flow, zonal flow over an isolated mountain, and Rossby-Hauritz wave test cases. It can be concluded from the results that KL and WENO-5 produced similar kind of results, which are better than the results attained by WENO-35 scheme. The dimension-split scheme WENO-5 produced similar results as KL scheme, which is a fully 2D central scheme for a non-linear case as well. WENO-5 has simple computational stencil when compared to KL scheme, due to this communication cost will be minimal in WENO-5 scheme when implemented in parallel. WENO-5 is very simple in terms of implementation than KL scheme. This makes WENO-5 scheme a better choice than KL to consider for future atmospheric models. Further testing should be done in to support this statement. The error norms for WENO-5 and KL schemes are comparable to other results published with high-order schemes.

The work presented here can also be found in [25], and [24].

7.2 FUTURE WORK

Firstly, I wish to extend the considered schemes to solve the 2D compressible Euler system, I am in the process of completing this work and intend to submit it to the conference proceedings on Scientific Computing and Applications [48]. And can also be extended to a 3D atmospheric core, The shallow water equations can be modified to create a stratified 3D model, using pressure as the vertical component. The atmosphere is vertically subdivided into a finite number of layers of pressure with thickness and is treated as a stack of shallow water systems. The equations governing potential temperature and moisture will also be included in conjunction to thickness, vorticity, and divergence. The performance of the 3D model can be tested using the test suite for dynamical cores mentioned in the literature.

Secondly, I wish to parallelize the code using MPI and OpenMP, and test the scal-

ability and performance of the proposed schemes on a cubed-sphere grid geometry, and then testing the performance on multi-GPUs will be next task. Future work also consists incorporating the schemes considered here in High-Order Method Modeling Environment (HOMME) framework. HOMME, a dynamical cores component, has been integrated into the Community Atmospheric Model (CAM), which is the atmospheric component of the Community Earth System Model (CESM). CESM is a fully coupled, global climate model that provides state-of-the-art computer simulations of the Earth's past, present, and future climate states. CESM is composed of five separate models simultaneously simulating the Earth's atmosphere, ocean, land, land-ice, and sea-ice, plus one central coupler component [<http://www.cesm.ucar.edu>]. The CESM system can be configured a number of different ways from both a science and technical perspective. CESM supports several different resolutions and component configurations. In addition, each model component has input options to configure specific model physics and parameterizations.

References

- [1] K. Adamy, B. Bousquet, S. Faure, J. Lammie, and R. Temam. A multilevel method for finite volume discretization of the two-dimensional nonlinear shallow-water equations. *Ocean Modelling*, 33:235–256, 2010.
- [2] A. Arakawa and V. R. Lamb. A potential enstrophy and energy conserving scheme for the shallow water equations. *Monthly Weather Review*, 109:18–36, 1981.
- [3] P. N. Blossey and D. R. Durran. Selective monotonicity preservation in scalar advection. *J. Comput. Phys.*, 227:5160–5183, May 2008.
- [4] S. Byron and D. Levy. On the total variation of high-order semi-discrete central schemes for conservation laws. *J. of Sci. Comput.*, 22:163–175, 2006.
- [5] Y. Chao, C. Jianwen, and C. Xiao-Chuan. A fully implicit domain decomposition algorithm for shallow water equations on the cubed-sphere. *SIAM Journal on Scientific Computing*, 32(1):418–438, 2010.
- [6] C. Chen and F. Xiao. Shallow water model on cubed-sphere by multi-moment finite volume method. *J. Comput. Phys.*, 227:5019–5044, 2008.
- [7] V. Cheruvu, R. D. Nair, and H. M. Tufo. A spectral finite volume transport scheme on the cubed-sphere. *Appl. Num. Math.*, 57:1021–1032, 2007.
- [8] B. Choi, M. Iskandarani, J. Levin, and D. B. Haidvogel. A spectral finite-volume method for the shallow water equations. *Monthly Weather Review*, 132(7):1777–1791, 2012/06/29 2004.
- [9] B. Cockburn and C-W. Shu. The Runge-Kutta discontinuous Galerkin method for convection-dominated problems. *J. Sci. Computing*, 16:173–261, 2001.

- [10] P. Colella and P. R. Woodward. The Piecewise Parabolic Method (PPM) for gas-dynamical simulations. *J. Comput. Phys.*, 54:174–201, 1984.
- [11] W. D. Collins, P. J. Rasch, B. A. Boville, J. J. Hack, J. R. McCaa, D. L. Williamson, B. P. Briegleb, C. M. Bitz, S.-J. Lin, M. Zhang, and Y. Dai. The formulation and atmospheric simulation of the Community Atmosphere Model: CAM3. *J. Climate*, 19:2144–2161, 2006.
- [12] J. Dennis, R. D. Nair, H. M. Tufo, M. Levy, and T. Voran. Development of a scalable global discontinuous Galerkin atmospheric model. *Int. J. Comput. Science and Engineering*, 2006. To appear.
- [13] L. Doron, P. Gabriella, and R. Giovanni. Compact central weno schemes for multidimensional conservation laws. *SIAM J. Sci. Comput.*, 22:656–672, February 2000.
- [14] D. R. Durran. *Numerical Methods for Wave Equations in Geophysical Fluid Dynamics*. Springer, 1999. ISBN 0-387-98376-7, 465 pp.
- [15] K. O. Friedrichs. Symmetric hyperbolic linear differential equations. *Communications on Pure and Applied Mathematics*, 7(2):345–392, 1954.
- [16] K. O. Godunov. A difference scheme for numerical solution of discontinuous solution of hydrodynamic equations. *Math. Sbornik*, 47:271–306, 1959.
- [17] S. Gottlieb, C.-W. Shu, and E. Tadmor. Strong Stability-Preserving high-order time discretization methods. *SIAM Review*, 43(1):89–112, 2001.
- [18] A. Harten. On the symmetric form of systems of conservation laws with entropy. *Journal of Computational Physics*, 49(1):151 – 164, 1983.
- [19] A. Harten, B. Engquist, S. Osher, and S. R. Chakravarthy. Uniformly high order accurate essentially non-oscillatory schemes, 111. *J. Comput. Phys.*, 71:231–303, August 1987.

- [20] M. Iskandarani, J.C. Levin, B.-J. Choi, and D.B. Haidvogel. Comparison of advection schemes for high-order hp finite element and finite volume methods. *Ocean Modelling*, 10(1–2):233 – 252, 2005. *The Second International Workshop on Unstructured Mesh Numerical Modelling of Coastal, Shelf and Ocean Flows*.
- [21] R. Jakob-Chien, J. J. Hack, and D. L. Williamson. Spectral transform solutions to the shallow water test set. *J. Comput. Phys.*, 119:164–187, 1995.
- [22] G-S. Jiang and C-W. Shu. Efficient implementation of weighted eno schemes. *J. Comput. Phys.*, 126:202–228, June 1996.
- [23] G. Karniadakis. Spectral/hp element methods for computational fluid dynamics.
- [24] K. Katta, R. D. Nair, and V. Kumar. High-order central finite-volume schemes for shallow water model on the cubed-sphere. *J. Comput. Phys.*, In Prep.
- [25] K. Katta, R. D. Nair, and V. Kumar. High-order central finite-volume schemes for linear transport problems on the cubed-sphere. Submitted.
- [26] A. Kurganov and L. Doron. A third-order semidiscrete central scheme for conservation laws and convection-diffusion equations. *SIAM J. Sci. Comput.*, 22:1461 – 1468, 2000.
- [27] A. Kurganov and C. T. Lin. On the reduction of numerical dissipation in central-upwind schemes. *COMMUNICATIONS IN COMPUTATIONAL PHYSICS*, 2:141–163, February 2007.
- [28] A. Kurganov and Y. Liu. New adaptive artificial viscosity method for hyperbolic systems of conservation laws. *Journal of Computational Physics*, 2012.
- [29] A. Kurganov, S. Noelle, and G. Petrova. Semidiscrete central-upwind schemes for hyperbolic conservation laws and hamilton–jacobi equations. *SIAM J. Sci. Comput.*, 23(3):707–740, March 2001.

- [30] A. Kurganov and G. Petrova. A third-order semi-discrete genuinely multidimensional central scheme for hyperbolic conservation laws and related problems. *Numerische Mathematik*, 88:683–729, 2001.
- [31] A. Kurganov and E. Tadmor. New high-resolution central schemes for nonlinear conservation laws and convection-diffusion equations. *J. Comput. Phys.*, 160:241–282, May 2000.
- [32] P. H. Lauritzen, R. D. Nair, and P. A. Ullrich. A conservative semi-Lagrangian multi-tracer transport scheme (CSLAM) on the cubed-sphere grid. *J. Comput. Phys.*, 229:1401–1424, 2010.
- [33] P. H. Lauritzen, P. A. Ullrich, and R. D. Nair. Atmospheric transport schemes: Desirable properties and a semi-lagrangian view on finite-volume discretizations. In P.H. Lauritzen, C. Jablonowski, M. Taylor, and R.D Nair, editors, *Numerical Techniques for Global Atmospheric Models, Lecture Notes in Computational Science and Engineering, Vol.80*, pages 185–250. Springer, 2011.
- [34] P.H. Lauritzen, C. Jablonowski, M.A. Taylor, and R.D. Nair. *Numerical Techniques for Global Atmospheric Models*. Lecture Notes in Computational Science and Engineering. Springer, 2011.
- [35] P. D. Lax. Weak solutions of nonlinear hyperbolic equations and their numerical computation. *Communications on Pure and Applied Mathematics*, 7(1):159–193, 1954.
- [36] R. J. LeVeque. Finite volume methods for hyperbolic problems. *Cambridge University Press*, 2002.
- [37] M. N. Levy, R. D. Nair, and H. M. Tufo. High-order Galerkin method for scalable global atmospheric models. *Computers and Geoscience*, 33:1022–1035, 2007.
- [38] XD. Liu, S. Osher, and T. Chen. Weighted essentially non-oscillatory schemes. *J. Comput. Phys.*, 115:200–212, 1994.

- [39] XD. Liu and E. Tadmor. Third order non-oscillatory central scheme for hyperbolic conservation laws. *Numer. Math.*, 79:397–425, 1998.
- [40] P. Lynch. *The Emergence of Numerical Weather Prediction*. Cambridge University Press, 2006.
- [41] P. Lynch. The origins of computer weather prediction and climate modeling. *J. Comput. Phys.*, 227(7):3431–3444, March 2008.
- [42] P. F. Fischer M. O. Deville and E. H. Mund. *High-Order Methods for Incompressible Fluid Flow*. Cambridge University Press, 2002.
- [43] B. Machenhauer, E. Kaas, and P.H. Lauritzen. *Special Volume on Computational Methods for the Ocean and Atmosphere*, volume 14, chapter Finite Volume Methods in Meteorology, pages 3–120. Elsevier, 2009. ISBN-13: 978-0-444-51893-4.
- [44] S. Moorthi, R. W. Higgins, and J. R. Bates. A global multilevel atmospheric model using a vector semi-lagrangian finite-difference scheme. part ii: Version with physics. *Monthly Weather Review*, 123(5):1523–1541, 2012/06/29 1995.
- [45] R. D. Nair. Diffusion experiments with a global discontinuous Galerkin shallow water model. *Mon. Wea. Rev.*, 139:In Pres, 2009.
- [46] R. D. Nair, H.-W. Choi, and H. M. Tufo. Computational aspects of a scalable high-order discontinuous Galerkin atmospheric dynamical core. *Computers and Fluids*, 38:309–319, 2009.
- [47] R. D. Nair and C. Jablonowski. Moving vortices on the sphere: A test case for horizontal advection problems. *Mon. Wea. Rev.*, 136:699–711, 2008.
- [48] R. D. Nair and K. Katta. High-order central finite-volume schemes for 2d euler system on the cubed-sphere. *The 8th International Conference on Scientific Computing and Applications.*, In Prep.

- [49] R. D. Nair and P. H. Lauritzen. A class of deformational flow test cases for linear transport problems on the sphere. *J. Comput. Phys.*, 229:8868–8887, 2010.
- [50] R. D. Nair, M. N. Levy, and P. H. Lauritzen. Emerging numerical methods for atmospheric modeling. In P.H. Lauritzen, C. Jablonowski, M. Taylor, and R.D Nair, editors, *Numerical Techniques for Global Atmospheric Models, Lecture Notes in Computational Science and Engineering, Vol.80*, pages 251–311. Springer, 2011.
- [51] R. D. Nair, S.J. Thomas, and R.D. Loft. A Discontinuous Galerkin global shallow water model. *Mon. Wea. Rev.*, 133:876–888, 2005.
- [52] R. D. Nair, S.J. Thomas, and R.D. Loft. A Discontinuous Galerkin transport scheme on the cubed sphere. *Mon. Wea. Rev.*, 133:814–828, 2005.
- [53] R. D. Nair and H. M. Tufo. Petascale atmospheric general circulation models. *Journal of Physics: Conference Series*, 78(1):012078, 2007.
- [54] H. Nessyahu and E. Tadmor. Non-oscillatory central differencing for hyperbolic conservation laws. *J. Comput. Phys.*, 87:408–463, April 1990.
- [55] M. R. Norman, R. D. Nair, and F. H. M. Semazzi. A low communication and large time step explicit finite-volume solver for non-hydrostatic atmospheric dynamics. *J. Comput. Phys.*, 230:1567–1584, 2011.
- [56] M. R. Norman, F. H. M. Semazzi, and R. D. Nair. Conservative cascade interpolation on the sphere: An intercomparison of various non-oscillatory reconstructions. *Q. J. R. Meteorol. Soc.*, 135:795–805, 2009.
- [57] J. Pedlosky. *Geophysical Fluid Dynamics*. Springer-Verlag, 1987. , 710 pp.
- [58] X. Peng, F. Xiao, and K. Takahashi. Conservative constraint for a quasi-uniform overset grid on the sphere. *Quart. J. Roy. Meteor. Soc.*, 132:979–996, 2006.

- [59] W. M. Putman and S. J. Lin. Finite-volume transport on various cubed-sphere grids. *J. Comput. Phys.*, 227:55–78, November 2007.
- [60] W. M. Putman and S.-J. Lin. A Finite-Volume Dynamical Core on the Cubed-Sphere Grid. In N. V. Pogorelov, E. Audit, P. Colella, & G. P. Zank, editor, *Numerical Modeling of Space Plasma Flows: ASTRONUM-2008*, volume 406 of *Astronomical Society of the Pacific Conference Series*, pages 268–+, 2009.
- [61] M. Rančić, R.J. Purser, and F. Mesinger. A global shallow water model using an expanded spherical cube. *Q. J. R. Meteorol. Soc.*, 122:959–982, 1996.
- [62] C. Ronchi, R. Iacono, and P. S. Paolucci. The “cubed sphere”: A new method for the solution of partial differential equations in spherical geometry. *J. Comput. Phys.*, 124(1):93–114, March 1996.
- [63] R. Sadourny. Conservative finite-difference approximations of the primitive equations on quasi-uniform spherical grids. *Mon. Wea. Rev.*, 100:136–144, 1972.
- [64] C.-W. Shu. Essentially non-oscillatory and Weighed essentially non-oscillatory schemes for hyperbolic conservation laws. In *Lecture Notes in Mathematics*, volume 1697, pages 325–432. Springer, 1997.
- [65] PK. Smolarkiewicz. Comment on “a positive definite advection scheme obtained by nonlinear renormalization of the advective fluxes”. *Mon. Wea. Rev.*, 117:2626–2632, 1989.
- [66] R. J. Spiteri and S. J. Ruuth. A new class of optimal high-order strong-stability-preserving time discretization methods. *SIAM J. Numer. Anal.*, 40:469–491, February 2002.
- [67] M. Taylor, J. Edwards, S. Thomas, and R. Nair. A mass and energy conserving spectral element atmospheric dynamical core on the cubed-sphere. *Journal of Physics: Conference Series*, 78, 2007. doi:10.1088/1742-6596/78/1/012074.

- [68] M. Taylor, J. Tribbia, and M. Iskandarani. The spectral element method for the shallow water equations on the sphere. *J. Comput. Phys.*, 130:92–108, 1997.
- [69] J. Thuburn. A PV-based shallow water model on a hexagonal-icosahedral grid. *Mon. Wea. Rev.*, 125:2328–2347, 1997.
- [70] E. F. Toro. *Riemann Solvers and Numerical Methods for Fluid Dynamics. A Practical Introduction (2nd Ed.)*. Springer-Verlag, New York, 1999.
- [71] P. A. Ullrich, C. Jablonowski, and B. van Leer. High-order finite-volume methods for the shallow-water equations on the sphere. *J. Comput. Phys.*, 229:6104–6134, August 2010.
- [72] G. K. Vallis. *Atmospheric and Oceanic Fluid Dynamics*. Cambridge University Press, Cambridge, U.K., 2006.
- [73] B. van Leer. Towards the ultimate conservative difference scheme. II. Monotonicity and conservation combined in a second-order scheme. *J. Comput. Phys.*, 14:361–370, 1974.
- [74] Z.J. Wang. Spectral (finite) volume method for conservation laws on unstructured grids. basic formulation: Basic formulation. *Journal of Computational Physics*, 178(1):210 – 251, 2002.
- [75] D. L. Williamson, J. B. Drake, J. J. Hack, R. Jakob, and P. N. Swarztrauber. A standard test set for numerical approximations to the shallow water equations in spherical geometry. *J. Comput. Phys.*, 102:211–224, 1992.
- [76] C. Yang and X. Cai. Parallel multilevel methods for implicit solution of shallow water equations with nonsmooth topography on the cubed-sphere. *J. Comput. Phys.*, 230:2523–2539, 2011.

- [77] X. Zhang and C.-W. Shu. On maximum-principle-satisfying high order schemes for scalar conservation laws. *J. Comput. Phys.*, 229:3091–3120, 2010.
- [78] Y. Zhang and R D. Nair. A non-oscillatory discontinuous Galerkin transport scheme on the cubed-sphere. *Submitted*, 2011.

Appendix A

Reconstruction and Other Details

A.1 2D SEMI-DISCRETE C-FV SCHEME RECONSTRUCTION DETAILS

The basic parabolas $q_{i,j}^n(x, y)$ are given as following:

$$q_{i,j}^n(x, y) = \left(\bar{u}_{i,j}^n - \frac{(\Delta x)^2}{24} D_+^x D_-^x \bar{u}_{i,j}^n - \frac{(\Delta y)^2}{24} D_+^y D_-^y \bar{u}_{i,j}^n \right) + D_0^x \bar{u}_{i,j}^n (x - x_j) + D_0^y \bar{u}_{i,j}^n (y - y_k) + \frac{1}{2} D_+^x D_-^x \bar{u}_{i,j}^n (x - x_j)^2 + \frac{1}{2} D_+^y D_-^y \bar{u}_{i,j}^n (y - y_k)^2 + D_0^x D_0^y \bar{u}_{i,j}^n (x - x_j) (y - y_k)$$

where:

$$\begin{aligned} D_{\pm}^x v(x, y) &= \pm \frac{v(x \pm \Delta x, y) - v(x, y)}{\Delta x}, \\ D_{\pm}^y v(x, y) &= \pm \frac{v(x, y \pm \Delta y) - v(x, y)}{\Delta y}, \\ D_0^x v(x, y) &= \frac{v(x + \Delta x, y) - v(x - \Delta x, y)}{2\Delta x}, \\ D_0^y v(x, y) &= \frac{v(x, y + \Delta y) - v(x, y - \Delta y)}{2\Delta y}. \end{aligned}$$

The slopes are given by:

$$s_{i,j}^x = \minmod \left(\frac{\bar{u}_{i,j}^n - \bar{u}_{i-1,j}^n}{\Delta x}, \frac{\bar{u}_{i+1,j}^n - \bar{u}_{i,j}^n}{\Delta x} \right), \quad s_{i,j}^y = \minmod \left(\frac{\bar{u}_{i,j}^n - \bar{u}_{i,j-1}^n}{\Delta y}, \frac{\bar{u}_{i,j+1}^n - \bar{u}_{i,j}^n}{\Delta y} \right).$$

The computation of diagonal point values ensures there are no oscillations in the diagonal direction, and also ensures there is no loss of dissipation in the diagonal direction unlike the conventional FV methods. The reconstruction is given by the piecewise polynomial function in the following expression:

$$\hat{p}_{i,j}^n(x, y) = (1 - \hat{q}_{i,j}^n) \hat{L}_{ij}^n(x, y) + \hat{\theta}_{i,j}^n \hat{q}_{i,j}^n(x, y), \quad 0 < \hat{\theta}_{i,j}^n < 1. \quad (\text{A.1})$$

The basic parabolas for the diagonal directions are given by:

$$\begin{aligned}\hat{q}_{i,j}^n(x,y) = & \left(\bar{u}_{i,j}^n - \frac{(\Delta)^2}{48} D_+^{d+} D_-^{d+} \bar{u}_{i,j}^n - \frac{(\Delta)^2}{48} D_+^{d-} D_-^{d-} \bar{u}_{i,j}^n \right), \\ & + D_0^{d+} \bar{u}_{i,j}^n \left(\frac{\Delta}{2\Delta_y} (y - y_i) + \frac{\Delta}{2\Delta_x} (x - x_i) \right), \\ & + D_0^{d-} \bar{u}_{i,j}^n \left(\frac{\Delta}{2\Delta_y} (y - y_j) - \frac{\Delta}{2\Delta_x} (x - x_i) \right), \\ & + D_0^{d+} D_0^{d-} \bar{u}_{i,j}^n \left(\frac{\Delta^2}{4(\Delta_y)^2} (y - y_j)^2 - \frac{\Delta^2}{4(\Delta_x)^2} (x - x_i)^2 \right), \\ & + \frac{1}{2} D_+^{d+} D_-^{d+} \bar{u}_{i,j}^n \left(\frac{\Delta}{2\Delta_y} (y - y_j) + \frac{\Delta}{2\Delta_x} (x - x_i) \right)^2, \\ & + \frac{1}{2} D_+^{d-} D_-^{d-} \bar{u}_{i,j}^n \left(\frac{\Delta}{2\Delta_y} (y - y_j) - \frac{\Delta}{2\Delta_x} (x - x_i) \right)^2.\end{aligned}$$

where

$$\Delta = \sqrt{(\Delta_x)^2 + (\Delta_y)^2}$$

and the divided differences for the diagonal directions are given by:

$$\begin{aligned}D_{\pm}^{d+} v(x,y) &= \pm \frac{v(x \pm \Delta x, y \pm \Delta y) - v(x,y)}{\Delta}, \\ D_{\pm}^{d-} v(x,y) &= \pm \frac{v(x \mp \Delta x, y \pm \Delta y) - v(x,y)}{\Delta}, \\ D_0^{d+} v(x,y) &= \frac{v(x + \Delta x, y + \Delta y) - v(x - \Delta x, y - \Delta y)}{2\Delta}, \\ D_0^y v(x,y) &= \frac{v(x - \Delta x, y + \Delta y) - v(x + \Delta x, y - \Delta y)}{2\Delta}.\end{aligned}$$

The linear functions for the diagonal directions are given by:

$$\hat{L}_{i,j}^n(x,y) = \hat{u}_{i,j}^n + \hat{s}_{i,j}^+ \left[\frac{\Delta}{2\Delta_y} (y - y_j) + \frac{\Delta}{2\Delta_x} (x - x_i) \right] + \hat{s}_{i,j}^- \left[\frac{\Delta}{2\Delta_y} (y - y_j) - \frac{\Delta}{2\Delta_x} (x - x_i) \right]$$

The slopes in the diagonal direction are given by:

$$\hat{s}_{i,j}^+ = \minmod \left(\frac{\bar{u}_{i,j}^n - \bar{u}_{i-1,j-1}^n}{\Delta}, \frac{\bar{u}_{i+1,j+1}^n - \bar{u}_{i,j}^n}{\Delta} \right), \quad \hat{s}_{i,j}^- = \minmod \left(\frac{\bar{u}_{i,j}^n - \bar{u}_{i+1,j+1}^n}{\Delta}, \frac{\bar{u}_{i-1,j+1}^n - \bar{u}_{i,j}^n}{\Delta} \right).$$

where $\hat{\theta}_{i,j}^n = \min\{\hat{\theta}_{i,j}^+, \hat{\theta}_{i,j}^-\}$

$$\theta_{i,j}^\pm = \begin{cases} \min \left\{ \frac{M_{i\pm\frac{1}{2},j\pm\frac{1}{2}}^\pm - \hat{L}_{i,j}^n(x_{i\pm\frac{1}{2}}, y_{j\pm\frac{1}{2}})}{M_{i,j}^\pm - \hat{L}_i^n(x_{i\pm\frac{1}{2}}, y_{j\pm\frac{1}{2}})}, \frac{m_{i\mp\frac{1}{2},j-\frac{1}{2}}^\pm - \hat{L}_{i,j}^n(x_{i\mp\frac{1}{2}}, y_{j-\frac{1}{2}})}{m_{i,j}^\pm - \hat{L}_{i,j}^n(x_{i\mp\frac{1}{2}}, y_{j-\frac{1}{2}})}, 1 \right\} & \text{if } \bar{u}_{i\mp 1,j-1}^n < \bar{u}_{i,j}^n < \bar{u}_{i\pm 1,j+1}^n, \\ \min \left\{ \frac{M_{i\mp\frac{1}{2},j-\frac{1}{2}}^\pm - \hat{L}_{i,j}^n(x_{i\mp\frac{1}{2}}, y_{j-\frac{1}{2}})}{M_{i,j}^\pm - \hat{L}_i^n(x_{i\mp\frac{1}{2}}, y_{j-\frac{1}{2}})}, \frac{m_{i\pm\frac{1}{2},j+\frac{1}{2}}^\pm - \hat{L}_{i,j}^n(x_{i\pm\frac{1}{2}}, y_{j+\frac{1}{2}})}{m_{i,j}^\pm - \hat{L}_{i,j}^n(x_{i\pm\frac{1}{2}}, y_{j+\frac{1}{2}})}, 1 \right\} & \text{if } \bar{u}_{i\mp 1,j-1}^n > \bar{u}_{i,j}^n > \bar{u}_{i\pm 1,j+1}^n, \\ 1 & \text{otherwise,} \end{cases} \quad (\text{A.2})$$

where

$$\begin{aligned} M_{i,j}^\pm &= \max \left\{ \hat{q}_{i,j}^n(x_{i\pm\frac{1}{2}}, y_{j\pm\frac{1}{2}}), \hat{q}_{i,j}^n(x_{i\mp\frac{1}{2}}, y_{j-\frac{1}{2}}) \right\}, \\ m_{i,j}^\pm &= \min \left\{ \hat{q}_{i,j}^n(x_{i\pm\frac{1}{2}}, y_{j\pm\frac{1}{2}}), \hat{q}_{i,j}^n(x_{i\mp\frac{1}{2}}, y_{j-\frac{1}{2}}) \right\}, \\ M_{i\pm\frac{1}{2},j\pm\frac{1}{2}}^+ &= \max \left\{ \frac{1}{2} \left(\hat{L}_{i,j}^n(x_{i\pm\frac{1}{2}}, y_{j\pm\frac{1}{2}}) + \hat{L}_{i\pm 1,j\pm 1}^n(x_{i\pm\frac{1}{2}}, y_{j\pm\frac{1}{2}}) \right), \hat{q}_{i\pm 1,j\pm 1}^n(x_{i\pm\frac{1}{2}}, y_{j\pm\frac{1}{2}}) \right\}, \\ M_{i\mp\frac{1}{2},j\pm\frac{1}{2}}^- &= \max \left\{ \frac{1}{2} \left(\hat{L}_{i,j}^n(x_{i\mp\frac{1}{2}}, y_{j\pm\frac{1}{2}}) + \hat{L}_{i\mp 1,j\pm 1}^n(x_{i\mp\frac{1}{2}}, y_{j\pm\frac{1}{2}}) \right), \hat{q}_{i\mp 1,j\pm 1}^n(x_{i\mp\frac{1}{2}}, y_{j\pm\frac{1}{2}}) \right\}, \\ m_{i\pm\frac{1}{2},j\pm\frac{1}{2}}^+ &= \min \left\{ \frac{1}{2} \left(\hat{L}_{i,j}^n(x_{i\pm\frac{1}{2}}, y_{j\pm\frac{1}{2}}) + \hat{L}_{i\pm 1,j\pm 1}^n(x_{i\pm\frac{1}{2}}, y_{j\pm\frac{1}{2}}) \right), \hat{q}_{i\pm 1,j\pm 1}^n(x_{i\pm\frac{1}{2}}, y_{j\pm\frac{1}{2}}) \right\}, \\ m_{i\mp\frac{1}{2},j\pm\frac{1}{2}}^- &= \min \left\{ \frac{1}{2} \left(\hat{L}_{i,j}^n(x_{i\mp\frac{1}{2}}, y_{j\pm\frac{1}{2}}) + \hat{L}_{i\mp 1,j\pm 1}^n(x_{i\mp\frac{1}{2}}, y_{j\pm\frac{1}{2}}) \right), \hat{q}_{i\mp 1,j\pm 1}^n(x_{i\mp\frac{1}{2}}, y_{j\pm\frac{1}{2}}) \right\}. \end{aligned}$$

A.2 2D FIFTH-ORDER WENO SCHEME RECONSTRUCTION DETAILS

The reconstruction function $R(x_{i+1/2}, y_j)$ and $R(x_i, y_{j+1/2})$ at cell interface $(x_{i+1/2}, y_j)$ and $(x_i, y_{j+1/2})$ respectively, can be written in the following way:

$$R_{i+1/2,j}^x = \sum_{k=0}^{r-1} w_k p_{i+1/2,j}^k, \quad R_{i,j+1/2}^y = \sum_{k=0}^{r-1} w_k p_{i,j+1/2}^k \quad (\text{A.3})$$

here $r = 3$,

$$p_{i+1/2,j}^{xk} = \sum_{m=0}^{r-1} c_{km} \bar{u}_{i-k+m,j}, \quad \text{and} \quad p_{i,j+1/2}^{yk} = \sum_{m=0}^{r-1} c_{km} \bar{u}_{i,j-k+m} \quad k = 0, \dots, r-1.$$

the nonlinear weights are given as:

$$w_k^x = \frac{\alpha_k^x}{\sum_{s=0}^{r-1} \alpha_s^x}, \quad \alpha_k^x = \frac{C_k}{(\epsilon + IS_k^x)^2},$$

$$w_k^y = \frac{\alpha_k^y}{\sum_{s=0}^{r-1} \alpha_s^y}, \quad \alpha_k^y = \frac{C_k}{(\epsilon + IS_k^y)^2}, k = 0, \dots, r-1$$

values of constants c_{km} , and the constants C_k are same as given above for 1D case for both x - and y - direction. The smooth indicators for x direction are given as:

$$IS_0^x = \frac{13}{12}(\bar{u}_{i,j} - 2\bar{u}_{i+1,j} + \bar{u}_{i+2,j})^2 + \frac{1}{4}(3\bar{u}_{i,j} - 4\bar{u}_{i+1,j} + \bar{u}_{i+2,j})^2,$$

$$IS_1^x = \frac{13}{12}(\bar{u}_{i-1,j} - 2\bar{u}_{i,j} + \bar{u}_{i+1,j})^2 + \frac{1}{4}(\bar{u}_{i-1,j} - \bar{u}_{i+1,j})^2,$$

$$IS_2^x = \frac{13}{12}(\bar{u}_{i-2,j} - 2\bar{u}_{i-1,j} + \bar{u}_{i,j})^2 + \frac{1}{4}(\bar{u}_{i-2,j} - 4\bar{u}_{i-1,j} + 3\bar{u}_{i,j})^2.$$

and the smooth indicators in y direction are given as:

$$IS_0^y = \frac{13}{12}(\bar{u}_{i,j} - 2\bar{u}_{i,j+1} + \bar{u}_{i,j+2})^2 + \frac{1}{4}(3\bar{u}_{i,j} - 4\bar{u}_{i,j+1} + \bar{u}_{i,j+2})^2,$$

$$IS_1^y = \frac{13}{12}(\bar{u}_{i,j-1} - 2\bar{u}_{i,j} + \bar{u}_{i,j+1})^2 + \frac{1}{4}(\bar{u}_{i,j-1} - \bar{u}_{i,j+1})^2,$$

$$IS_2^y = \frac{13}{12}(\bar{u}_{i,j-2} - 2\bar{u}_{i,j-1} + \bar{u}_{i,j})^2 + \frac{1}{4}(\bar{u}_{i,j-2} - 4\bar{u}_{i,j-1} + 3\bar{u}_{i,j})^2.$$

Here the reconstruction polynomials are given for the right (E) and top (N) edges of a cell I_{ij} are given, for obtaining the values at the left (W) and bottom edges of a cell then $k = -1, \dots, r-2$ is considered. The values of the constants are given as $C_0 = 1/10, C_1 = 3/5, C_2 = 3/10$. The other details remain the same.

A.3 2D KL SCHEME RECONSTRUCTION DETAILS

The details of the auxiliary quantities $C'S$ are given as following:

$$\begin{aligned}
C_1 &= (7084\bar{u}_{ij} - 368\sigma_1^{xy}\bar{u}_{ij} + 27\sigma_1^{xy}\bar{u}_{ij} + 10\sigma_d\bar{u}_{ij})/5760, \\
C_2 &= (36D_1^x\bar{u}_{ij} - 5D_2^x\bar{u}_{ij} - D_1^x\bar{u}_{ij+1} - D_1^x\bar{u}_{ij-1})/96, \\
C_3 &= (36D_1^y\bar{u}_{ij} - 5D_2^y\bar{u}_{ij} - D_1^y\bar{u}_{i+1j} - D_1^y\bar{u}_{i-1j})/96, \\
C_4 &= (38\sigma_1^x\bar{u}_{ij} - 3\sigma_2^x\bar{u}_{ij} + 2\sigma_1^y\bar{u}_{ij} - \sigma_D\bar{u}_{ij} - 70\bar{u}_{ij})/192, \\
C_5 &= (38\sigma_1^y\bar{u}_{ij} - 3\sigma_2^y\bar{u}_{ij} + 2\sigma_1^x\bar{u}_{ij} - \sigma_D\bar{u}_{ij} - 70\bar{u}_{ij})/192, \\
C_6 &= (D_1^x\bar{u}_{ij+1} - D_1^x\bar{u}_{ij-1})/16, \\
C_7 &= (D_1^y\bar{u}_{i+1j} - D_1^y\bar{u}_{i-1j} - 2D_1^x\bar{u}_{ij})/32, \\
C_8 &= (D_1^x\bar{u}_{ij+1} - D_1^x\bar{u}_{ij-1} - 2D_1^y\bar{u}_{ij})/32, \\
C_9 &= (D_2^x\bar{u}_{ij} - 2D_1^x\bar{u}_{ij})/96, \\
C_{10} &= (D_2^y\bar{u}_{ij} - 2D_1^y\bar{u}_{ij})/96, \\
C_{11} &= (4\bar{u}_{ij} - 2\sigma_1^{xy}\bar{u}_{ij} + \sigma_d\bar{u}_{ij})/64, \\
C_{12} &= (6\bar{u}_{ij} - 4\sigma_1^x\bar{u}_{ij} + \sigma_2^x\bar{u}_{ij})/384, \\
C_{13} &= (6\bar{u}_{ij} - 4\sigma_1^y\bar{u}_{ij} + \sigma_2^y\bar{u}_{ij})/384.
\end{aligned}$$

the discrete operators are given as:

$$\begin{aligned}
\sigma_1^x\bar{u}_{ij} &= \bar{u}_{i-1j} + \bar{u}_{i+1j}, & \sigma_2^x\bar{u}_{ij} &= \bar{u}_{i-2j} + \bar{u}_{i+2j}, \\
\sigma_1^y\bar{u}_{ij} &= \bar{u}_{ij-1} + \bar{u}_{ij+1}, & \sigma_2^y\bar{u}_{ij} &= \bar{u}_{ij-2} + \bar{u}_{ij+2}, \\
\sigma_1^{xy}\bar{u}_{ij} &= \sigma_1^x\bar{u}_{ij} + \sigma_1^y\bar{u}_{ij}, & \sigma_2^{xy}\bar{u}_{ij} &= \sigma_2^x\bar{u}_{ij} + \sigma_2^y\bar{u}_{ij}, \\
D_1^x\bar{u}_{ij} &= \bar{u}_{i+1j} - \bar{u}_{i-1j}, & D_2^x\bar{u}_{ij} &= \bar{u}_{i+2j} - \bar{u}_{i-2j}, \\
D_1^y\bar{u}_{ij} &= \bar{u}_{ij+1} - \bar{u}_{ij-1}, & D_2^y\bar{u}_{ij} &= \bar{u}_{ij+2} - \bar{u}_{ij-2}, \\
\sigma_d\bar{u}_{ij} &= \bar{u}_{i-1j-1} + \bar{u}_{i+1j+1} + \bar{u}_{i+1j-1} + \bar{u}_{i-1j+1}.
\end{aligned}$$

A.4 CONSTANTS FOR THE SSP-RK (5,4) SCHEME

Here we present the values of the constants α_{ik} and β_{ik} , which are required by SSP-RK (5,4) time integration scheme.

$$\begin{aligned}
\alpha_{10} &= 1.0 & \alpha_{20} &= 0.44437049406734 \\
\alpha_{21} &= 0.55562950593266 & \alpha_{30} &= 0.62010185138540 \\
\alpha_{32} &= 0.37989814861460 & \alpha_{40} &= 0.17807995410773 \\
\alpha_{43} &= 0.82192004589227 & \alpha_{50} &= 0.00683325884039 \\
\alpha_{52} &= 0.51723167208978 & \alpha_{53} &= 0.12759831133288 \\
\alpha_{54} &= 0.34833675773694 & \beta_{10} &= 0.39175222700392 \\
\beta_{21} &= 0.36841059262959 & \beta_{32} &= 0.25189177424738 \\
\beta_{43} &= 0.54497475021237 & \beta_{53} &= 0.08460416338212 \\
\beta_{54} &= 0.22600748319395 & \alpha_{31,41,42,51} &= 0.0 \\
\beta_{20,30,31,40,41,42,50,51,52} &= 0.0
\end{aligned}$$

A.5 CUBED-SPHERE GEOMETRY DETAILS

A cube with side of length $2a$ is inscribed into a sphere of radius R , such that all (eight) the vertices touch the sphere, where $a = R/\sqrt{3}$. The 3D absolute Cartesian co-ordinates (X, Y, Z) are normal to the cube faces, as shown in Figure. A.1. Let (x^1, x^2) , be the local Cartesian co-ordinates centered on the cube face, such that $(x^1, x^2) \in [-a, +a]$ and (λ, θ) denote the spherical longitude and latitude co-ordinates.

Here,

$$X = R \cos \lambda \cos \theta,$$

$$Y = R \sin \lambda \cos \theta,$$

$$Z = R \sin \theta.$$

The following trigonometric relations can be concluded from Figure. A.1:

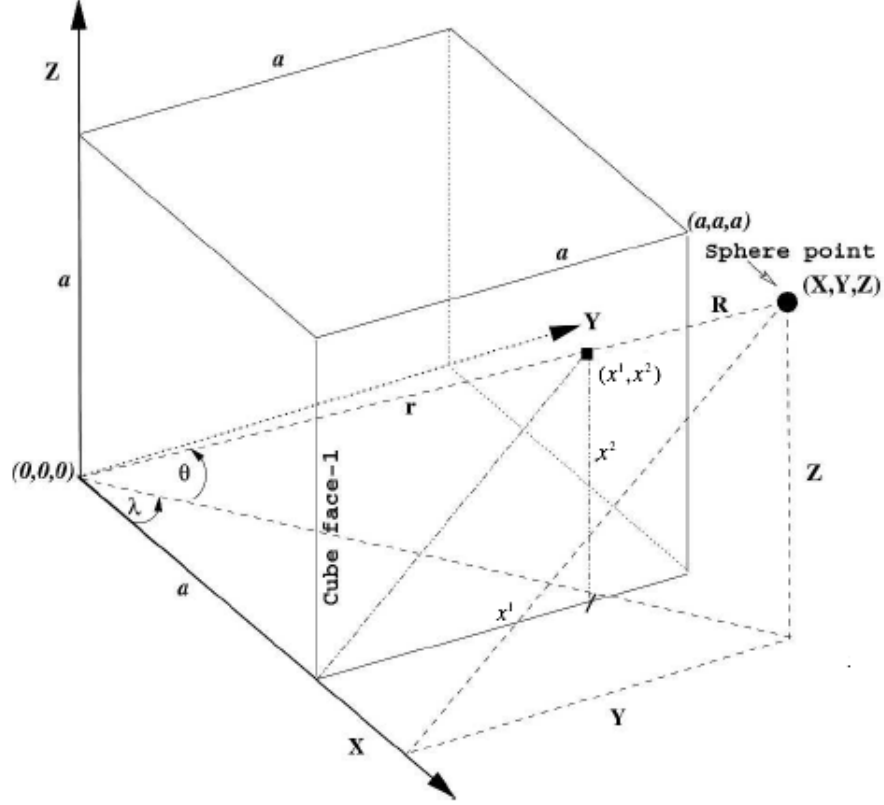


Figure A.1: Illustration of gnomonic mapping between sphere with radius R and the inscribed cube with side of length $2a$. One-eighth of the cube is shown here. A point on the cube face P_1 is marked by a solid square with local Cartesian coordinates (x^1, x^2) , and the corresponding point on the sphere is marked by a solid circle with absolute Cartesian coordinates (X, Y, Z) . The spherical polar coordinates, longitude and latitude, are λ and θ respectively. r is the radial distance from the center to any point on the cube face (Note: Figure is taken from [52]).

$$\begin{aligned}
\sin \theta &= Z/R, \\
\tan \lambda &= x^1/a = Y/X, \\
Y/Z &= x^1/x^2, \\
r^2 &= a^2 + (x^1)^2 + (x^2)^2.
\end{aligned}$$

$$x^1 = a \tan \lambda, \quad x^2 = a \tan \theta \sec \lambda. \quad (\text{A.4})$$

Equation. A.4 is the basic gnomonic transformation between the cube and its circumscribing sphere.

The covariant base vectors of the transformation between cube face and spherical surface can be obtained from the following:

$$\mathbf{a}_1 = \frac{\partial \mathbf{r}}{\partial x^1}, \mathbf{a}_2 = \frac{\partial \mathbf{r}}{\partial x^2}. \quad (\text{A.5})$$

where \mathbf{r} is the corresponding position vector on the surface of the sphere. The components of the covariant vector are given by $u_1 = \mathbf{v} \cdot \mathbf{a}_1$, $u_2 = \mathbf{v} \cdot \mathbf{a}_2$ and the corresponding contravariant components are given by:

$$\mathbf{v} = u^1 \mathbf{a}_1 + u^2 \mathbf{a}_2 \quad (\text{A.6})$$

The metric tensor for the transformation can be given as:

$$g_{ij} = \mathbf{a}_i \cdot \mathbf{a}_j = \begin{bmatrix} g_{11} & g_{12} \\ g_{21} & g_{22} \end{bmatrix} = \frac{R^2}{r^4} \begin{bmatrix} a^2 + (x^2)^2 & -x^1 x^2 \\ -x^1 x^2 & a^2 + (x^1)^2 \end{bmatrix} \quad (\text{A.7})$$

Here, $i, j \in \{1, 2\}$. The covariant and contravariant vectors are related through, $u_i = g_{ij} u^j$ and $u^i = g^{ij} u_j$, here

$$g^{ij} = g_{ij}^{-1} = \begin{bmatrix} g^{11} & g^{12} \\ g^{21} & g^{22} \end{bmatrix} = \frac{1}{g} \begin{bmatrix} g_{22} & -g^{12} \\ -g^{21} & g^{11} \end{bmatrix} \quad (\text{A.8})$$

where $g = \det(g_{ij})$, and the jacobian of the transformation is $\sqrt{g} = R^2 a / r^3$. Identical metric tensor is used on all the six cube faces. For additional details please refer to [52].

A.6 ANTI-DIFFUSIVE FLUX TERM

Here, in this section, we define the anti-diffusive flux (A_f) term given in [27] for the east wall, and by using symmetry it can be obtained for the other walls (i.e. west, north and south).

$$A_{i+1/2,j}^x = \minmod \left(\frac{u_{i+1,j}^{NW} - w_{i+1/2,j}^{int}}{a_{i+1/2,j}^+ - a_{i+1/2,j}^-}, \frac{w_{i+1/2,j}^{int} - u_{i,j}^{NE}}{a_{i+1/2,j}^+ - a_{i+1/2,j}^-}, \frac{u_{i+1,j}^{SW} - w_{i+1/2,j}^{int}}{a_{i+1/2,j}^+ - a_{i+1/2,j}^-}, \frac{w_{i+1/2,j}^{int} - u_{i,j}^{SE}}{a_{i+1/2,j}^+ - a_{i+1/2,j}^-} \right)$$

The definition of \minmod is given in Equation. 3.11, and the intermediate values are given as:

$$w_{i+1/2,j}^{int} = \frac{a_{i+1/2,j}^+ u_{i+1,j}^W - a_{i+1/2,j}^- u_{i,j}^E - \{F(u_{i+1,j}^W) - F(u_{i,j}^E)\}}{a_{i+1/2,j}^+ - a_{i+1/2,j}^-}$$

Where, a^+ and a^- are right- and left-sided local speeds which are given in Equation. 6.12, and $u_{i,j}^{NE}$, $u_{i,j}^{NW}$, $u_{i,j}^{SE}$ and $u_{i,j}^{SW}$, are the corresponding corner point values of the piecewise polynomial (Equation. 6.13) reconstruction in (i,j) th cell.

Curriculum Vitae

Kiran K Katta was born on January 16, 1985 in Madhira, India, he is the eldest child of Nageshwara Rao Katta and Padmavathi Katta and has lived in Hyderabad, India since the age of 5 until he came to El Paso for his Masters. He completed his high-school education at Narayana Jr College, Hyderabad, India in 2002 and was awarded Bachelors of Engineering (Mechanical Engineering) by Osmania University in May 2006. He was awarded Masters of Science (Mechanical Engineering) by University of Texas at El Paso (UTEP) in Dec 2008. While at UTEP, Kiran Katta has worked as a graduate research and teaching assistant. He also worked for Cummins Inc as CPE Engineer for a period of one year (Apr 2008 Apr 2009). He was given an opportunity as an Intern (SIParCS summer - 2010) at National Center for Atmospheric Center (NCAR). Presently he is pursuing his Doctoral Studies (started Aug 2009) in Program in Computational Science (CPS) at UTEP. He was also given an opportunity at NCAR as a Graduate Student Visitor for the period of 8 months during 2011 for the completion of his Doctoral thesis.

D-97 Madhuranagar, Hyderabad, AP, India, 500038.